ADVANCED STEEL CONSTRUCTION

An International Journal

Volume 13 Number 4

December 2017

CONTENTS

Technical Papers

Website: *http://www.hkisc.org*
ISSN 1816-112X
Science Citation Index Expanded, Materials Science Citation Index and ISI Alerting

Cover: The 139mx73m clear span Spectacle Roof designed by Second-order Direct Analysis without assumption of effective length

e-copy of IJASC is free to download at "www.ascjournal.com" in internet and mobile apps.

ADVANCED STEEL CONSTRUCTION

VOL.13, NO.4 (2017)

ADVANCED STEEL CONSTRUCTION

an International Journal

ISSN 1816-112X

Volume 13 Number 4 *December 2017*

ISSN 1816-112X

Science Citation Index Expanded, Materials Science Citation Index and ISI Alerting

Advanced Steel Construction
an international journal

Cover: The 139mx73m clear span Spectacle Roof designed by Second-order Direct Analysis without assumption of effective length

e-copy of IJASC is free to download at "www.ascjournal.com" in internet and mobile apps.

General Information
Advanced Steel Construction, an international journal

Aims and scope

The International Journal of Advanced Steel Construction provides a platform for the publication and rapid dissemination of original and up-to-date research and technological developments in steel construction, design and analysis. Scope of research papers published in this journal includes but is not limited to theoretical and experimental research on elements, assemblages, systems, material, design philosophy and codification, standards, fabrication, projects of innovative nature and computer techniques. The journal is specifically tailored to channel the exchange of technological know-how between researchers and practitioners. Contributions from all aspects related to the recent developments of advanced steel construction are welcome.

Instructions to authors

Submission of the manuscript. Authors may submit on-line at **www.hkisc.org**

Asian Pacific , African and organizing editor :	Professor S.L. Chan, Email: ceslchan@polyu.edu.hk
American editor :	Professor W.F. Chen, Email: waifah@hawaii.edu
European editor :	Professor R. Zandonini, Email: riccardo_zandonini@ing.unitn.it

All manuscripts submitted to the journal are recommended to accompany with a list of four potential reviewers suggested by the author(s). This list should include the complete name, address, telephone and fax numbers, email address, and at least five keywords that identify the expertise of each reviewer. This scheme will improve the process of review.

Style of manuscript

General. Author(s) should provide full postal and email addresses and fax number for correspondence. The manuscript including abstract, keywords, references, figures and tables should be in English with pages numbered and typed with double line spacing on single side of A4 or letter-sized paper. The front page of the article should contain:

a) a short title (reflecting the content of the paper);
b) all the name(s) and postal and email addresses of author(s) specifying the author to whom correspondence and proofs should be sent;
c) an abstract of 100-200 words; and
d) 5 to 8 keywords.

The paper must contain an introduction and a conclusion. The length of paper should not exceed 25 journal pages (approximately 15,000 words equivalents).

Tables and figures. Tables and figures including photographs should be typed, numbered consecutively in Arabic numerals and with short titles. They should be referred in the text as Figure 1, Table 2, etc. Originally drawn figures and photographs should be provided in a form suitable for photographic reproduction and reduction in the journal.

Mathematical expressions and units. The Systeme Internationale (SI) should be followed whenever possible. The numbers identifying the displayed mathematical expression should be referred to in the text as Eq. 1, Eq. 2.

References. References to published literature should be referred in the text, in the order of citation with Arabic numerals, by the last name(s) of the author(s) (e.g. Zandonini and Zanon [3]) or if more than three authors (e.g. Zandonini et al. [4]). References should be in English with occasional allowance of 1-2 exceptional references in local languages and reflect the current state-of-technology. Journal titles should be abbreviated in the style of the Word List of Scientific Periodicals. References should be cited in the following style [1, 2, 3].

Journal: [1] Chen, W.F. and Kishi, N., "Semi-rigid Steel Beam-to-column Connections, Data Base and Modelling", Journal of Structural Engineering, ASCE, 1989, Vol. 115, No. 1, pp. 105-119.

Book: [2] Chan, S.L. and Chui, P.P.T., "Non-linear Static and Cyclic Analysis of Semi-rigid Steel Frames", Elsevier Science, 2000.

Proceedings: [3] Zandonini, R. and Zanon, P., "Experimental Analysis of Steel Beams with Semi-rigid Joints", Proceedings of International Conference on Advances in Steel Structures, Hong Kong, 1996, Vol. 1, pp. 356-364.

Proofs. Proof will be sent to the corresponding author to correct any typesetting errors. Alternations to the original manuscript at this stage will not be accepted. Proofs should be returned within 48 hours of receipt on-line.

Copyright. Submission of an article to "Advanced Steel Construction" implies that it presents the original and unpublished work, and not under consideration for publication nor published elsewhere. On acceptance of a manuscript submitted, the copyright thereof is transferred to the publisher by the Transfer of Copyright Agreement and upon the acceptance of publication for the papers, the corresponding author must sign the form for Transfer of Copyright.

Permission. Quoting from this journal is granted provided that the customary acknowledgement is given to the source.

Page charge and Reprints. There will be no page charges if the length of paper is within the limit of 25 journal pages. A total of 30 free offprints will be supplied free of charge to the corresponding author. Purchasing orders for additional offprints can be made on order forms which will be sent to the authors. These instructions can be obtained at the Hong Kong Institute of Steel Construction, Journal website: http://www.hkisc.org

The International Journal of Advanced Steel Construction is published quarterly by learnt society, The Hong Kong Institute of Steel Construction, c/o Department of Civil & Environmental Engineering, The Hong Kong Polytechnic University, Hung Hom, Kowloon, Hong Kong.

Subscription inquiries and change of address. Address all subscription inquiries and correspondence to Member Records, IJASC. Notify an address change as soon as possible. All communications should include both old and new addresses with zip codes and be accompanied by a mailing label from a recent issue. Allow six weeks for all changes to become effective.

The Hong Kong Institute of Steel Construction
HKISC
c/o Department of Civil and Environmental Engineering,
The Hong Kong Polytechnic University,
Hunghom, Kowloon, Hong Kong, China.
Tel: 852- 2766 6047 Fax: 852- 2334 6389
Email: *ceslchan@polyu.edu.hk* Website: *http://www.hkisc.org/*
ISSN 1816-112X
Science Citation Index Expanded, Materials Science Citation Index and ISI Alerting

ISSN 1816-112X

Science Citation Index Expanded, Materials Science Citation Index and ISI Alerting

Advanced Steel Construction
an international journal

VOLUME 13 NUMBER 4 DECEMBER 2017

Technical Papers

STABILITY OF INDEPENDENT HEAVY-DUTY SCAFFOLDS: AN EXPERIMENTAL STUDY

Peng, Jui-Lin[1,*], Wang, Chung-Sheng[2], Lin, Chen-Chung[3] and Lin, Shu-Ken[4]

[1] Professor, Department of Civil and Construction Engineering, National Yunlin University of Science and Technology, Taiwan, ROC
[2] Ph.D. Student, Graduate School of Engineering Science and Technology, National Yunlin University of Science and Technology, Taiwan, ROC
3 Associate Researcher, Institute of Labor, Occupational Safety and Health, Ministry of Labor, Executive Yuan, Taiwan, ROC
[4] Lecturer, Department of Civil Engineering, National Chung Hsing University, Taiwan, ROC
**(Corresponding author: E-mail: peng.jl@msa.hinet.net)*

Received: 7 June 2016; Revised: 27 August 2016; Accepted: 26 October 2016

ABSTRACT: This study explores the stability of independent heavy-duty scaffolds by means of loading tests. The study results show that 3-story and 2-story independent heavy-duty scaffolds have very similar load capacities. The top and base screw jacks provide extra bending moment stiffness for independent heavy-duty scaffolds, which enhances the load capacity of the structural system. Horizontal braces also enhance the load capacity and the stable of independent heavy-duty scaffolds and should not be neglected. Extension of the top and base screw jacks has unobvious effect on the load capacity of independent heavy-duty scaffolds. The constructors may take advantage of this feature to adjust the height of top and base screw jacks in order to suit internal clearances and landforms of buildings. Given a similar height, as long as the number of joints is constant, the load capacities of different setups of independent heavy-duty scaffolds do not significantly vary. The eccentric load has obvious effect on the load capacity of independent heavy-duty scaffolds, which should be noted in the structure design. The age-old scaffolds treated with the red lead rust resistant paint and the used rust scaffolds have a great effect on the load capacity of the independent heavy-duty scaffolds. Therefore, they should be avoided on construction sites as much as possible. The lower limit value of the strength of reusable materials can be accurately simulated by means of the second loading in this study. Designers can choose proper strength reduction factors for reusable scaffolds based on safety requirements to conduct the structural design for independent heavy-duty scaffolds.

Keywords: Buckling, critical load, falsework, independent heavy-duty scaffold, stability

DOI: 10.18057/IJASC.2017.13.4.1

1. INTRODUCTION

Falseworks used to construct bridges are often composed of independent heavy-duty scaffolds and traditional section steel structures. Compared to falseworks of section steel structures, independent heavy-duty scaffolds have the advantage of being easier and quicker to assemble and less restricted by the working environment. For the same area, more independent heavy-duty scaffolds are needed than the falsework of section steel structures. In construction sites with a weak geological ground condition, independent heavy-duty scaffolds have a large area of contact with the ground. Additionally, comparing with the falsework of section steel structures, uneven settlement is less likely to occur on the base of independent heavy-duty scaffolds.

For buildings with high headroom and heavy concrete weights of slabs and beams, such as gymnasiums, warehouses and high-tech plants, independent heavy-duty scaffolds are often used as falseworks. Compared to frame-type steel scaffolds, members of independent heavy-duty scaffolds have a larger diameter; there is no distinction of strong and weak axes in different setups of independent heavy-duty scaffolds; and independent heavy-duty scaffolds have a bigger load capacity. Therefore, unlike independent heavy-duty scaffolds, frame-type steel scaffolds are commonly used in reinforced concrete buildings with medium and low headroom and smaller concrete weights of labs and beams.

Independent heavy-duty scaffolds are assembled independently as an isolated setup whereas frame-type steel scaffolds are assembled in a row-type setup. Because of their high load capacity, quick assembly and disassembly, and suitability of different working environments, independent heavy-duty scaffolds are often used in structures with heavy concrete weights of slabs and beams, such as bridges and high-tech plants. Figure 1 shows independent heavy-duty scaffolds assembled on construction sites of a high-tech plant at the Central Taiwan Science Park.

Figure 1. Independent Heavy-duty Scaffolds Assembled on Construction Sites of a High-tech Plant at the Central Taiwan Science Park

Independent heavy-duty scaffolds are widely used on construction sites in Taiwan. However, due to lack of information available for reference in design and safety assembly, independent heavy-duty scaffolds assembled on construction sites have a very high risk of collapse. Figure 2 shows the collapse scene of independent heavy-duty scaffolds on construction sites of a bridge engineering in Zhunan Section of National Freeway No. 3. The accident caused one death and two injuries on the spot.

Figure 2. Collapse Scene of Independent Heavy-duty Scaffolds on Construction Sites of a Bridge in Zhunan Section of National Freeway No. 3

Until now, most studies of falsework have focused on frame-type and door-type steel scaffolds. Apart from studying the system reliability of frame-type steel scaffolds, Zhang et al. [1] also explored the variabilities of various parameters of the load capacity of frame-type steel scaffolds.

Weesner and Jones [2] performed a numerical analysis of the strength of frame-type steel scaffolds based on eigenvalue buckling analysis and geometrically nonlinear analysis, and loading tests were conducted. Yu and Chung [3] studied the relationship between number of stories and load capacities of door-type steel scaffolds and proposed a simplified model for use in designing scaffolds. Yu et al. [4] explored the effect of different boundary conditions and X-bracing on the strength of door-type steel scaffolds.

Peng et al. [5] compared structural behaviors between "door-type steel scaffolds" and "door-type steel scaffold system with wooden shores" from the perspective of structural stability and proposed a simplified theoretical analysis model. Peng et al. [6] studied the effect of different number of stories, rows and spans on the load capacity of "door-type steel scaffolds" and "door-type steel scaffold system with wooden shores" and proposed the design guidelines for door-type steel scaffolds. Peng et al. [7] used loading tests to explore the relationship between number of spans and load capacity of single-row multi-span door-type steel scaffolds.

In terms of studies on other non-frame-type or non-door-type steel scaffolds, Peng et al. [8] studied the two-story shoring system assembled with wooden shores and adjustable steel tube shores and determined the load model and the load capacity of the two-story shoring system. Peng et al. [9] performed tests and analyses of system scaffolds to determine the load capacities and failure models in different scaffold setups. Liu et al. [10] conducted loading tests on the tube and coupler steel scaffold system without X-bracing to explore the load capacity and the failure model for the whole system. Peng et al. [11] confirmed that the critical load of the whole system decreased based on loading tests when other supporting shores were added to the top of independent heavy-duty scaffolds. Therefore, this combined setup should be avoided on construction sites.

As mentioned above, most previous studies focused on frame-type steel scaffolds, door-type steel scaffolds, tube and coupler steel scaffolds, and system scaffolds, but few on independent heavy-duty scaffolds. Unlike the above-mentioned steel scaffolds that are assembled in a row-type setup, independent heavy-duty scaffolds are assembled independently. Therefore, findings of studies on those steel scaffolds are not directly applicable to independent heavy-duty scaffolds. For this reason, the load capacity and the failure model for independent heavy-duty scaffolds need further study.

2. OBJECTIVES AND HIGHLIGHTS

This study analyzed the stability of independent heavy-duty scaffolds in various configurations. Loading tests are used to explore the critical load and the failure model for various independent heavy-duty scaffold setups. The results of this study are expected to serve as a reference for future structural analysis and design of independent heavy-duty scaffolds in order to reduce the risk of collapse.

This study generalizes the following key factors that affect the load capacity and the failure model for independent heavy-duty scaffolds on construction sites: (1) different number of stories, (2) without top and base screw jacks, (3) with extended top and base screw jacks, (4) without horizontal braces, (5) eccentric load, (6) with unrestrained boundary, (7) same height with different setups, (8) similar height with more joints, (9) reusable and rusted scaffolds, and (10) simulation of lower strength bounds of reusable scaffolds. Loading tests are used to explore these key factors.

3. SECTIONAL DIMENSIONS AND MATERIAL PROPERTIES

Independent heavy-duty scaffolds mainly consist of triangle-type scaffold units, ledgers and horizontal braces. The triangle-type scaffold unit consists of a vertical member, a horizontal member, an internal sub-horizontal member and a diagonal brace. Figure 3 shows how various members are arranged. The figure shows that each story is composed of four triangle-type scaffold units and ledgers. Horizontal braces are placed in the junction between stories to enhance structural stability. Measurement of six setups of independent heavy-duty scaffolds obtained the average cross dimensions of various members as follows:

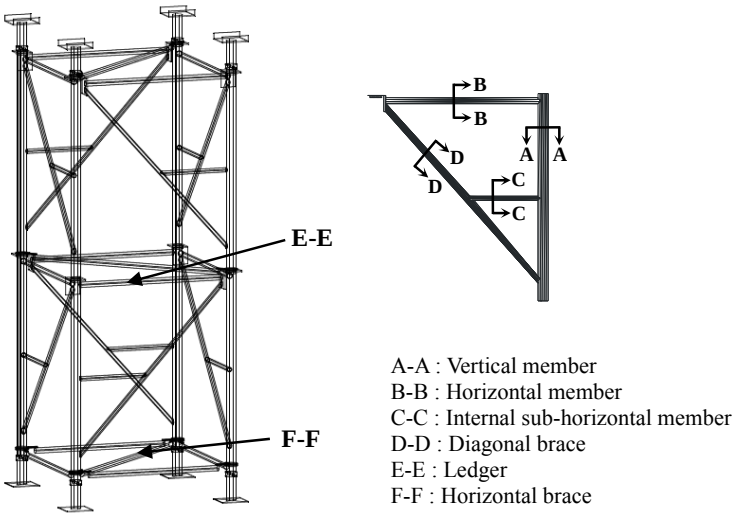

Figure 3. Arrangement of Various Members of an Independent Heavy-duty Scaffold

In the triangle-type scaffold units: vertical member (section A-A): external diameter (D)=76.35 mm, thickness (t)=3.32 mm ; horizontal member (section B-B): external diameter (D)=42.26 mm, thickness (t)=2.24 mm; internal sub-horizontal member (section C-C): external diameter (D)=33.62 mm, thickness (t)=2.24 mm; diagonal brace (section D-D): external diameter (D)=33.63 mm, thickness (t)=2.18 mm. Ledger (section E-E): external diameter (D)=42.35 mm, thickness (t)=2.40 mm. Horizontal brace (section F-F): external diameter (D)=42.27 mm, thickness (t)=1.92 mm.

In this study, coupon tests are performed on six sets of members randomly selected from independent heavy-duty scaffolds. The average elastic modulus (E) of the six sets of members is 20386 kN/cm^2, which approximates the nominal value 20012.4 kN/cm^2. Therefore, further numerical analyses can use nominal value for reference.

4. TEST PLAN

4.1 Different Number of Stories

Different stories of independent heavy-duty scaffolds used on construction sites are needed to cope with the variation of headroom of the structure during construction. Independent heavy-duty scaffolds with different stories have different load capacities. This study performed loading tests on two-story and three-story independent heavy-duty scaffolds to explore how the load capacities of independent heavy-duty scaffolds was affected by a change in height. The test values can be used as comparing data for other tests in this study. For convenience sake, in this study, these two setups of independent heavy-duty scaffolds are defined as "basic setups". Figure 4 shows the test arrangements.

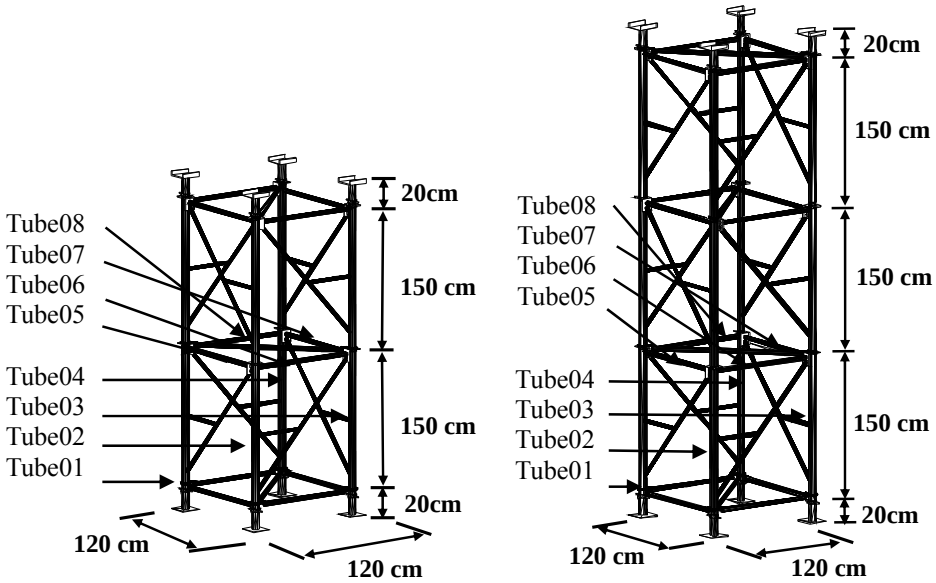

Figure 4. Configurations of Two-story and Three-story Independent Heavy-duty Scaffolds

This section also measures the axial forces of different members by using strain gauges attached on Tube 01 ~ Tube 04 for vertical members and on Tube 05 ~ Tube 08 for ledgers. Figure 4 shows the positions of these strain gauges in two-story and three-story independent heavy-duty scaffolds.

4.2 Without Top and Base Screw Jacks

The top and base screw jacks of independent heavy-duty scaffolds are mainly used to adjust the scaffold elevation. The end plates of the top and base screw jacks provide bending moment stiffness for the independent heavy-duty scaffold structural system. This study explores the effect of top and base screw jacks on the load capacity of independent heavy-duty scaffolds. The test setups are the same as those described in previous section except that the end plates of the top and base screw jacks are removed. In the numerical analysis, the boundary conditions are considered as hinged ends because no bending moment stiffness is provided due to lack of the end plates here. Figure 5 shows the test configuration of two-story independent heavy-duty scaffolds. Unless otherwise specified, the top and base screw jacks used in the tests have lengths of 20 cm.

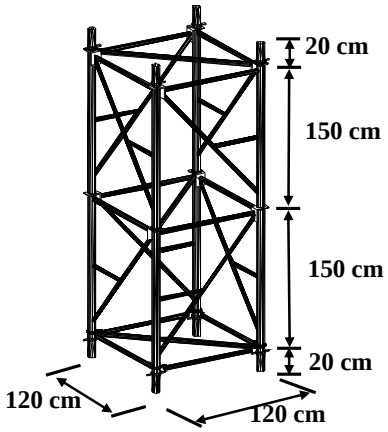

Figure 5. Configuration of Two-story Independent heavy-duty scaffolds without end plates of the top and base screw jacks

4.3 With Extended Top and Base Screw Jacks

On construction sites, the top and base screw jacks of independent heavy-duty scaffolds often musts be extended to cope with the variation of landforms and headrooms of structures under construction. For the tests in this study, the length of the top and base screw jacks was increased from 20 cm to 40 cm to determine the relationship between the extended length of top and base screw jacks and load capacity. Figure 6 shows the test configuration of three-story independent heavy-duty scaffolds with extended top and base screw jacks.

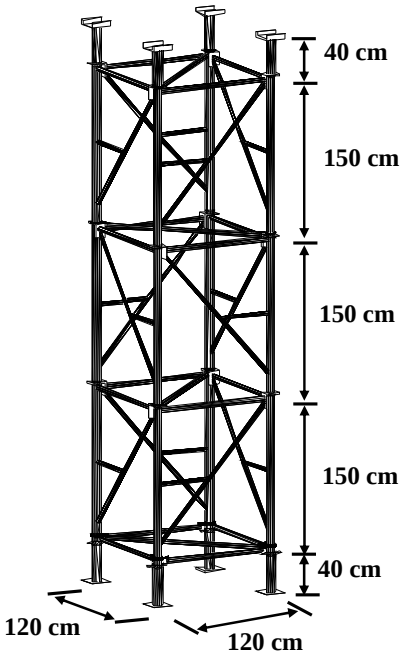

Figure 6. Configuration of Three-story Independent Heavy-duty Scaffolds with Extended Top and Base Screw Jacks

4.4 Without Horizontal Braces

In the tests, the horizontal braces of independent heavy-duty scaffolds are removed to determine how the horizontal braces affect the load capacity of independent heavy-duty scaffolds. Figure 7 shows test configuration of two-story independent heavy-duty scaffolds without horizontal braces.

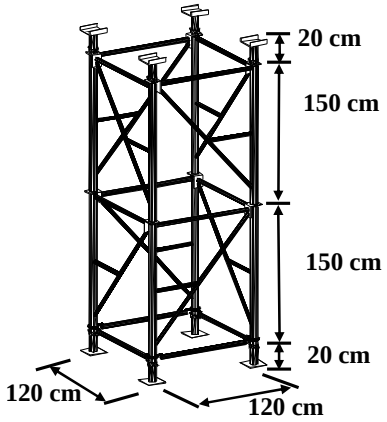

Figure 7. Configuration of Two-story Independent Heavy-duty Scaffolds without Horizontal Braces

4.5 Eccentric Load

On construction sites, fresh concrete is often applied following a preset grouting path. Therefore, in the process of fresh concrete grouting, the concrete load applied to independent heavy-duty scaffolds is likely to become eccentric. In the basic test setup, the load is applied eccentrically in two directions (double eccentric loading L/3). Figure 8 shows where the double eccentric loading L/3 was applied. This study explores the effect of double eccentric loading L/3 on the load capacity of independent heavy-duty scaffolds.

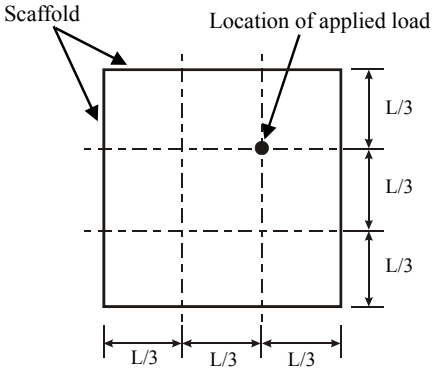

Figure 8. Top View of Location of Applied Load of Double Eccentric Loading L/3

4.6 With Unrestrained Boundary

On the construction site of bridge engineering, independent heavy-duty scaffolds are often assembled between two piers. No extra restraint for the bridge deck is provided in the direction perpendicular to the piers (lateral direction of the bridge). In the process of fresh concrete grouting, the bridge deck may drift laterally in the non-restraint direction, causing lateral displacement at the top of independent heavy-duty scaffolds and bridge formwork.

Simulating lateral displacement on the top boundary of independent heavy-duty scaffolds in a universal test machine is difficult because the hydraulic jack of the universal test machine is a fixed device that does not allow lateral displacement. Therefore, the whole heavy-duty scaffold system is turned upside down to proceed the tests, turning the bottom of the system into a free end that allows lateral displacement. The free end is simulated with steel balls.

Figure 9 shows the diagram of two-story independent heavy-duty scaffolds with the possible boundary lateral displacement. Two overlapping steel plates are placed at the bottom under each vertical member in the area that touches the ground. Figure 9 shows how nine rectangular sections are divided between the two steel plates. Four steel balls are placed in each section to simulate the situation that allows boundary lateral displacement.

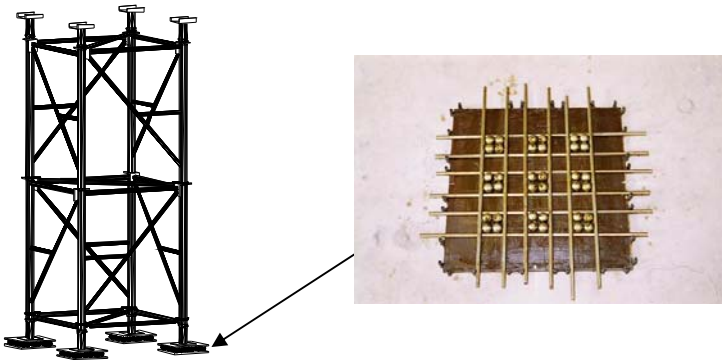

Figure 9. Configuration of Two-story Independent Heavy-duty Scaffolds with Possible Boundary Lateral Displacement

4.7 Same Height with Different Setups

The triangle-type scaffold unit of independent heavy-duty scaffolds is available in different sizes. With the same height, different sizes of triangle-type scaffold unit can be used to assemble independent heavy-duty scaffolds in various combinations. The objective of this study was to determine which setup has the best load capacity.

Three heights of triangle-type scaffold units are used in the tests: 0.5 m, 1 m and 1.5 m. In coordination with the internal clearance of the universal test machine, the independent heavy-duty scaffolds with a total height of 3.5 m are used to proceed with loading tests. Tests are divided into three cases according to the heights of top, medium and bottom stories (1.5 m, 1 m and 1 m in case A; 1.5 m, 0.5 m and 1.5 m in case B; 1.5 m, 1.5 m and 0.5 m in case C, respectively). Figure 10 shows the test configurations of various setups.

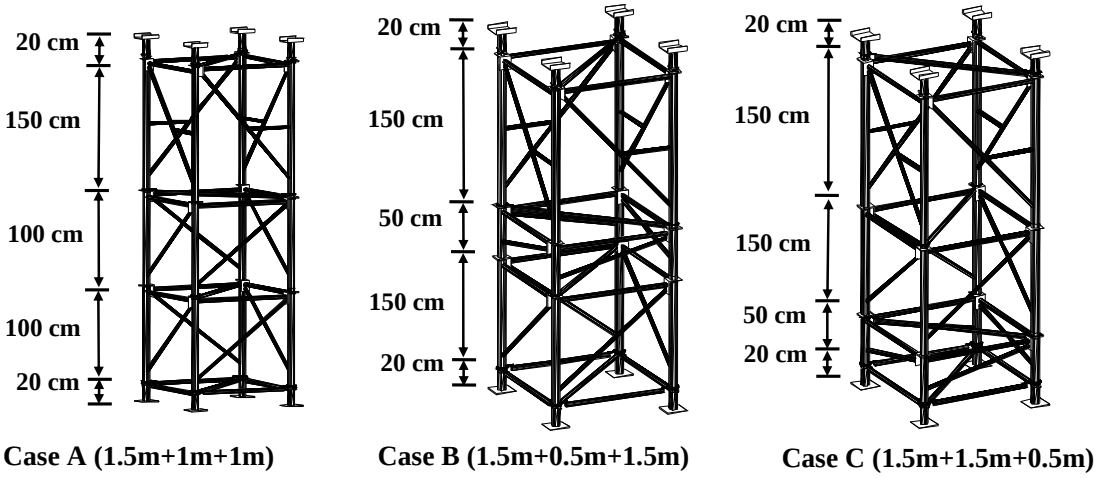

Figure 10. Configurations of Independent Heavy-duty Scaffolds with Different Sizes of Triangle-type Scaffold Units in the Same Height

4.8 Similar Height with More Joints

On construction sites, 150 cm triangle-type scaffold units are usually used to assemble independent heavy-duty scaffolds. If shorter triangle-type scaffold units, such as 110 cm ones, are used, there will be more joints with the same height. This study explores the variation of load capacities when there are more joints (or shorter triangle-type scaffold units are used) in the configuration of independent heavy-duty scaffolds with similar height.

In the tests, three 110 cm triangle-type scaffold units are used to assemble independent heavy-duty scaffolds (a three-story system with a total height of 330 cm). The test results for the three-story scaffolds were compared with those for the two-story basic setup of scaffolds assembled with two 150 cm triangle-type scaffold units with a total height of 300 cm. Figure 11 shows the configuration of three-story independent heavy-duty scaffolds assembled with three 110 cm triangle-type scaffold units with more joints compared to the two-story basic setup of scaffolds.

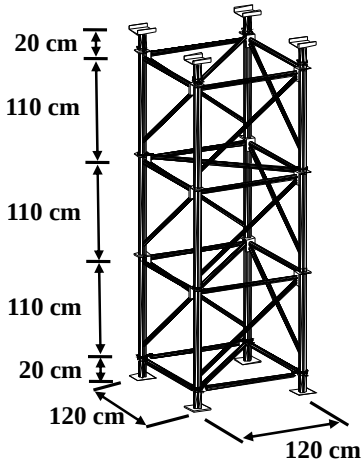

Figure 11. Configuration of Three-story Independent Heavy-duty Scaffolds Assembled with Three 110 cm Triangle-type Scaffold units with More Joints

4.9 Reusable and Rusted Scaffolds

(I) Red lead antirust paint

Independent heavy-duty scaffolds manufactured at different times have used different antirust paint. In Taiwan, red lead antirust paint was used in early days and galvanization in more recent times for antirust treatment. This study used loading tests to explore the load capacity and failure model for independent heavy-duty scaffolds assembled with age-old and appearance defective materials treated with red lead antirust paint. The test results were then compared with those obtained from tests on the basic setup of independent heavy-duty scaffolds treated with antirust galvanizing paint.

(II) Rusted used scaffolds

Independent heavy-duty scaffolds are often reused to reduce costs. After repeated use, due to friction and collision, the antirust paint may fall off and steel tubes may be slightly sunken, which might lead to serious rustiness on independent heavy-duty scaffolds. Rust can cause the changes of material quality and tube thickness, which will reduce the load capacity of independent heavy-duty scaffolds. This study performed loading tests to explore the load capacity and failure model for independent heavy-duty scaffolds assembled with seriously rusted scaffold surfaces treated with galvanization. This test can detect the difference of load capacity between independent heavy-duty scaffolds assembled with and without severely rusted scaffold surfaces.

4.10 Simulation of Lower Strength Bounds of Reusable Scaffolds

This study explores the lower bounds of the load capacity of reusable independent heavy-duty scaffolds. After the first loading on independent heavy-duty scaffolds, the independent heavy-duty scaffold systems were unloaded and readjusted before the second loading. The second test values obtained will be considered the simulated lower bounds of the load capacity of reusable scaffolds. The rationale for the tests is that after the first loading, permanent deformation of the independent heavy-duty scaffolds could be used to simulate the worst condition of reusable independent heavy-duty scaffolds on construction sites.

In the tests, the strength reduction factor of reusable independent heavy-duty scaffolds (ϕ) was obtained by dividing the load capacity of the second loading by that of the first loading. The average of strength reduction factors (μ) and the standard deviation (σ) can be used as a reference for the structural design of independent heavy-duty scaffolds.

5. TEST RESULTS AND DISCUSSIONS

5.1. Different Number of Stories

Table 1 shows the test results of two-story independent heavy-duty scaffolds with an average load capacity of 981.72 kN. Figure 12 is the diagram of load - vertical displacement curve (P-Δ curve) of the loading test on two-story independent heavy-duty scaffolds, which is a basic setup of independent heavy-duty scaffolds. The test results for other two-story independent heavy-duty scaffolds can be compared with those for this setup.

Table 1. Results of Loading Tests for Various Setups of Independent Heavy-duty Scaffolds

Setups	Type	Test code	Test values (kN)					Comparison with basic setups	
			Case A	Case B	Case C	Case D	Average	2-story	3-story
Basic setup	2-story	BUS2	1012.99 (736.31)	941.30 (708.369)	990.88	#	981.72	1	-
	3-story	BUS3	951.57 (756.51)	891.04 (644.15)	#	#	921.31	-	1
Without top and base screw jacks (simulated hinged ends)	2-story	NBNUS2	919.99	842.88	#	#	831.44	0.85	-
	3-story	NBNUS3B	744.32	784.19	#	#	764.25	-	0.83
Extended top and base screw jacks	2-story	HDS2 (HDDS2)	938.46 (722.04)	970.43 (744.95)	#	#	954.45 (733.50)	0.97	-
	3-story	HDS3 (HDDS3)	954.36 (483.39)	824.77 (664.41)	730.68 (555.19)	859.11 (534.23)	842.23 (559.30)	-	0.91
Without horizontal braces	2-story	NHBS2 (NHDBS2)	898.75 (695.92)	880.09 (583.42)	868.00	#	882.28	0.90	-
	3-story	NHBS3	763.00	761.26	#	#	762.13	-	0.83
Eccentric load	2-story	ELS2	674.90 (568.75)	722.76 (604.54)	#	#	698.83 (585.14)	0.71	-
	3-story	ELS3	657.45 (575.13)	684.47 (577.00)	#	#	670.96 (576.56)	-	0.73
With lateral displacement on the boundary	2-story	UBS2B	777.24	1003.18	895.65	#	892.02	0.91	-
	3-story	UBS3	871.45	778.81	818.40	#	822.89	-	0.89
Same height with different setups	1.5m 1m 1m	VCS11	792.37 (623.89)	981.69 (754.38)	857.12 (760.78)	#	877.06 (713.02)	-	-
	1.5m 0.5m 1.5m	VCS05S	842.32 (468.08)	873.34 (634.19)	#	#	857.83 (551.13)	-	-
	1.5m 1.5m 0.5m	VCSS05	874.54 (380.58)	925.19 (668.78)	#	#	889.87 (524.68)	-	-
Similar height with more joints	3-story 1.1m	SH310	1120.25 (926.71)	1077.19 (749.09)	#	#	1098.72 (837.90)	1.12	-
Treated with red lead antirust paint	2-story	OCS2 (OCDS2)	690.92 (545.26)	737.32 (519.15)	#	#	714.12 (583.88)	0.73	-
	3-story	OCS3 (OCDS3)	662.89 (507.91)	636.35 (519.15)	#	#	649.62 (513.53)	-	0.71
Rusted used materials	2-story	RBUS2	712.00 (519.15)	723.92 (531.48)	#	#	717.96 (525.32)	0.73	-

Notes:
1. Figure in parentheses "( )" refers to the load capacity of the second loading on the independent heavy-duty scaffolds that have been readjusted after the first loading.
2. Unless otherwise specified, each test setup is assembled with 20 cm top and base screw jacks, horizontal braces, and mutually perpendicular lateral bracing stories.
3. # refers to no test value
4. – refers to no ratio

Table 1 also shows the test results of three-story independent heavy-duty scaffolds with an average load capacity of 921.31 kN. Figure 13 shows the failure model for this system under loading. By comparison, the load capacity of three-story basic setup is around 94% (= 921.31/981.72) of that of its two-story counterpart, indicating that the load capacities of these two basic setups are very close. Figures 14, 15 and 4 show the axial forces of vertical members and ledgers measured from strain gauges for two-story and three-story independent heavy-duty scaffolds. The figures show that the vertical members take most of the applied loads, and the axial forces of horizontal ledgers are insignificant. This indicates that the strong or weak vertical member influences the load capacity of independent heavy-duty scaffolds.

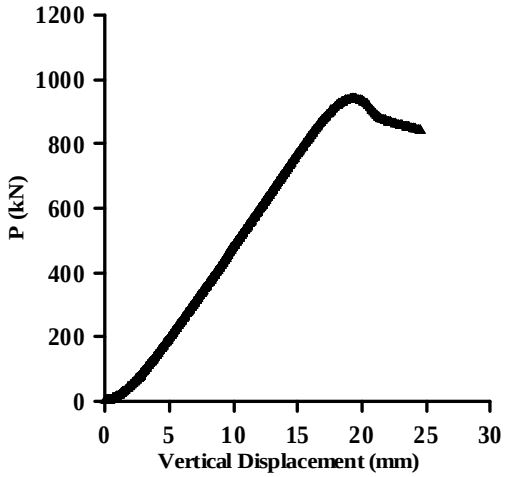

Figure 12. Load - Vertical Displacement Curve of Loading Tests on Two-story Independent heavy-duty scaffolds

Figure 13. Failure Model for Three-story Basic Setup of Independent Heavy-duty Scaffolds under loading

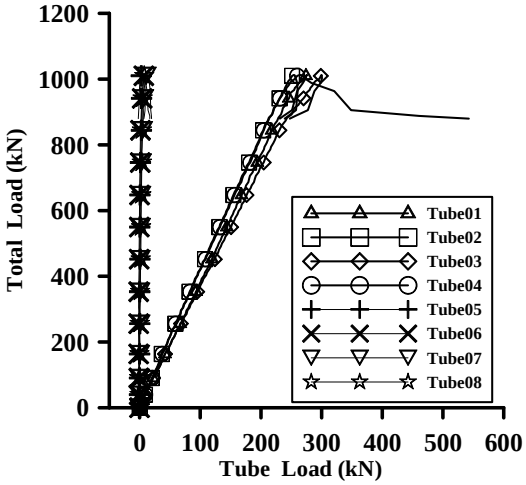

Figure 14. Total Loads-axial Forces of Vertical Members and Ledgers of Two-story Independent Heavy-duty Scaffolds

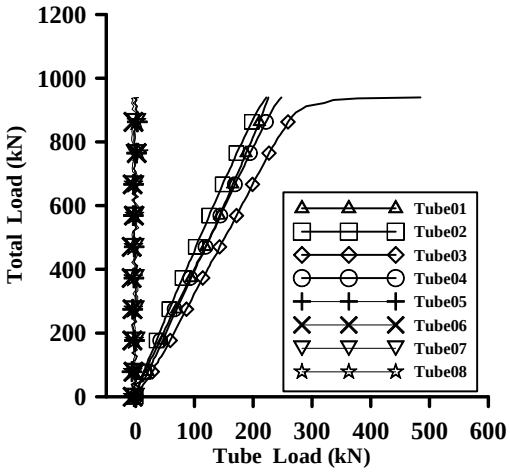

Figure 15. Total Loads-axial Forces of Vertical Members and Ledgers of Three-story Independent Heavy-duty Scaffolds

5.2 Without Top and Base Screw Jacks

Table 1 shows the test results of two-story and three-story independent heavy-duty scaffolds with end plates of top and base screw jacks removed to simulate hinged ends. The average load capacity of the two-story independent heavy-duty scaffolds without end plates of top and base screw jacks is 831.44 kN, which is 85% (= 831.44/981.72) of that of the two-story basic setup. The average load capacity of three-story scaffolds without end plates is 764.25 kN, which is 83% of that in the three-story basic setup (921.31 kN). Figure 16 shows the failure model for three-story independent heavy-duty scaffolds without end plates of top and base screw jacks under loading. The test results for the two-story and three-story independent heavy-duty scaffolds show that, because the top and base screw jacks provide bending moment stiffness, they enhance the load capacity of independent heavy-duty scaffolds.

The quotient of the load capacity of three-story independent heavy-duty scaffolds without end plates of top and base screw jacks and that of two-story independent heavy-duty scaffolds with same conditions is 92% (=764.26/831.44). Therefore, the load capacity of independent heavy-duty scaffolds without end plates of top and base screw jacks, simulating hinged ends, is not significantly associated with the increase in the number of stories.

Figure 16. Failure Model for Three-story Independent Heavy-duty Scaffolds without End Plates of Top and Base Screw Jacks under Loading

5.3 With Extended Top and Base Screw Jacks

Table 1 shows that, when the length of top and base screw jacks is increased from 20 cm to 40 cm, the average load capacity of two-story independent heavy-duty scaffolds is 954.45 kN and that of three-story independent heavy-duty scaffolds is 842.23 kN, which are 97% (= 954.45/981.72) and 91% (= 842.23/921.31) of the load capacities of the two-story and three-story basic setups respectively. Figure 17 shows the failure model for three-story independent heavy-duty scaffolds with extended top and base screw jacks under loading.

The test results show that, when the top and base screw jacks of independent heavy-duty scaffolds are extended to 40 cm, reduction of load capacity of the overall independent heavy-duty scaffold structural system is small. Based on these test results, constructors may choose to extend the length of top and base screw jacks to cope with the variation of the internal clearance of building, instead of adopting a combined setup of independent heavy-duty scaffolds, using other kinds of shores at the top of scaffolds. A combined setup reduces the load capacity of the overall scaffold system (Peng et al. 2014).

Figure 17. Failure Model for Three-story Independent Heavy-duty Scaffolds with Extended Top and Base Screw Jacks under Loading

5.4 Without Horizontal Braces

Table 1 shows that the average load capacity of two-story independent heavy-duty scaffolds without horizontal braces is 882.28 kN and that of their three-story counterparts is 762.13 kN, which are 90 % (= 882.28/981.72) and 83 % (= 762.13/921.31) of the load capacities of the two-story and three-story basic setups respectively. Figure 18 shows the failure model for three-story independent heavy-duty scaffolds without horizontal braces under loading.

The test results show that the horizontal braces increase the strength of independent heavy-duty scaffolds. When independent heavy-duty scaffold systems are not reinforced with horizontal braces, with the increase of number of stories, the reduction of the load capacity of independent heavy-duty scaffold systems becomes more obvious.

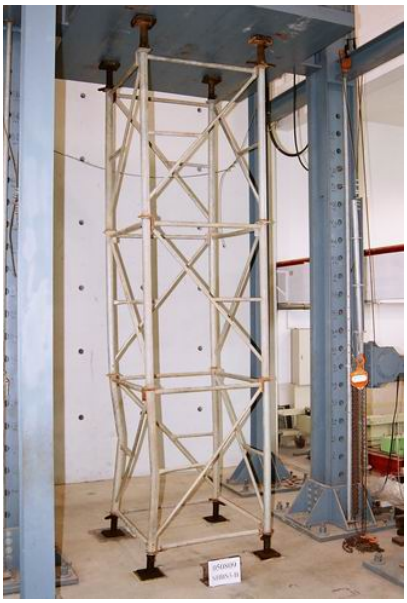

Figure 18. Failure Model for Three-story Independent Heavy-duty Scaffolds without Horizontal Braces under Loading

5.5 Eccentric Load

Table 1 shows that, for the test results and Figure 8 for the setup of eccentric loading, the average load capacity of two-story independent heavy-duty scaffolds with double eccentric loading L/3 is 698.83 kN, and that of their three-story counterparts is 670.96 kN, which are 71% (= 698.83/981.72) and 73% (= 670.96/921.31) of the load capacities of the two-story and three-story basic setups respectively. Figure 19 shows the failure model for three-story independent heavy-duty scaffolds with double eccentric loading L/3 under loading.

The test results show that, with double eccentric loading L/3, the load capacity of independent heavy-duty scaffolds decreases by almost 30%. Therefore, when independent heavy-duty scaffolds are used under eccentric loads, safety factors in the structural design should be increased.

Figure 19. Failure Model for Three-story Independent Heavy-duty Scaffolds with Eccentric Load under Loading

5.6 With Unrestrained Boundary

Based on the unrestrained boundary in Figure 9, Table 1 shows that the average load capacity of two-story independent heavy-duty scaffolds with lateral displacement on the boundary is 892.02 kN, and that of their three-story counterparts is 822.89 kN, which are 91 %(= 892.02/981.72) and 89%(= 822.29/921.31) of the load capacities of the two-story and three-story basic setups, respectively. Figure 20 shows the failure model for three-story independent heavy-duty scaffolds with lateral displacement on the boundary under loading.

Theoretically, a lateral displacement on the boundary significantly reduces the load capacity of independent heavy-duty scaffolds. However, the load capacity was not obviously reduced in these tests. In fact, steel balls used to simulate the roller support exist the friction force between steel plates and steel balls. The friction force ($F=\nu N$) is proportional to the normal force (N), where ν is the coefficient of friction. As the applied load from the universal test machine increases, the friction force rises with the increase of the normal force. As the friction force was increased in the tests, the lateral displacement on the boundary became unobvious so that the reduction of load capacity of the independent heavy-duty scaffolds was not as high as expected.

Figure 20. Failure Model for Three-story Independent Heavy-duty Scaffolds with Lateral Displacement on the Boundary under Loading

5.7 Same Height with Different Setups

Figure 10 shows that the three setups of independent heavy-duty scaffolds were considered in the tests – Cases A, B and C. Table 1 shows the test results, which revealed that the average load capacity of case A (the heights of top, medium and bottom stories are 1.5 m, 1 m and 1 m respectively) is 877.06 kN; the average load capacity of case B (the heights of top, medium and bottom stories are 1.5 m, 0.5 m and 1.5 m respectively) is 857.83 kN; the average load capacity of case C (the heights of top, medium and bottom stories are 1.5 m, 1.5 m and 0.5 m respectively) is 889.87 kN. Figure 21 shows the failure models for three cases of independent heavy-duty scaffolds. The test results show that, for a height of 3.5 m, although case C has the highest load capacity, the load capacities of cases A and B do not lag far behind case C, indicating that when the height is the same, the load capacities of independent heavy-duty scaffolds assembled with different sizes of triangle-type scaffold units are similar.

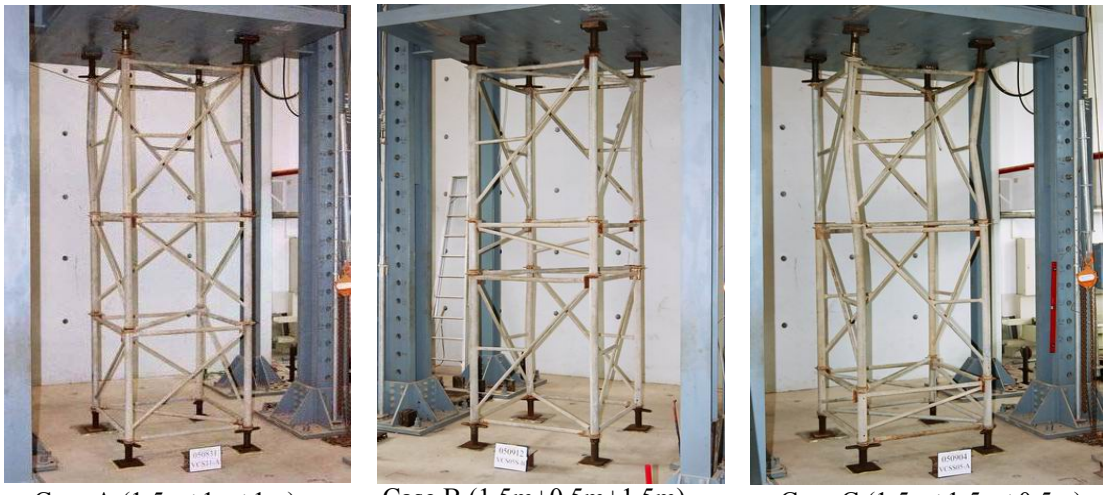

Case A (1.5m+1m+1m) Case B (1.5m+0.5m+1.5m) Case C (1.5m+1.5m+0.5m)

Figure 21. Failure Models for Independent Heavy-duty Scaffolds with the Same Height but Different Configurations

5.8 Similar height with more joints

As shown in Table 1, the average load capacity of three-story independent heavy-duty scaffolds assembled with three 110 cm triangle-type scaffold units (total height=330 cm) is 1098.72 kN. Figure 22 shows the failure model for this structural system. The average load capacity of two-story independent heavy-duty scaffolds assembled with two 150 cm triangle-type scaffold units (total height=300 cm) is 981.72 kN. The quotient of the former (1098.72 kN) divided by the latter (981.72 kN) is 112.0%. The test results show that, for a total height circa 300 cm, independent heavy-duty scaffolds assembled with shorter triangle-type scaffold units have a higher total height and more joints but a higher load capacity.

Figure 22. Failure Model for Three-story Independent Heavy-duty Scaffolds Assembled with Three 110 cm Triangle-type Scaffold Units under Loading (total height=330 cm)

5.9 Reusable and Rusted Scaffolds

(I) Red lead antirust paint

As shown in Table 1, the average load capacities of two-story and three-story reusable independent heavy-duty scaffolds treated with red lead antirust paint are 714.12 kN and 649.62kN respectively, which are 73%(= 714.12/981.72) and 71%(= 649.62/921.31) of the load capacities of two-story and three story basic setups respectively. Figure 23 shows the failure model for three-story reusable independent heavy-duty scaffolds treated with red lead antirust paint under loading.

Figure 23. Failure Model for Three-story Reusable Independent Heavy-duty Scaffolds Treated with Red Lead Antirust Paint under Loading

(II) Rusted used Scaffolds

In this case, the tests were mainly performed on two-story independent heavy-duty scaffolds. The load capacity of two-story reusable and rusted independent heavy-duty scaffolds is 717.96 kN, which is 73% (= 719.96/981.72) of two-story basic setup. Therefore, using reusable and rusted independent heavy-duty scaffolds has a large effect on load capacity.

As shown by the test results, the load capacity of independent heavy-duty scaffolds assembled with aged materials treated with red lead antirust paint or rusted used materials reduces around 30%. Therefore, on construction sites, when assembling independent heavy-duty scaffolds, constructors should avoid using age-old or rusted used materials in order to enhance the construction safety.

5.10 Simulation of Lower Strength Bounds of Reusable Scaffolds

According to the tests, the deformation of independent heavy-duty scaffolds after the first loading is the worst condition of the reusable scaffolds on construction sites. The load capacity of the second loading is defined as the “simulation of lower strength bounds of reusable scaffolds”. The strength reduction factor of load capacity of the reusable independent heavy-duty scaffolds (ϕ) is obtained by dividing the load capacity of the second loading by that of the first loading.

Table 2. Simulated Lower Strength Bounds of Load Capacities of the Reusable Independent heavy-duty scaffolds

Setup	Type	Test case	Average test values (kN)		□□= 2nd loading/1st loading	Average	Standard deviation
			1st loading Load capacity	2nd loading Load capacity			
Basic setup	2-story	A	1012.99	736.31	0.727	0.739	0.111
		B	941.3	708.369	0.753		
	3-story	A	951.57	756.51	0.795		
		B	891.04	644.15	0.723		
Without horizontal brace	2-story	A	898.75	695.92	0.774		
		B	880.09	583.42	0.663		
Extended top/base screw jacks	2-story	A	938.46	722.04	0.769		
		B	970.43	744.95	0.768		
	3-story	A	954.36	483.39	0.507		
		B	824.77	664.41	0.806		
		C	730.68	555.19	0.760		
		D	859.11	534.23	0.622		
Eccentric load	2-story	A	674.90	568.75	0.843		
		B	722.76	604.54	0.836		
	3-story	A	657.45	575.13	0.875		
		B	684.47	577.00	0.843		
Same height with different setups	1.5m+1m +1m	A	792.37	623.89	0.787		
		B	981.69	754.38	0.768		
		C	857.12	760.78	0.888		
	1.5m+0.5 m +1.5m	A	842.32	468.08	0.556		
		B	873.34	634.19	0.726		
	1.5m+1.5 m +0.5m	A	874.54	380.58	0.435		
		B	925.19	668.78	0.723		
Same height with different number of stories	3-story 1.1m	A	1120.25	926.71	0.827		
		B	1077.19	749.09	0.695		

Notes:
Average value: $\bar{x} = \sum_{i=1}^{n} x_i / n$; Standard deviation: $\sigma = \sqrt{\frac{\sum (x - \bar{x})^2}{(n-1)}}$

Table 2 shows that the average of all strength reduction factors (μ) is 0.739, and the standard deviation (σ) is 0.111. Figure 24 is the scatter plot from the average value plus or minus one standard deviation ($\mu \pm \sigma$) to plus or minus three standard deviations ($\mu \pm 3\sigma$).

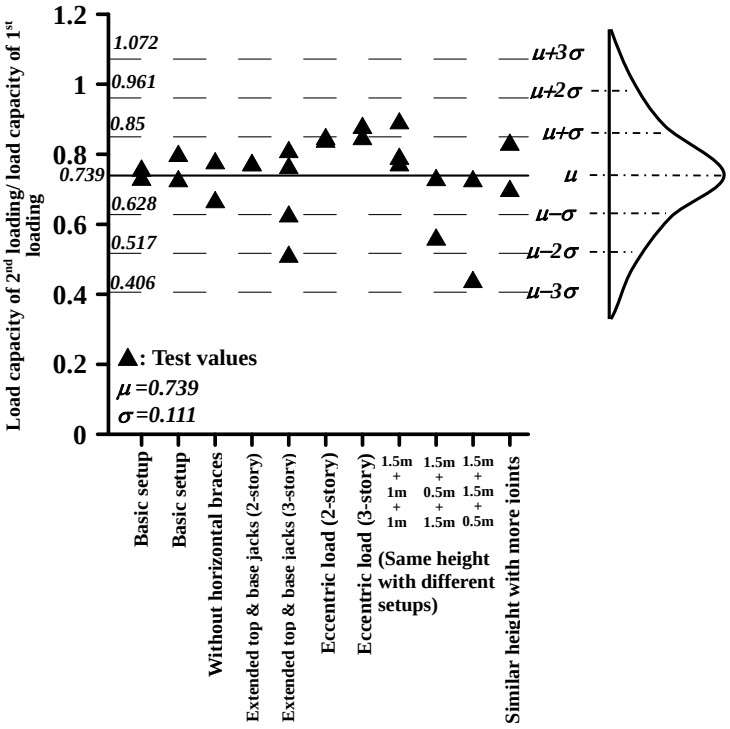

Figure 24. Scatter Plot of Average Strength Reduction Factors (ϕ) of Reusable Independent Heavy-duty Scaffolds based on $\mu\pm\sigma$ to $\mu\pm3\sigma$

Figure 24 shows that most of the strength reduction factors (ϕ) are located in the area of the average value plus or minus two standard deviations ($\mu\pm2\sigma$) with the exception of only one test (same height with 1.5m+1.5m+0.5m triangle-type scaffold units). During the first loading, the specimen was overloaded and unloaded too late, so it was too seriously damaged to serve as "reusable materials". This value may consider to be deleted.

Additionally, engineers may perform independent heavy-duty scaffold structural design at construction sites by referring to the strength reduction factors of reusable scaffolds shown in Figure 24 based on safety requirements. The strength reduction factor (ϕ) of reusable scaffolds with one standard deviation is 0.628 ($=\mu-\sigma=0.739-0.111$). The reduction factor (ϕ) of reusable scaffolds with two standard deviations is 0.517 ($=\mu-2\sigma=0.739-2\times0.111$). The strength reduction factor (ϕ) of reusable scaffolds with three standard deviations is 0.406 ($=\mu-3\sigma=0.739-3\times0.111$). In this study, the strength reduction factor (ϕ) based on two standard deviations is appropriate for the structural design of independent heavy-duty scaffolds used in constructions.

5.11 Comprehensive Comparisons

Figure 25 compares the load capacities of all the independent heavy-duty scaffolds tested in this study. Figure 25 shows that the load capacity of three-story independent heavy-duty scaffolds does not significantly differ from that of two-story independent heavy-duty scaffolds. Situations of double eccentric loading L/3 and rustiness scaffolds reduce the most load capacity of independent heavy-duty scaffolds. If the heights are similar, independent heavy-duty scaffolds assembled in the three different setups with the same number of joints have similar load capacities. The load capacity of three-story independent heavy-duty scaffolds assembled with 110 cm triangle-type scaffold units is higher than that of the two-story basic setup.

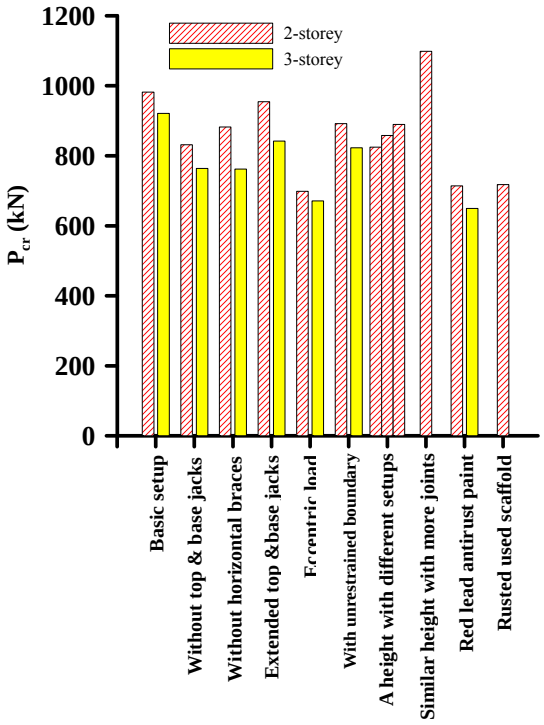

Figure 25. Comparisons of Load Capacities of Various Independent Heavy-duty Scaffold Setups

Figures 26 and 27 show the load capacities of various setups of two-story and three-story independent heavy-duty scaffolds comparing with those of the two-story and three-story basic setups respectively. Based on the load capacities of the two-story and three-story basic setups, the percentage of the load capacities of various setups of independent heavy-duty scaffolds to those of two- and three-story basic setups can be obtained.

The load capacities of two-story and three-story aging independent heavy-duty scaffolds treated with red lead antirust paint are 73% and 71%, respectively, of the capacities of their basic setup counterparts. The load capacity of two-story reusable independent heavy-duty scaffolds assembled with rusted surfaces is 73% of that of the basic setup counterpart. The test results are consistent with the average strength reduction factor of load capacities of reusable independent heavy-duty scaffolds 0.739 (see Table 2 and Figure 24). These results show that the reduced load capacities of aging independent heavy-duty scaffolds treated with red lead antirust paint or have rusted surfaces are similar to the average strength reduction factor (ϕ_μ) observed in the simulation of lower strength bounds of reusable scaffolds.

As shown by the test results, the second loading method used in this study to simulate the lower strength bounds of reusable scaffolds has a good practical value. Based on the average strength reduction factor (ϕ_μ) of simulated lower strength bounds of reusable scaffolds, designers can choose proper strength reduction factors for reusable scaffolds based on safety requirements to perform structural design for independent heavy-duty scaffolds.

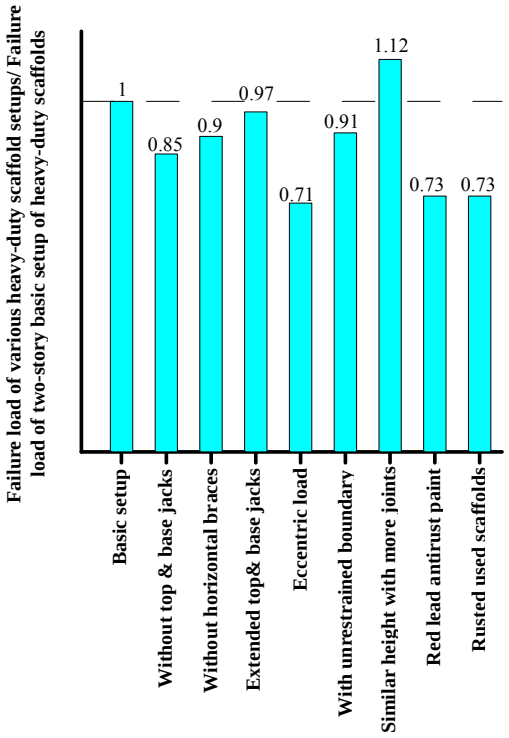

Figure 26. Comparisons of Load Capacities between Various Two-story Independent Heavy-duty Scaffold Setups and Two-story Basic Setup

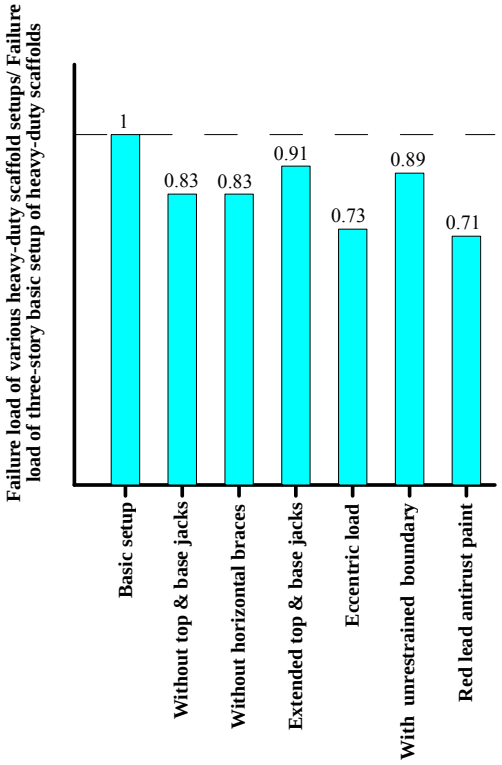

Figure 27. Comparisons of Load Capacities between Various Three-story Independent Heavy-duty Scaffold Setups and Three-story Basic Setup

6. CONCLUSIONS

This study investigated the stability of various setups of independent heavy-duty scaffolds commonly used on construction sites in Taiwan. The following conclusions and suggestions are based on the results of experiments performed in two-story and three-story scaffolds:

1. The load capacity of three-story independent heavy-duty scaffolds is not significantly lower than that of two-story independent heavy-duty scaffolds. The top and base screw jacks provide extra bending moment stiffness for independent heavy-duty scaffolds. Thus, seriously deformed top and base screw jacks are not safe for use in independent heavy-duty scaffolds. Since horizontal braces can enhance the load capacity of independent heavy-duty scaffolds and the stable during lifting and moving scaffolds, they cannot be neglected when assembling independent heavy-duty scaffolds. Extension of the top and base screw jacks does not substantially affect the load capacity of independent heavy-duty scaffolds. Thus, the height of top and base screw jacks can be adjusted to suit the internal clearances and landforms of the building. For a given height, independent heavy-duty scaffolds are assembled with different sizes of triangle-type scaffold units, as long as the number of joints is the same, the load capacities are similar. In addition, test results show that all vertical members of scaffolds can take most total vertical loads, but the tube forces of horizontal ledgers are unobvious.
2. This study revealed that the load capacity of independent heavy-duty scaffolds with such conditions as double eccentric loading L/3 and aging scaffolds treated with red lead antirust paint or rusted surfaces is decreased by approximately 30%. These strength affecting factors should be taken into account when engineers perform structural design for independent heavy-duty scaffolds.
3. The average of strength reduction factors (μ) of simulated lower strength bounds of reusable scaffolds is 0.739 and the standard deviation (σ) is 0.111. The strength reduction factors (ϕ) of reusable scaffolds minus one, two and three standard deviations are 0.628, 0.517 and 0.406 respectively. When performing structural design for independent heavy-duty scaffolds, engineers can choose proper strength reduction factors for reusable scaffolds based on their safety requirements. The reduction in load capacity of reusable independent heavy-duty scaffolds treated with red lead antirust paint or rusted surfaces is similar to the average reduction factor (0.739) for lower strength bounds of reusable scaffolds, indicating that the second loading method used in this study to simulate the lower limit value of the strength of reusable scaffolds has pretty good reliability and usability.
4. The boundary lateral displacement tests revealed the difficulty of simulating lateral displacement of the boundary in the testing laboratory. The load capacity of three-story independent heavy-duty scaffolds assembled with 110 cm triangle-type scaffold units is higher than that of the two-story basic setup with 150 cm triangle-type scaffold units. This implies that 110 cm triangle-type scaffold units provide a stronger scaffolding structure compared to 150 cm triangle-type scaffold units.

ACKNOWLEDGEMENT

The authors would like to thank the Ministry of Science and Technology, for funding this study (MOST 106-2221-E-224-016), Hua Construction Ltd. for sponsoring independent heavy-duty scaffolds as test materials, and Mr. Jian, Ming-zhi for assistance with experiments.

REFERENCES

[1] Zhang, H., Chandrangsu, T. and Rasmussen, K.J.R., "Probabilistic study of the strength of steel scaffold systems", Structural Safety, 2010, Vol. 32, pp.393-401.

[2] Weesner, L.B. and Jones, H.L., "Experimental and Analytical Capacity of Frame Scaffolding ", Engineering Structures, 2001, Vol. 23, No. 6, pp.592-599.

[3] Yu, W.K. and Chung K.F., "Prediction on Load Carrying Capacities of Multi-storey Door-type Modular Steel Scaffolds", Steel and Composite Structures, 2004, Vol. 4, No. 6, pp.471-487.

[4] Yu, W.K., Chung, K.F. and Chan, S.L., "Structural Instability of Multi-storey Door-type Modular Steel Scaffolds", Engineering Structures, 2004, Vol. 26, pp.867-881.

[5] Peng, J.L., Pan, A.D., Rosowsky, D.V., Chen, W.F., Yen, T., and Chan, S.L., "High Clearance Scaffold Systems during Construction – I. Structural Modelling and Modes of Failure", Engineering Structures, 1996, Vol. 18, No. 3, pp.247-257.

[6] Peng, J.L., Rosowsky, D.V., Pan, A.D., Chen, W.F., Chan, S.L., and Yen, T., "High Clearance Scaffold Systems during Construction – II. Structural Analysis and Development of Design Guidelines", Engineering Structures, 1996, Vol. 18, No. 3, pp. 258-267.

[7] Peng, J.L., Ho, C.M., Lin, C.C., and Chen, W.F., "Load-Carrying Capacity of Single-Row Steel Scaffolds with Various Setups", Journal of Advanced Steel Construction, 2015, Vol. 11, No. 2, pp.185~210.

[8] Peng, J.L., Wang, P.L., Huang, Y.H., and Tsai, T.C., "Experimental Studies of Load Capacities of Double-Layer Shoring Systems", Journal of Advanced Steel Construction, 2010, Vol. 6, No. 2, pp.698-721.

[9] Peng, J.L., Yen, T., Kuo, C.C., and Chan, S.L., "Analytical and Experimental Bearing Capacities of System Scaffolds", Journal of Zhejiang University SCIENCE A, 2009, Vol. 10, No. 1, pp.82-92.

[10] Liu, H., Zhao, Q., Wang, X., Zhou, T., Wang, D., Liu, J., and Chen, Z., "Experimental and Analytical Studies on the Stability of Structural Steel Tube and Couple Scaffolds without X-bracing", Engineering Structures, 2010, Vol. 32, No. 4, pp.1003-1015.

[11] Peng, J.L., Ho, C.M., Chen, C.Y., and Yang, Y.B., "Experimental Study on Load Capacities of Isolated Heavy-Duty Scaffolds Used in Construction", Journal of Advanced Steel Construction, 2014, Vol. 10, No. 3, pp.248~273.

INFLUENCE OF EXECUTION TOLERANCES FOR FRICTION CONNECTIONS IN CIRCULAR AND POLYGONAL TOWERS FOR WIND CONVERTERS

Christine Heistermann [1], Marko Pavlović [1,4,*], Milan Veljković [1,4], Daniel Pak [2,5], Markus Feldmann [2],Carlos Rebelo [3] and Luis Simões da Silva [3]

[1] *Steel Structures, Luleå University of Technology, 97187 Luleå, Sweden*
[2] *Institute for Steel Construction, RWTH Aachen University, Mies-van-der-Rohe-Straße 1, 52074 Aachen, Germany*
[3] *ISISE; Department of Civil Engineering, University of Coimbra, Rua Luís Reis Santos, Pólo 2, 3030-788 Coimbra, Portugal*
[4] *Delft University of Technology, Faculty of Civil Engineering and Geosciences, Stevinweg 1, 2600 GA Delft, The Netherlands*
[5] *Universität Siegen, Paul-Bonatz-Str. 9-11, 57076 Siegen, Germany*

**(Corresponding author: E-mail: m.pavlovic@tudelft.nl)*

Received: 9 June 2016; Revised: 15 August 2016; Accepted: 29 October 2016

ABSTRACT: Friction connections with long open slotted holes have been proven to be a competitive alternative to the conventional flange connections in steel tubular towers for wind energy converters. As full-scale tests are not available, results of Finite Element Analysis (FEA) of the real-scale tower geometry are used in this paper to investigate the influence of tower cross section shape, execution tolerance (gap between the shells) and length of the connection on the bending resistance. Buckling behaviour of the shell in the vicinity of the friction connection in circular and polygonal towers is compared. The friction connection is thoroughly examined and recommendations for execution tolerances are given. The influence of two types of the execution tolerances on the connection strength is considered: inward bended "fingers", leading to inclined gaps, and a parallel gap created by different tower diameters.

Keywords: steel tubular tower, wind energy converter, friction connection, long open slotted hole, circular cross section, polygonal cross section, execution tolerance, FEA

DOI: 10.18057/IJASC.2017.13.4.2

1. INTRODUCTION

Steel tubular towers are the most common support for wind energy converts. They reach heights up to 100 m, which is limited by the size of the shell diameter of up to 4.5 m. Transportation issues impose the maximum value for shell diameter. In recently finished RFCS (Research Fund for Coal Steel) projects, "High-strength tower in steel for wind turbines (HISTWIN)" Veljkovic et al. [1] and "High steel tubular towers for wind turbines (HISTWIN2)" Veljkovic et al. [2], the use of technical innovations to increase competiveness of steel tubular towers was one of the main topics. One important innovation is the use of so-called "friction connections with long open slotted holes" for in-situ execution, see Figure 1. This connection has been shown as a competitive alternative to the conventional ring flange connection of the steel tubular tower for a hub-height up to 100 m. The material cost for the connection, which takes into account shell material and bolts, is about 80 % lower for the adequate resistance, according to Veljkovic et al. [1].

In the friction connection, the outer shell (upper segment) is equipped with fitted bolts, close tolerance holes, on the side of the bolt head, while the inner shell (lower segment) has open slotted holes with the width of the hole equal to the normal clearance hole diameter, see Figure 1. Feasibility tests on tower segments, 2 m in diameter, carried out within HISTWIN and HISTWIN2 project, Veljkovic et al. [1] and [2], proved that the bolts can be pre-installed in the

upper segment and easily slid on top of the lower segment with an execution tolerance providing a 10 mm initial gap between the shells, see Figure 2. Diameters of towers with common height of 80 – 100 m are large e.g. up to 4 m and thicknesses of shells can go up to 60 mm, depending on site condition, wind turbine class, and steel grade used. As a rule of thumb, the initial shell thickness which can be assumed for the pre-designed considerations is about 1% of the shell diameter. Therefore, relatively larger execution tolerances are needed for the execution of real-scale tower.

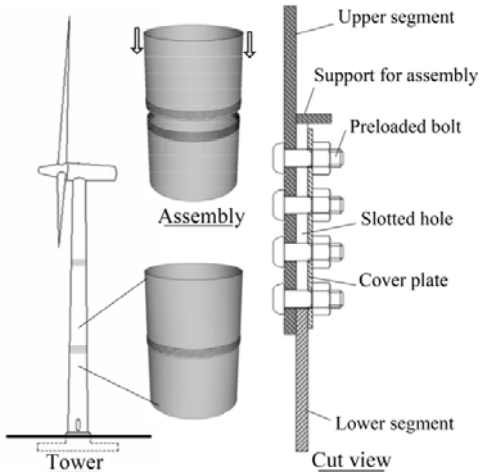

Figure 1. The Friction Connection in Tower for Wind Converters, Veljkovic et al. [1]

a) HISTWIN Project [1] b) HISTWIN2 Project [2]

Figure 2. Feasibility Tests Performed in Previous Projects

Down-scale experiments on tower segments with friction connection have been conducted within the scope of HISTWIN project, Veljkovic et al. [1], but neither tests or field measurements are available with real dimensions of a tower. It is worth noting that photos shown in Figure 2 show feasibility testing which is performed so the upper segment of the tower is placed at the ground. This choice is made by workers in the workshop, just for their convenience, this decision has no consequences on any conclusion relevant for the research project.

It is unrealistic to expect that experiments up to failure of such large specimens will ever be realised, especially having in mind the possibilities of advanced FEA as demonstrated in this paper. Thorough examination of slip and buckling behaviour of the friction connection in a tower with circular cross section is given by Pavlović et al., [3] and [4], respectively. The time dependent loss of the bolt preloading force in the friction connection has been considered in Heistermann et al. [5]. Polygonal tower shapes have been studied by Garzon [6] and Reinke [7], providing numerical and

experimental evidences on the buckling behaviour of tower segments with polygonal cross section, respectively. The friction connection in polygonal towers has been reported in the HISTWIN2 project, Veljkovic et al. [2].

The aim of the research presented here, is to comprehensively examine the behaviour of the friction connection in circular and polygonal towers including the influence of local buckling of the shell in the vicinity of the connection and the influence of execution tolerances. Quasi-static analysis is made with ABAQUS FE software package, see [8], using the explicit dynamic solver coupled with damage material models. The assumed tower segment has a diameter of the shell of D = 3374 mm, thickness t = 24 mm, steel grade S460 and high-strength bolts M48, grade 10.9, are used for the connection. Details of the connection are shown in Figure 3. Dimensions and values of design loads (M_{Ed} = 45.8 MNm) at the analysed connection cross section are based on the design of a "real" tower with the common ring flange connection. Local buckling of the shell in the vicinity of the friction connection is analysed considering design shell imperfections in the circular and the polygonal tower.

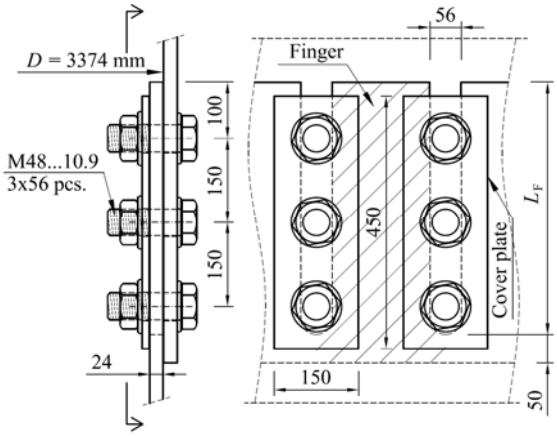

Figure 3. Layout of the Friction Connection in a Real-scale Tower Considered in the Study

A possible solution to ensure the execution tolerance is the provision of a gap between the outer and the inner shell obtained by different diameters. The second alternative is to pre-bend "fingers" of the inner shell which has the same outer diameter as the inner diameter of the outer shell. These alternatives and the size of the execution tolerance are examined in this study.

In order to validate the FE modelling and the computational procedure, the experimental results of the down-scale 4-point bending tests conducted by Pak and Naumes [9] on 8 mm thick shells with a diameter of 1 m and the total span of about 7 m are used.

2. FINITE ELEMENT ANALYSIS

Two FE models of the friction connection shown in Figure 3 are created: a connection in a tower with circular cross section (FCC) and a connection in a tower with polygonal cross section (FCP), as shown in Figure 4. The friction connection is designed with three rows of 56 bolts each, and cover plates to have sufficient slip resistance so that the buckling resistance of the connection becomes the dominant failure mode.

The polygonal tower shape has 14 edges (folds). The governing criterion for such division is to be at the boundary to local buckling of a flat part of the cross section, a segment between the folds, i.e. keeping the slenderness of the flat part close to the lower limit for the cross section of class 4 according to EN 1993-1-1 [10], see Eq. 1 and Eq. 2.

$$c_{\text{flat}} / t \le 42\varepsilon \Rightarrow c_{\text{flat}} \le 42 \cdot 0.71 \cdot 24 = 716\,\text{mm} \tag{1}$$

$$n_{\text{edge}} \ge \frac{\pi D}{c_{\text{flat}}} = 14.8\,. \tag{2}$$

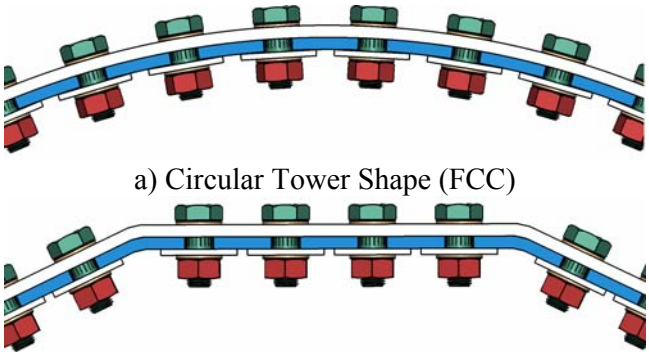

a) Circular Tower Shape (FCC)

b) Polygonal Tower Shape (FCP)

Figure 4. Different Tower Shapes Considered in the Case of Friction Connection

2.1 Geometry, Boundary Conditions and Mesh

The FEA model geometry and boundary conditions of one half of the tower segment including the most possible refinement of the connection details shown in Figure 5 and Figure 6. Symmetry boundary conditions for bending are used to reduce the computation time. The tower segment is 3 m long on each side of the connection. This size of the model is chosen for proper modelling of the connection, local buckling of the shell and to allow redistribution of meridional stresses. Preliminary FEA was used to justify dimensions and costs of the feasibility tests which has been confirmed by the detailed analysis shown here. Cross section surfaces of the shells are fully kinematically constrained to the reference points.

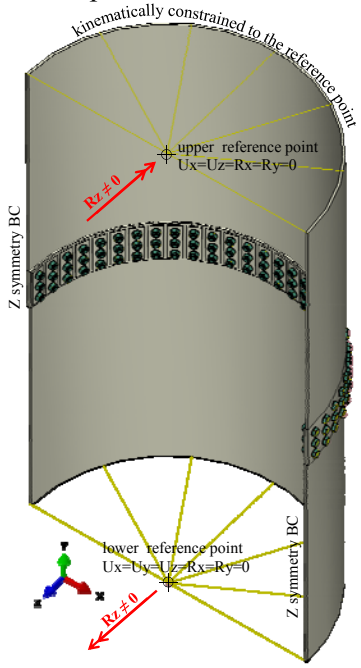

Figure 5. Geometry of the Model and Boundary Conditions

Bolts and nuts are modelled with the real thread geometry, see Figure 6 and preloading of the bolts is applied by the turn-of-nut method, see Figure 7. Tetrahedron solid elements (C3D4) are used to form the bolt mesh. Global element size of the bolt is 11 mm, while in the threaded zone the element size is reduced to 5 mm. Eight node hexahedron solid elements with reduced integration (C3D8R) are used for the shell with element size of 20 mm. The shells and the cover plates are meshed with four elements through the thickness to properly take into account the bending stiffness.

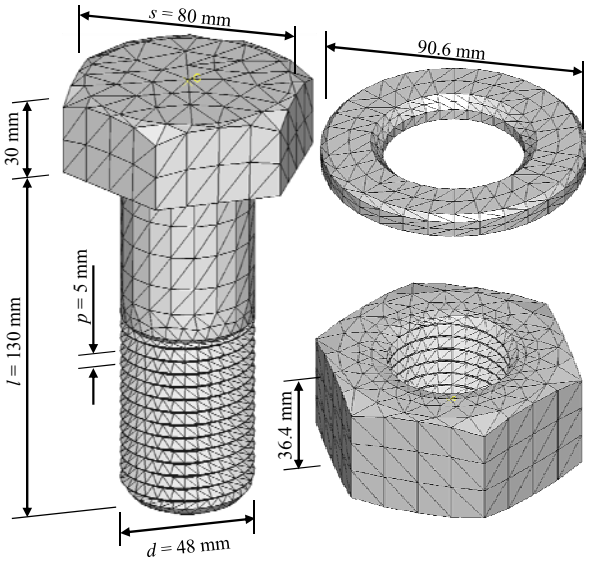

Figure 6. Geometry and Mesh of the Bolt, Washer and Nut

General contact interaction procedure is used in ABAQUS/Explicit with “hard” formulation of normal behaviour and “penalty” friction formulation of tangential behaviour, see [8]. The friction coefficient of 0.14 is set for bolts and nuts threads surface pairs according to recommendation given in ECCS Publication No. 38 [11]. For all other surface pairs in the model a nominal Class A friction surface is assumed with the slip factor $\mu = 0.5$ according to EN 1993-1-8 [12] in the parametric study performed here. The sophisticated modelling of bolts is necessary to have appropriate stiffness of the bolt and connection, however the full benefits of its complex analysis are emphasised at the ultimate limit state of the connection, see references [2], [3], [4], and Pavlovic et al. [13].

2.2 Loading and Computational Procedure

Two computation steps are analysed for each model: preloading of the bolts and bending to the failure. Preloading of the bolts is applied by the turn-of-nut method. Hexagon edges of nuts are kinematically coupled to the reference points in the centre line of each nut, as it is shown in Figure 7a. Those reference points are turned by applying changes in boundary conditions, i.e. by rotating around the axis parallel to the shank of each bolt. The targeted preloading force of 960 kN is calculated according to EN 1993-1-8 [12] for M48 bolts, grade 10.9. Rotations of the nuts are calibrated in each case to achieve this targeted preloading force. Values of the bolt preloading forces are obtained by summation of node forces in the cross section of the bolt, see. In Figure 7b, the stress in the bolt, shells and cover plate in the friction connection are shown for the final stage of preloading.

Table 1. Rotations of the Nuts and Resulting Preloading Forces

Case	Grip length (mm)	Gap (mm)	Nut rotation (rad)	Obtained preloading force (kN)
FCC	60	0	3.83	960
	60	10	16.40	1024
	60	20	28.95	892
	60	30	41.52	893
FCP	60	0	1.00	905
	60	10	13.60	964

The bending moment is applied "displacement controlled" by imposing rotations of upper and lower reference point as shown in Figure 5.

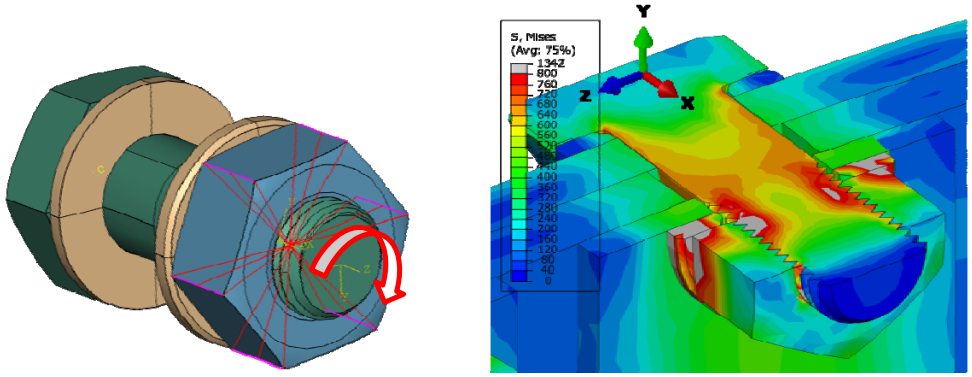

a) The Turn-of-nut Method b) Stresses in the Bolt, Shells and Cover Plate

Figure 7. Preloading of the Bolts

Explicit dynamic solver of ABAQUS is known to be robust for this kind of analysis, where complex contact interactions coupled with large deformations and nonlinear behaviour are present, see [8]. It does not have usual convergence problems such as the implicit static solver. However, the computation may be quite long, if the real dynamic response of the model is required. Loading is supposed to be quasi-static. In this model the dynamic solver is used to efficiently solve the quasi-static problem. Calculation time is shortened by using variable non-uniform mass scaling technique with the target time increment set to $\Delta t = 5.0 \times 10^{-5}$ s. Artificial durations are adopted for two computation steps: 7 s and 10 s, for preloading of the bolts and loading up to failure, respectively. Trial computations are made in order to select the appropriate target time increment and to avoid unwanted inertia forces in quasi-static FEA.

2.3 Material Models

Measured data of material properties are used for the verification FEA, while nominal material values are used for the bolts and the shells in the real-scale FEA, as given in Table 2. Isotropic hardening plasticity with modulus of elasticity of $E_0 = 210$ GPa, and Poisson's ratio of $\nu = 0.3$ is used for all materials. Bolts, washers and nuts are set to nominal values of stress at the yield point $f_y = 900$ MPa and ultimate strength $f_u = 1000$ MPa, with the ultimate elongation $A = 10$ % according to ISO 898-1 [14] for bolt material grade 10.9, see Figure 8. A parabolic shape of the nominal stress-strain curve is assumed to enable the definition of the damaged plasticity material model of bolts.

Table 2. Material Properties used in FEA

Material	Steel grade	Thickness t (mm)	Yield strength f_y (MPa)	Ultimate strength f_u (MPa)	Ultimate elongation A (%)
Down-scale verification FEA	S355J2+N	8	415	534	-
High-strength bolts	10.9	-	900	1000	10
Shells in real-scale FEA	S460	24	460	550	-

A ductile damage model is used to model the failure of the bolts. The hardening part of the material behaviour is defined by the plasticity curve while the softening part and the failure are governed by the damage initiation criterion and the damage evolution law. Parameters of ductile damage initiation criterion and damage evolution law are derived analysing undamaged and damaged material response in a standard (round bar) tensile test, as described by Pavlović et al. [145]. The standard (round bar) tensile test model is created and material parameters are calibrated by comparing the nominal stress-strain curve to the FE results, as shown in Figure 8. Details of the calibration procedure for the material models of the bolt are given by Pavlovic et al. 3].

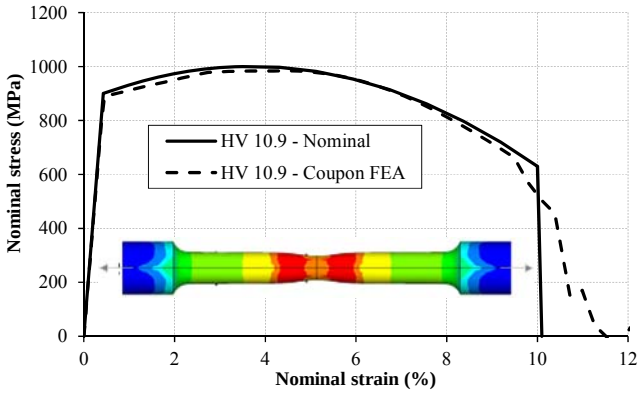

Figure 8. Comparison of Nominal and FEA Tensile Tests Results for Bolts

The same element type (C3D4) and corresponding size (5.0 mm) used in the validation of the material model is used for bolts in the FE models of real-scale connections.

2.4 Verification of FEA by Down-scale Experiments

In order to prove the validity of the FEA study presented here, verification is made with respect to the experimental data of down-scaled tests of tower segments. The layout of the 4-point bending experiments conducted at RWTH Aachen University, see Veljkovic et al. [1] and Pak and Naumes [9], is shown in Figure 9a. The ring flange connection and the friction connection using 32 M20 bolts and 24x3 M20 bolts, respectively, were tested with shell diameter 1 m and thickness 8 mm over a 7 m span. The same computational procedure, which is used for the verification of FEA, is used for the real dimensions of the tower segment in this study.

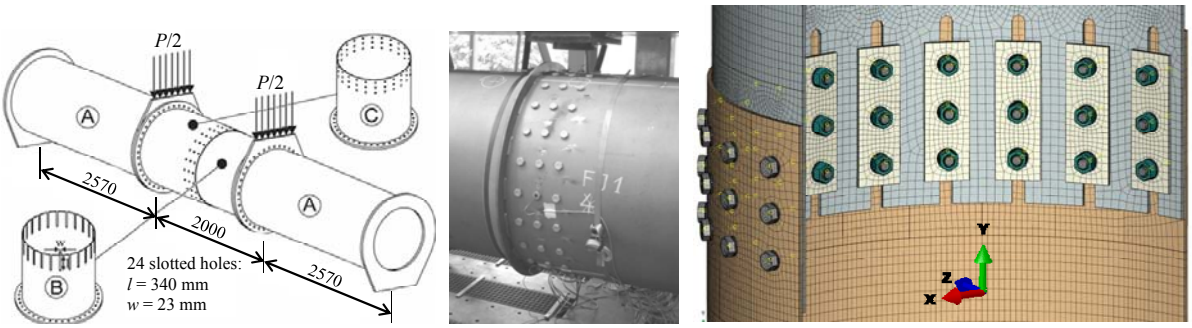

a) test set-up b) detail of the connection c) FE model

Figure 9. Experiments and FE Model of the Down-scaled Tower Segment

Comparisons of the experimental and FE results for the friction connection are shown in Figure 10. More details about verification of FEA are given by Pavlovic et al.]. Very good agreement is achieved for both failure modes buckling of the shell in case of the ring flange connection and slip failure for the specimen where the friction connection is used. This has justified use of the same FE model for analysis of the full scale connections.

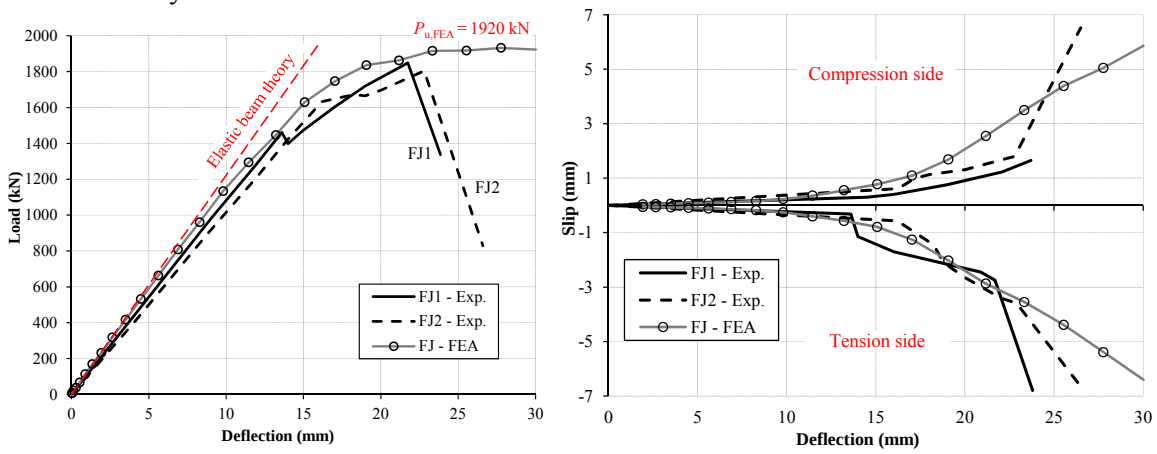

a) load-deflection curves b) slip at the end of finger

Figure 10. Results of the Verification FEA vs. Experiments on the Friction Connection

2.5 Shell imperfections

Friction connections in circular and polygonal tower shapes, FCC and FCP, respectively are firstly analysed with and without shell imperfections in the compression zone. For the circular tower shape (FCC) a dimple imperfection is applied, as shown in
Figure **11**a, with a maximum amplitude of 13 mm calculated according to EN 1993-1-6 [15] assuming the fabrication tolerance quality class B. For the polygonal tower shape (FCP) a harmonic shape of the local imperfection is applied, as shown in
Figure **11**b. The maximum amplitude of the harmonic imperfection of 4 mm is assumed as approximately $b/200$, where b is the width of the flat part of the polygonal cross section between two folds. The position of the imperfection is obtained from non-linear analysis of the initially ideal geometry, see Figure 15. This initial deformation is introduced in the subsequent model under a stress-free conditions.

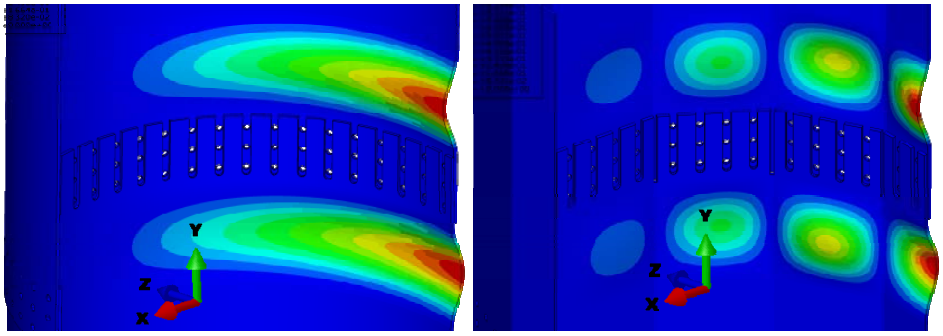

a) circular cross section (FCC) b) polygonal cross section (FCP)

Figure 11. The Imperfections Applied to the Shell, Adjacent to the Connection

2.6 Execution Tolerances

A parametric study of the friction connection's bending resistance regarding the execution tolerances is made analysing several parameters: tower shape, length of the connection (length of the "finger"), and type and size of execution tolerance. Two different types of execution tolerances are considered for the friction connection in circular tower: a gap between the shells due to different diameters of the segments and an inclined gap due to bending of fingers, as it is shown in Figure 12. Both alternatives are investigated for the maximum gap in the range of 10 – 30 mm.

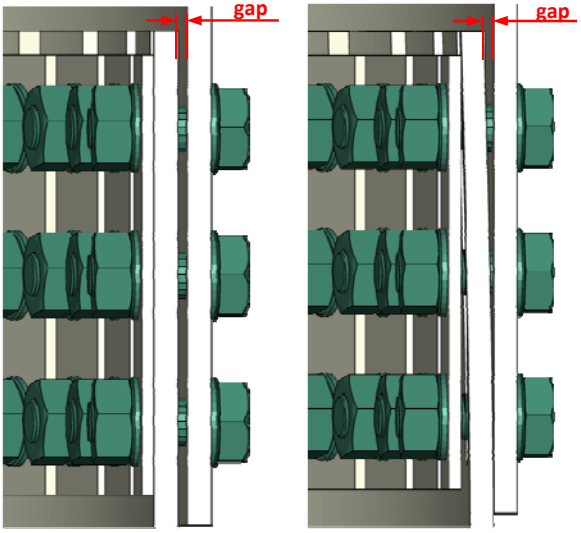

a) parallel gap between the shells b) inclined gap due to bending of the fingers

Figure 12. Different Types of the Execution Tolerances.

Denomination of the cases considered in the parametric study is given in Table 3. The first letter indicates the tower shape (C – circular, P – polygonal), the second is the digit designating the size of execution tolerance (0 means no gap, 1 means 10 mm gap, 2 means 20 mm gap, 3 means 30 mm gap). The third character denotes the steel grade of the shell (B means S460 in this study) and the remaining three digits represent the length of the fingers (L_F = 450 mm, L_F = 550 mm and L_F = 650 mm). The last lower case character defines the type of the execution tolerance (g – gap between the shells, b – inclined gap due to bending of the fingers). The overlapping length in the connection is 50 mm longer than the fingers in all cases, as shown in Figure 3. Reference cases, with ideal geometry (C0B450 and P0B450), have no gaps between the outer and the inner shell. No dimple imperfections of the shell are taken into account in the parametric study to isolate the problem of stress concentrations and buckling within the connection.

Table 3. Cases Considered in the Parametric Study

Case	Tower shape	Execution tolerance g (mm)	Length of the fingers (mm) L_F (mm)	Type of exec. tol.
C0B450	circular	0	450	none
C1B450g		10	450	gap
C1B550g		10	550	gap
C1B650g		10	650	gap
C2B450g		20	450	gap
C3B450g		30	450	gap
C1B450b		10	450	bending
C2B450b		20	450	bending
C3B450b		30	450	bending
P0B450	polygonal	0	450	none
P1B450g		10	450	gap
P1B450b		10	450	bending

In the polygonal tower with assumed execution tolerances, slots are cut at the corners in the connection zone, as shown in Figure 13, to allow the unrestrained deformation of the fingers during preloading of the bolts. For the sake of simplicity no rounded root of the slot in the fold is modelled. The width of those slots is 24 mm and the length is 50 mm longer then the fingers. No slots are made in the initial case with perfect geometry where no gap between the shells exists, P0B450.

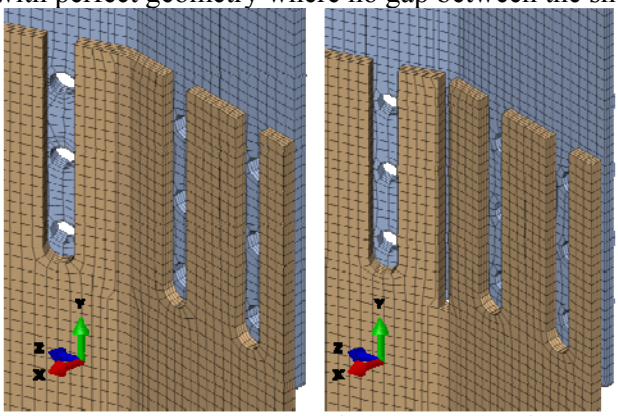

a) P0B450 b) P1B450g and P1B450b

Figure 13. Slots at the Corners in the Connection Zone of Polygonal Tower

3. RESULTS AND DISCUSSION

3.1 Number of Folds

According to the criteria for cross section classification given in EN 1993-1-1 [10], the number of edges (folds) in the tower with polygonal cross section is supposed to be $n_{edge} \leq 14.7$ to comply with the requirement for cross section class 4. The slenderness limit, Eq. 1, for the flat segments of the tower assumes that the folds have enough small angle, Eq. 3. For the tower considered here the angel between flat segments of 154^0 corresponds to the $n_{edge}=14$ according to eq.3. is too large to keep folds fixed. This is obvious from results of experiments performed by Tran [16]. Therefore the number is not supposed to be enough to to prevent its displacement at the ultimate limit state governed by the stability.

$$\alpha = \frac{\pi}{2}(1 - \frac{2}{n_{edge}}) \quad \text{for} \quad n_{edge} \geq 3 \tag{3}$$

This expectations is confirmed by the analysis performed. It is clearly shown in Figure 14 that the cross section undergoes global buckling characterized by the dominant radial movement of the folds. Larger number of folds will lead to the weaker folds and smaller number of folds will lead to slender segments, however the optimization of polygonal towers are left out of the scope of this paper.

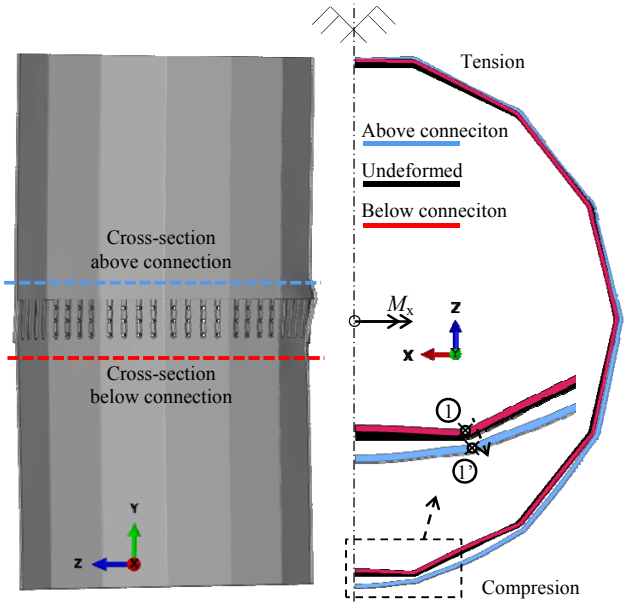

Figure 14. Buckling of the Polygonal Cross Section

3.2 Influence of the Shell Imperfections

Post-failure deformed shapes for both cross section cases obtained in FEA without initial dimple imperfections for finger length L_F = 450 mm are shown in Figure 15. Failure mode in both cases is local buckling of the shell, which includes rotation of the whole connection. This appears due to eccentricity of the single lap joint.

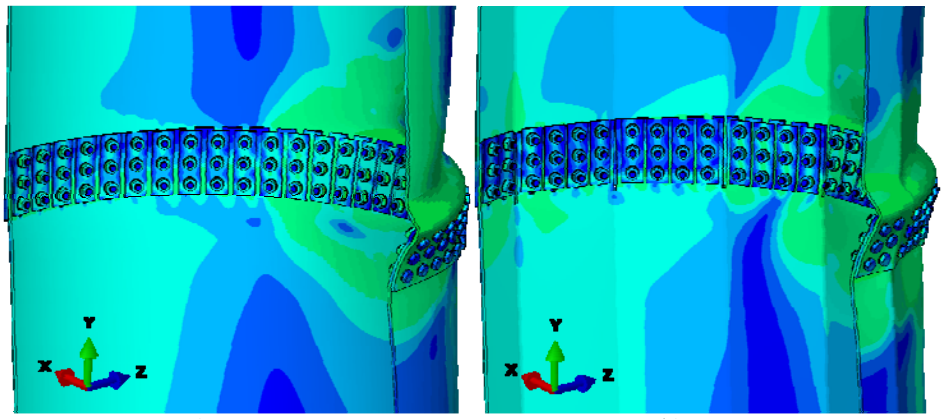

a) FCC b) FCP

Figure 15. Post-buckling Deformed Shapes for Connections without Shell Imperfections

Moment-rotation curves for FCC and FCP, with and without imperfections are shown in Figure 16. Initial stiffnesses are identical while the bending resistances are different. In both cases the ultimate buckling resistance $M_{b,Ru}$ calculated according to EN 1993-1-6 [15], assuming fabrication tolerance class B, is surpassed.

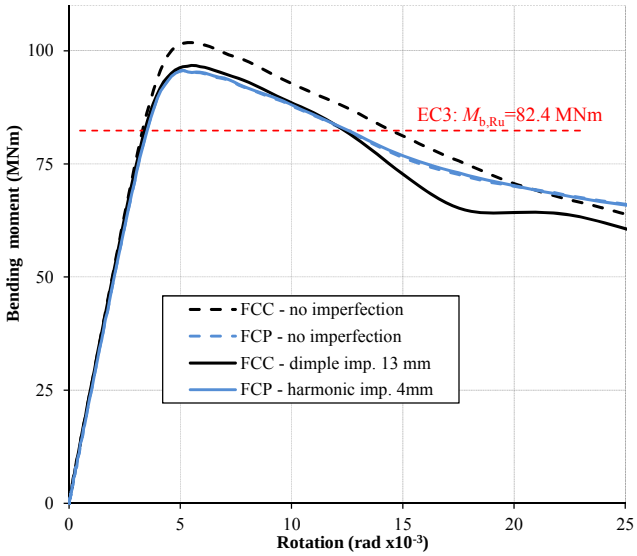

Figure 16. Moment-rotation Curves of FCC and FCP for Finger Length L_F = 450 mm

The bending resistance of the connection in the circular tower without imperfections is 5 % higher compared to the polygonal tower. However, the same ultimate bending moment is obtained in the friction connection in circular and polygonal tower: 96.8 MNm and 95.6 MNm, respectively, if imperfections are considered. This is expected as the harmonic imperfections introduced in the polygonal tower are smaller than the dimple imperfections introduced in the circular tower, 5 mm vs. 13 mm, respectively. The folds in the polygonal tower stiffen the cross section.

Table 4. Bending Resistances of FCC and FCP With and Without Design Shell Imperfections

Case	Imperfections		Bending resistance (MNm)		
	Shape	Size (mm)	Without imperfections	With imperfection	Influence of imperfection
FCC	Dimple	13	101.8	96.8	-5 %
FCP	Harmonic	4	95.7	95.6	0%

Deformed shapes and meridional stresses in the compression zone of the shell at the load step prior to buckling are shown in Figure 17 for FCC and FCP with design imperfections. Buckling shape in FCC is different compared to the case without imperfection. If imperfections are not considered, the shell local buckling is affected by eccentricity of the single lap joint resulting in an inclination of the whole connection, see Figure 15a. If the design imperfections are applied, buckling occurs in the zone of imperfection without inclination of the whole connection, see Figure 17a. In FCP shell imperfections are rather small, and similar buckling shape including the inclination of the connection can be seen in Figure 15b and Figure 17b. From the influence of design imperfections on the resistance it is clear that the circular tower is more sensitive to buckling of the shell, in the vicinity of the friction connection, compared to the polygonal towers.

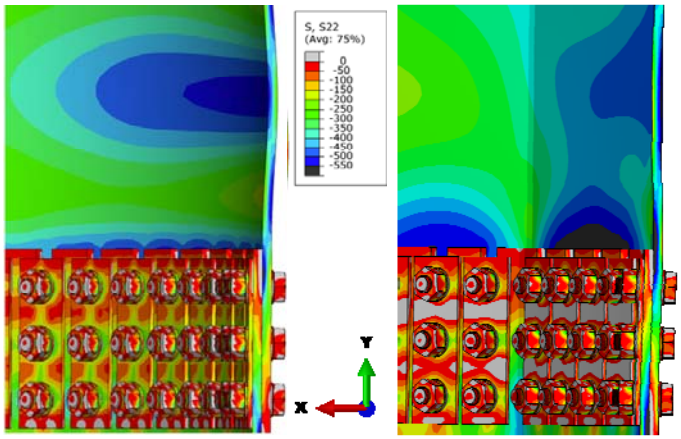

a) FCC (M = 90.7 MNm) b) FCP (M = 89.5 MNm)

Figure 17. Deformed Shapes and Meridional Stresses in the Shell Prior to Buckling

3.3 Influence of the Connection Length

Meridional stresses due to bending of the fingers by preloading of the bolts for different lengths of the fingers are shown in Figure 18. It can be noticed that the case with shortest fingers (C1B450) has the lowest meridional stresses since the gap is closed by the simultaneous deformation of upper and lower shell. In the other two cases (C1B550 and C1B650) closure of the gap between the shells is obtained by bending of the fingers, resulting in larger meridional stresses. Therefore, there is no use of providing long fingers in order to reduce normal stresses in fingers. Certainly, a bit longer slotted holes may be beneficial for alignment of the tower segments during the execution, but this aspect is not taken into account here but there are no structural reasons to use longer fingers, especially not if the inclined gap is obtained in inward bending of the fingers

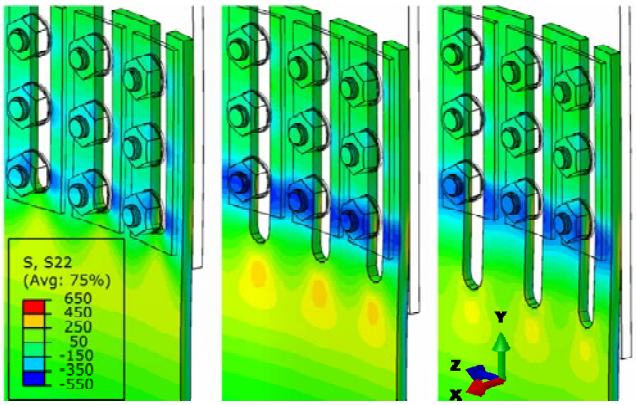

a) C1B450g b) C1B550g c) C1B650g

Figure 18. Meridional Stresses in the Fingers due to Closing of the Gap by Tightening of the Bolts

3.4 Influence of the tower shape

Moment-rotation curves for the friction connection with and without the gap of 10 mm in both circular and polygonal tower are shown in Figure 19. Reduction of the bending resistance due to execution tolerance is 2 % and 7 %, in circular and polygonal tower, respectively, compared to the cases without execution tolerances, see Figure 19 and
Table 5. The larger reduction in the polygonal tower is caused by the reduction of cross section area of the shell by applying the corner slots, see Figure 13. The plastic bending moment resistance of the cross section of the polygonal shell with corner slots $M_{p,Ru,red}$ = 116 MNm is 4.2 % lower than

the plastic bending moment resistance of the gross cross section $M_{p,Ru}$ = 121 MNm. This justifies the difference in reduction of bending moment resistance obtained for the polygonal and circular cross section.

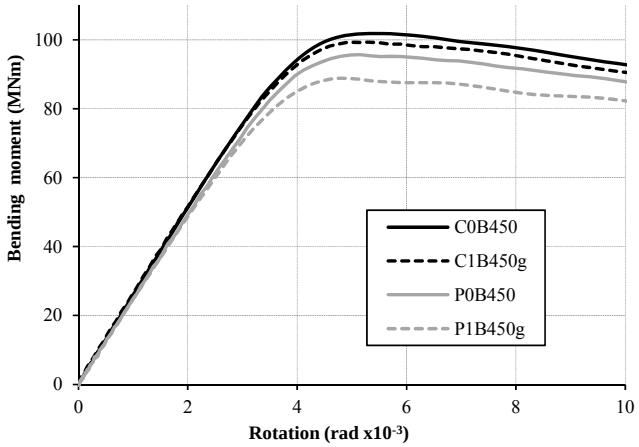

Figure 19. Influence of the Corner Slots in Polygonal Tower on Reduction of Bending Resistance

Table 5. Influence of the Tower Shape

Case	Tower shape	Execution tolerance g (mm)	Ultimate bending moment M_{ult} (MNm)	Reduction factor M_{ult}/ M_{ref}
C0B450	circular	0	101.8 (M_{ref})	1.00
C1B450g		10	99.3	0.98
P0B450	polygonal	0	95.7 (M_{ref})	1.00
P1B450g		10	88.9	0.93

Stress concentrations at the roots of the corner slots in the polygonal tower are caused by preloading of the bolts, see Figure 20b, which can reduce fatigue endurance of the shell. This needs to be assessed in more detail to justify the application of polygonal tower shapes in towers for wind converters (not scope of this study).

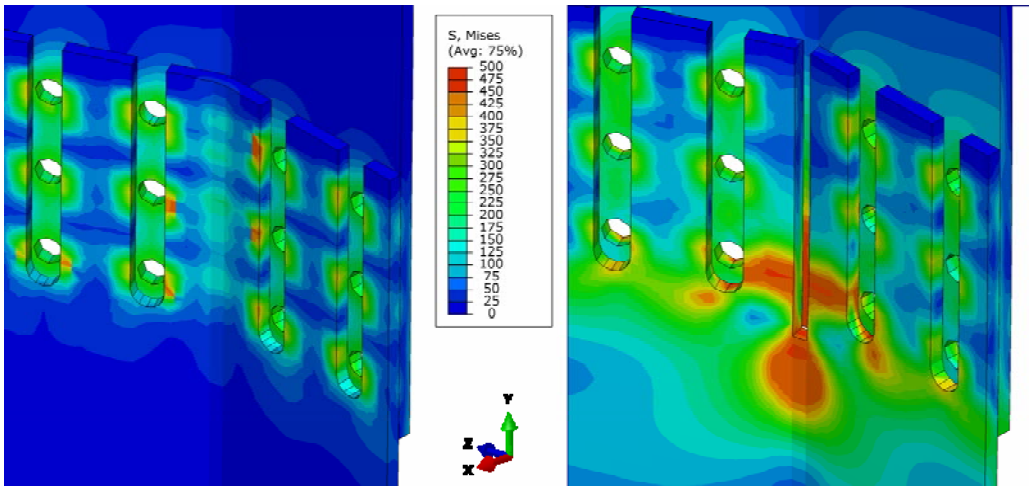

a) P0B450 b) P1B450g

Figure 20. Stress Concentration in the Corner Slot of the Polygonal Tower

3.6 Influence of the Type and Size of the Execution Tolerances

Two different methods to provide execution tolerances in the circular tower:

- the gap between the shells, parallel gap established by different diameters of two tower segments with and without fingers

- the same diameter of both tower segments but the inclined gap is established by inward plastic bending of the fingers.,

Different sizes:10 mm, 20 mm and 30 mm of the maximum gap , are compared to the reference (theoretical) cases of no gap, in Table 6. The reduction of bending resistance with regards to the parameters considered above is shown in Figure 21.

Table 6. Influence of the Type and Size of Execution Tolerance on Bending Resistance

Case	Type of the execution tolerance	Size of the execution tolerance g (mm)	Ultimate bending moment M_{ult} (MNm)	Reduction factor M_{ult}/ M_{ref}
C0B450	none	0	101.8 (M_{ref})	1.000
C1B450g	gap	10	99.3	0.975
C2B450g		20	96.7	0.950
C3B450g		30	94.4	0.927
C1B450b	Bending (inclined)	10	101.2	0.993
C2B450b		20	100.2	0.984
C3B450b		30	100.3	0.985

The effect of execution tolerance provided by the parallel gap between the shells leads to higher reduction of ultimate bending resistance compared to the inclined gap obtained by the inward bending of the fingers. Almost linear dependency of the reduction factor with regards to the size of the gap between the shells is obtained. With the largest execution tolerance of 30 mm gap between the shells 7 % reduction of the bending resistance is obtained. Inward bending of the fingers causes very small reduction, which is practically negligible. These results are expected as the less eccentricity is introduced in the tower segment at the connection, if the gap is made by inward bending of the fingers. This is illustrated in
Figure **22**, where deformed shapes and meridional stresses after preloading of the bolts and after the failure are shown for the reference case and the two types of execution tolerances.

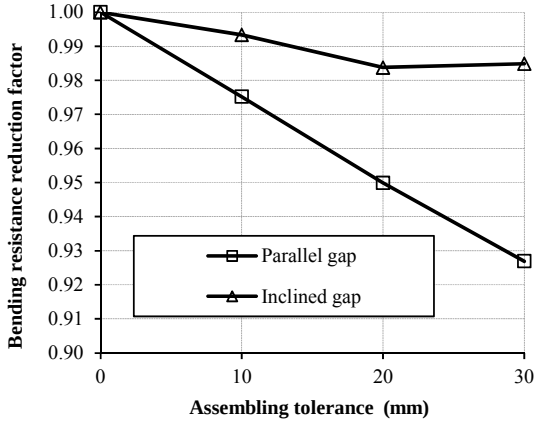

Figure 21. Influence of Execution Tolerances on Bending Resistance of the Connection

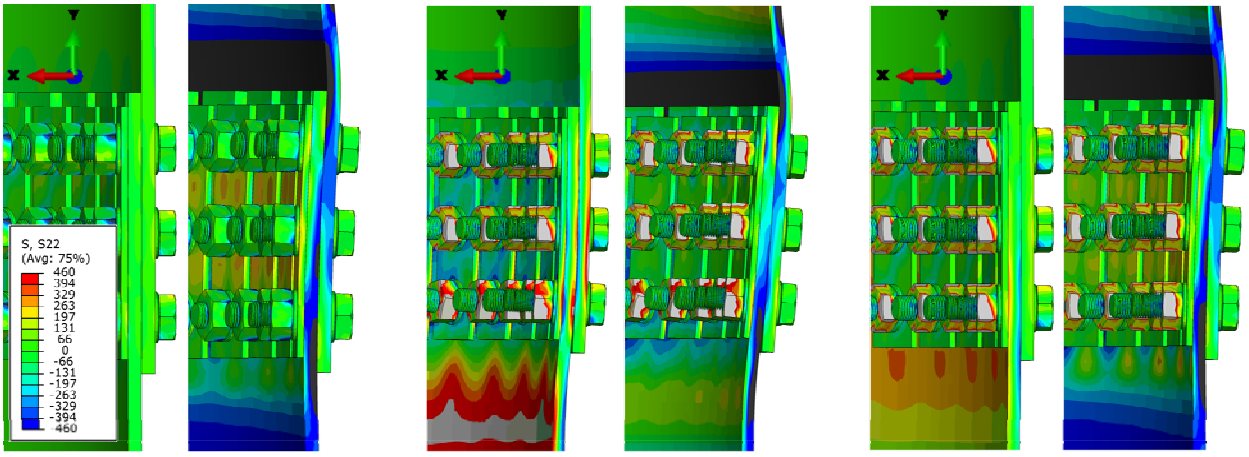

a) no execution tolerance C0B450 b) gap between the shells - C3B450g c) bending of the fingers - C3B450b

Figure 22. Deformed Shapes and Meridional Stresses after Preloading of Bolts and after Failure

Meridional stresses along the inner and outer edge of the fingers in the lower shell are shown in Figure 23 for different sizes and types of execution tolerances. Yielding criterion, $f_y = 460$ MPa, is reached below the fingers at $z \approx 650$ mm for the 30 mm parallel gap , see Figure 23a. The inclined gap is favourable since the meridional stresses are in elastic range, see Figure 23a. Moreover, preloading of the bolts is simpler if the fingers are pre-bent as they can be fully straightened by tightening of the lowest bolt row. Obviously the method of the inward finger bending for achieving the execution tolerances is advantageous.

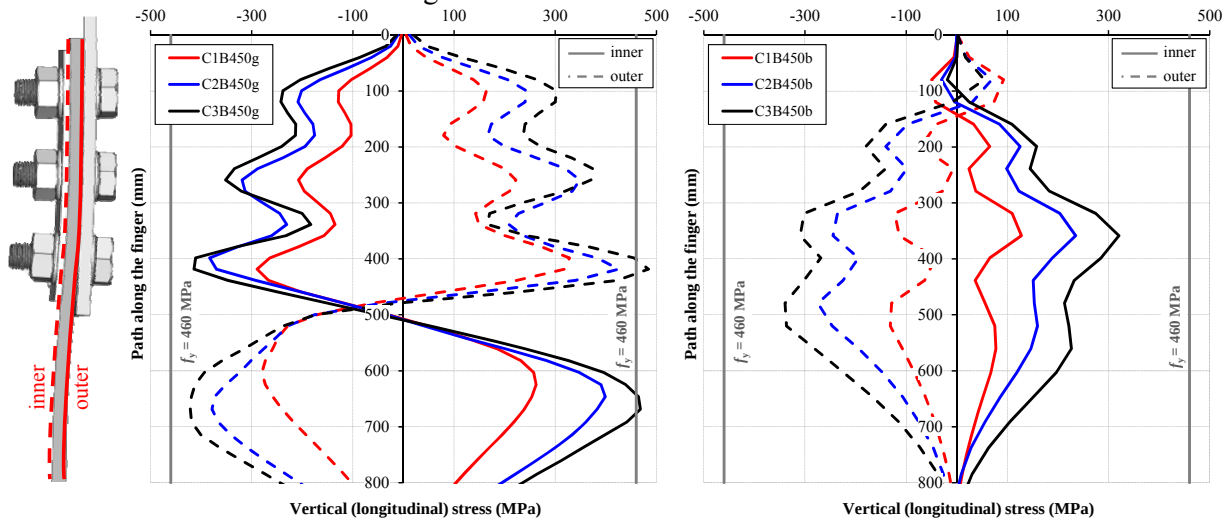

a) parallel gap b) inclined gap

Figure 23. Meridional Stresses along the Edges of Inner Shell after Preloading of the Bolts

4. CONCLUSIONS

Advanced FEA of the real-scale friction connection in a steel tubular tower for wind energy converter have been conducted, relaying on a FEA verified by down-scaled experiments. The friction connection is analysed in a parametric study considering circular and polygonal tower shape, design shell imperfection, length of the fingers, and size and type of execution tolerance. The following conclusions are drawn:

1. Provision of the execution tolerance by a parallel gap between the shells higher than 20 mm produces yielding in the root of the fingers. The bending resistance of the connection is 7 % reduced for an execution tolerance of 30 mm gap. This method is not recommended for larger execution tolerances. Execution tolerance provided by inward bending of the fingers is recommended. In this case, the inclined gap, practically no reduction of bending resistance is obtained up to a maximum tolerance of 30 mm.
2. The polygonal cross section of the tower is fully effective and no local buckling of the flat part occurs if the number of edges is chosen such that the flat part of the cross section satisfies the slenderness limit for the class 3 cross section according to EN 1993-1-1 [10].
3. Approximately 5 % higher bending resistance of the friction connection is obtained in the circular tower compared to the polygonal tower, if shell imperfections are not considered. However, design imperfections in the polygonal tower are lower compared to imperfections of the circular tower. The same design bending resistance is obtained as for the circular tower.
4. There is no need to use slotted holes that are significantly longer than the group of bolts in the connection since the initial gap between the shells is closed by simultaneous deformations of the upper and lower shell. A small extension of the slotted hole beyond the last bolt in a row ($1d_0$ is used in this study) should be provided to allow easy alignment of the tower segments during execution.

ACKNOWLEDGEMENTS

The authors gratefully acknowledge the financial support by the European Research Fund of Coal & Steel, Grant-Agreements No. RFSR-CT-2010-00031 “High steel tubular towers for wind turbines (HISTWIN2)” as well as the Centrum for High-performance Steel (CHS) at Luleå University of Technology, Sweden and Portuguese Regional Operational Programme CENTRO2020 within the scope of the project CENTRO-01-0145-FEDER-000006.

REFERENCES

[1] Veljkovic, M., Heistermann, C., Husson, W., Limam, M., Feldmann, M., Naumes, J., Pak, D., Faber, T., Klose, M., Fruhner, K.U., Krutschinna, L., Baniotopoulos, C.C., Lavassas, I., Pontes, A., Ribeiro, E., Hadden, M., Sousa, R., Simões da Silva, L., Rebelo, C., Simões, R., Henriques, J., Matos, R., Nuutinen, J. and Kinnunen, H., “High-strength Tower in Steel for Wind Turbines (HISTWIN)”, Final Report - RFSR-CT-2006-00031, 2012, European Commission (RFCS).

[2] Veljkovic, M., Heistermann, C., Tran, A.T., Feldmann, M., Möller, F., Richter, C., Baniotopoulos, C.C., Gerasimidis, S., Zygomalas, I., Matos Silva, A., Simões da Silva L., Rebelo, C., Pinto, P., Matos, R., Moura, A., Gervasio, H., Siltanen, J., “High Steel Tubular Towers for Wind RTurbines (HISTWIN2)”, Final Report - RFSR-CT-2010-00031, 2015, European Commission (RFCS).

[3] Pavlovic, M., Heistermann, C., Veljkovic, M., Pak, D., Feldmann, M., Rebelo, C. and Simões da Silva, L., “Connections in Towers for Wind Converters – Part 2: The Friction Connection Behaviour”, Journal of Constructional Steel Research, 2015, Vol. 115, pp. 458-466.

[4] Pavlovic, M., Heistermann, C., Veljkovic, M., Pak, D., Feldmann, M., Rebelo, C., Simões da Silva, L., “Friction Connection vs. Ring Flange Connection in Steel Towers for Wind Converters”, Engineering Structures, 2015, Vol. 98, pp. 151-162.

[5] Heistermann, C., Veljkovic M., Simões R., Rebelo, C. and Simões da Silva, L., "Design of Slip Resistant Lap Joints with Long Open Slotted Holes", J. Constr. Steel Res. 2013, Vol. 82, pp. 223–233.
[6] Garzon, O., "Resistance of Polygonal Cross Sections - Application on Steel Towers for Wind Turbines", Licentiate Thesis, Luleå University of Technology, 2013.
[7] Reinke, T., "Tragverhalten von Stahlmasten mit polygonalem Querschnitt", DASt Kolloqium, Aachen, 2012.
[8] ABAQUS User Manual. Version 6.12. Providence, RI, USA: DS SIMULIA Corp; 2012.
[9] Pak, D. and Naumes, J., "High-strength Tower in Steel for Wind Turbines (HISTWIN): WP2.5 – Large Scale 4-Point-Bending Tests", Background Document - RFSR-CT-2006-00031, Brussels, Belgium: European Commission (RFCS), 2010.
[10] EN 1993-1-1, "Eurocode 3: Design of Steel Structures, Part 1-1: General Rules and Rules for Buildings", Brussels, Belgium: European Committee for Standardization (CEN), 2005.
[11] ECCS Publication No. 38, "European Recommendations for Bolted Connections in Structural Steelwork", Brussels, Belgium, ECCS, 1985.
[12] EN 1993-1-8: "Eurocode 3: Design of Steel Structures. Part 1-8: Design of Joints", Brussels, Belgium: European Committee for Standardization (CEN), 2005.
[133] Pavlovic, M., Heistermann, C., Veljkovic, M., Pak, D., Feldmann, M., Rebelo, C. and Simões da Silva, L., "Connections in Towers for Wind Converters – Part 1: Evaluation of Down-scaled Experiments", Journal of Constructional Steel Research, 2015, Vol. 115, pp. 445-457.
[14] ISO 898-1: "Mechanical Properties of Fasteners Made of Carbon Steel and Alloy Steel. Part 1: Bolts, Screws and Studs", Fourth Edition, Brussels, Belgium: European Committee for Standardization (CEN), 2009.
[145] Pavlović, M., Marković, Z., Veljković, M. and Buđevac, D., "Bolted Shear Connectors vs. Headed Studs Behaviour in Push-out Tests", J. Constr. Steel Res. 2013, Vol. 88, pp. 134-149.
[15] EN 1993-1-6: "Eurocode 3: Design of Steel Structures. Part 1-6: Strength and Stability of Shell Structures", European Committee for Standardization (CEN), 2007.
[16] Tran, A.T., Veljkovic, R., Rebelo, C. and Simões da Silva, L., "Resistance of Cold-formed High Strength Steel Circular and Polygonal Sections - Part 1: Experimental Investigations", Journal of Constructional Steel Research, 2016, Vol. 125, pp. 227-238.

DYNAMIC SOIL-STRUCTURE INTERACTION OF DUCTILE STEEL FRAMES IN SOFT SOILS

Edgar Tapia-Hernández[1,*], Yesenia De Jesús-Martínez[1] and Luciano Fernández Sola[1]

[1] *Materials Department, Universidad Autónoma Metropolitana – Azcapotzalco. Mexico City.*
**(Corresponding author: E-mail: etapiah@hotmail.com)*

Received: 7 June 2016; Revised: 27 August 2016; Accepted: 26 October 2016

ABSTRACT: Results of static and dynamic nonlinear analysis of ductile steel frames of 8- and 12- stories buildings are discussed in this paper. The influence of dynamic soil-structure interaction in deformation demands, failure mechanism, ductility and overstrength capacities and maximum demands in columns were analyzed. For this purpose, buildings were designed and studied under three boundary conditions: (i) fixed-base (no Soil-Structure Interaction), (ii) pile foundation and (iii) mat foundation condition. The influence of the lateral stiffness was studied through the response of moment resisting frames (unbraced frames), 1-braced bay frames and 2-braced bays frames. Soil foundation dynamic stiffness (impedance function) is introduced by a set of springs in horizontal and rocking direction, which were computed from the dynamic behavior and properties of the soil-foundation system. It was found that fixed base model might not be a conservative representation of the response of buildings with flexible foundations, especially when a pile foundation system is considered.

Keywords: Steel frames, inelastic analyses, pile foundation, mat foundation, soft soil

DOI: 10.18057/IJASC.2017.13.4.3

1. INTRODUCTION

Most of the design procedures in current seismic codes are based on elastic analyses and account the inelastic response in an indirect way. In many codes (such as Mexico's Federal District Code MFDC-04 [1] and ASCE/SEI 7-05 [2]), the lateral load patterns along the height of building depend on the fundamental period and their masses (Ganjavi and Hao [3]). In these codes, the load pattern is obtained by elastic analysis under a fixed-base condition, neglecting the possible effects of soil-foundation flexibility. The effectiveness of this procedure has been widely studied. In general, it is concluded that the ductility demands are not the same and in many cases the collapse mechanism is led by the first floor.

Results of nonlinear dynamic analysis suggest that models designed by following general guidelines do not adjust acceptably with the assumptions inherent to the design philosophy. Structures designed under a ductile behavior philosophy could have near-elastic responses and important overstrength reserves that are not necessarily considered in the design process (Tapia-Hernández and Tena-Colunga [4]). Therefore, the employment of the normative load patterns does not guarantee the optimum use of materials in regular buildings. An adjustment of the load pattern is necessary with respect to the period of the structure and the target ductility demand (Moghaddam and Hajirasouliha [5]).

In addition, seismic designs for soil-structure interaction (SSI) are based on an approximation in which the predominant period (and associated damping) of the corresponding fixed-base system are modified [1, 6, 7]. In fact, the current seismic provisions consider that the soil-structure interaction is a beneficial effect, since it usually causes a reduction of total base shear. However, in soft soil, the fundamental period of the building with fixed base might be located in the region of the ascending branch of the design spectra and, therefore, SSI might increase the acceleration demand, even despite the possible increase of the structure's damping.

In recent years, the influence of the SSI under inelastic analysis has been studied through single-degree-of-freedom systems (Rosenblueth and Reséndiz [8], Avilés and Pérez-Rocha [9]) or through simplified models in 2D (Tabatabaiefar *et al*. [10], Sáez *et al*. [11]); while the interaction on inelastic response of multi-degrees-of-freedom systems, which is more complex, has not been widely investigated (Ganjavi and Hao [12]). In fact, just a few studies of SSI on multi-degrees-of-freedom systems have been conducted (Barcena and Esteva [13], Raychowdhury [14], Fernández-Sola *et al*. [15]).

In this paper, the inelastic response of buildings structured with ductile steel frames was studied, in order to evaluate the influence of the foundation flexibility. Models represent typical regular mid-rise building frames in Mexico City. Buildings were evaluated through multi-degree-of-freedom systems under pushover and nonlinear time-history analysis. The dynamic analysis is performed by a set of selected historical ground motion related to the corresponding design spectrum. In addition, the influence of the lateral stiffness was also evaluated. For this purpose, the results of the analysis of moment resisting frames (unbraced frames), frames with one braced bay and frames with two braced frames are discussed.

2. DESCRIPTION OF MODELS

Buildings of 8- and 12- stories were designed for soft-soil site conditions (lake zone of Mexico City) and a ductility factor μ= 3.0, which is the maximum allowed for these structures according to MFDC-04 [1]. The buildings were representative of typical office buildings structured with ductile moment-resisting concentrically braced frames (MRCBFs) with three frame configurations: unbraced frames, internal frames with one braced bay and external frames with two braced bays as shown in Fig 1b. The design gravity loads for the studied models are also given in Figure 1.

Buildings were designed using 3-D models (Figure 1c) with the response spectrum analysis of MFDC-04 [1]. The resisting elements were designed by applying standard capacity concepts for ductile systems through an iterative process. Here, the following sequence was used for the member design: the bracing system, beams, columns and panel zone connection. The final sections for all models are summarized in Table 1 and reported in further detail in Tapia-Hernández [16].

According to MFDC-04 [1], a ductile braced frame should be designed using a representative analytical model, where a maximum shear strength balance between the resisting frames and the bracing system shall be considered. At all stories, the frames should be able to resist at least 50 percent of the seismic shear force without the contribution of bracing system. Moment resisting concentrically braced frames were designed to meet the lateral shear strength balances between the bracing system itself and the corresponding columns of the moment frame. Further information on the design process can be found in Tapia-Hernández and Tena-Colunga [17].

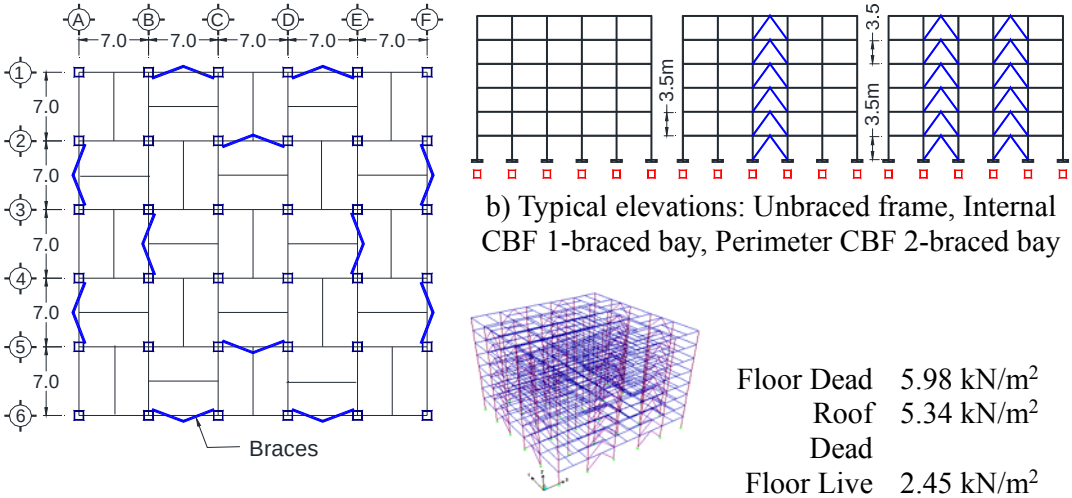

a) Typical floor plan view

b) Typical elevations: Unbraced frame, Internal CBF 1-braced bay, Perimeter CBF 2-braced bay

c) 3-D model

Figure 1. Buildings

Table 1. Designed Sections for the Studied Models

Model	Element	Stories	Cross section (cm)
8-story building	Column Rectangular box section	S1 to S3	40x40; *t*= 1.91 cm (3/4")
		S4 to S6	40x40; *t*= 1.58 cm (5/8")
		S7 to S8	40x40; *t*= 1.27 cm (1/2")
	Beams W-steel section	S1 to S2	W 18" x 128.1 kg/m
		S3 to S8	W 18" x112.9 kg/m
	Braces Rectangular box section	S1 to S4	15x15 *t*= 0.95 cm (3/8")
		S5 to S8	15x15 *t*= 0.64 cm (1/4")
12-story building	Column Rectangular box section	S1 to S3	45x45; *t*= 2.22 cm (7/8")
		S4 to S6	45x45; *t*= 1.90 cm (3/4")
		S7 to S8	45x45; *t*= 1.58 cm (5/8")
		S9 to S12	45x45; *t*= 1.27 cm (1/2")
	Beams W-steel section	S1 to S3	IR 18"x157.8 kg/m
		S4 to S12	IR 18"x144.3 kg/m
	Braces Rectangular box section	S1 to S4	25x25 *t*= 2.22 cm (7/8")
		S5 to S8	25x25 *t*= 1.91 cm (3/4")
		S9 to S12	25x25 *t*= 1.58 cm (5/8")

For the models with flexible base (SSI), two foundation systems were proposed: a partially compensated mat foundation and a pile foundation. Here, compensation corresponds to the difference between the total weight of the building and the resistance of the foundation slab behaving as a shallow foundation. Whereas floating circular piles (with diameter of 0.40 m) were considered for pile foundation. The particular design characteristics are discussed in the following section.

The frames of the building were decoupled in order to study the influence of the lateral stiffness on the inelastic response. The cryptograms for the identification of the models are *xyz*, where *x* indicates the base condition: *F* for a fixed-base boundary, *P* for a pile foundation and *M* for a mat foundation; *y* indicates the number of stories (08 or 12) and *z* indentifies the number of braced bays, 0 for unbraced frame, 1 for 1-bay braced frame and 2 for 2-bay braced frames (Figure 1b).

2.1 Characteristics of the Foundation

Soil properties were obtained from a downhole and suspension logging test of a typical cohesive soil (c= 50.0 kN/m^2) of the Lake Zone of Mexico City. Soil was modeled as a homogeneous layer with thickness H_s= 40 m, shear wave velocity V_s= 65 m/s, unit weight γ= 13 kN/m3, Poisson ratio ν= 0.50 and damping ratio ξ= 0.05. Thus, the foundation was designed following a resistance based design described in the MFDC-04 [1] for each flexible base system (Table 2). Further information about the characteristics of the soil and foundations can be found in Dávalos [18].

Table 2. Foundation Properties and Impedance Values

Building	Mat foundation			Piles			
	Depth (m)	K_h (kN/m)	K_r (kN/m)	No. of piles	Length (m)	K_h (kN/m)	K_r (kN/m)
8-story	4.0	$1.203(10)^6$	$8.931(10)^7$	121	20.0	$1.180(10)^6$	$7.330(10)^8$
12-story	9.0	$1.423(10)^6$	$2.792(10)^8$	169	22.0	$9.352(10)^5$	$3.330(10)^8$

Usually the dynamic behavior of the foundation is characterized by a complex-valued dynamic function commonly referred as the massless compliance function, which is defined as the ratio of the displacement response and the total load at the soil-foundation interface as a function of the frequency (Jafarzadeh and Asadinik [19]). The inverse of the compliance function is called impedance function and it is computed from the geometrical properties. Impedance functions (Eq. 1) are the dynamic stiffness of soil-foundation system. They are defined as the dynamic force (or moment) needed to produce a unitary displacement (or rotation) in the massless foundation.

$$\check{K}(\omega)=K(\omega) + i\omega C(\omega) \tag{1}$$

In Eq. 1, the real part $K(\omega)$ represents the inertia and stiffness of soil-foundation system. The imaginary part $C(\omega)$ represents the amount of energy dissipated by either wave radiation or histeretical behavior of the soil. Since the definition of the impedance functions considers that the soil-foundation system are performing together, the representation of soil-foundation stiffness and damping is done by a set of equivalent springs on the base of the building (Figure 2).

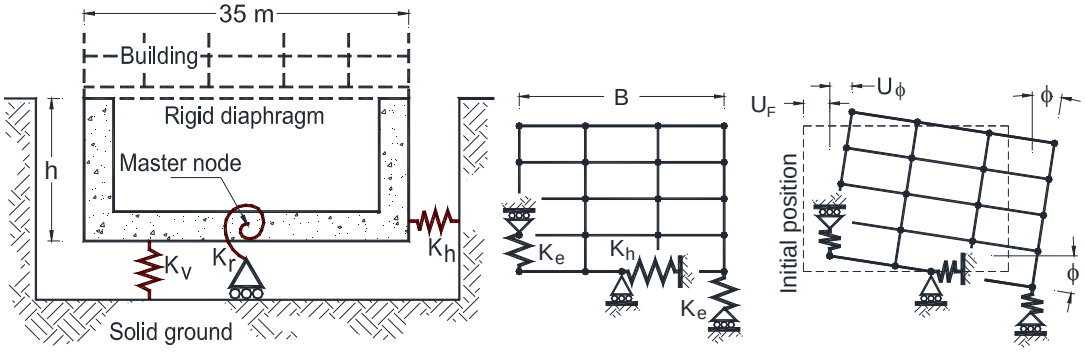

a) Impedance functions as a set of equivalent springs b) Boundary conditions and related displacements

Figure 2. Models with Flexible Foundation

Mexico City is placed on a thick layer of soft clay deposits over a hard stratum, located on the edge of an old lakebed. In the lake-bed area, the shear wave velocity of the soft clay varies from 40 to 90 m/s. Because of this, shear seismic waves experience an important vertical polarization, producing a mainly horizontal surface motion. Under these conditions, the rocking stiffness of the soil-foundation system and, specially, the horizontal stiffness have an important influence on the

structural behavior of flexible buildings. In contrast, the vertical response and, in consequence, the vertical stiffness is less important under lateral demands. This is characteristic not only for the local soil conditions of Mexico City, but also of all soft soils.

Thus, an infinite vertical stiffness was considered ($K_v \rightarrow \infty$); in fact, the vertical component of ground motion was neglected. Horizontal K_h and rocking K_r stiffness were computed with Dyna5 [20]. Mat foundation was modeled as *stratumfoundation* in Dyna5, which is a model of raft embedded in an homogeneous finite layer. Piles were modeled with *pile foundation* as flexible elements with pinned tip and a fixed head boundary condition; this model allows the study of group effects. The values obtained by the impedance functions for the fundamental frequency were also included in Table 2.

In the models, the rotational stiffness K_r was modeled by equivalent vertical springs K_e (Figure 3). The strategy to compute the stiffness of the equivalent spring K_e is through the sum of the moments about A (Eq. 2).

$$\Sigma M_A = 0 \qquad F_e(B/2) + F_e(B/2) - M_r = 0 \tag{2}$$

Where, B is the building's width (= 35 m, Figure 2a); F_e is the axial force of the equivalent spring, which is equal to $F_e = K_e d_e$ and M_r is the moment at the point A, which is equal to $M_r = K_r \phi$. Here, K_e is the stiffness of the equivalent spring; K_r is the rotational stiffness; ϕ is the base rotation and d_e is the axial shortening of the equivalent spring (Figure 3). Then, the equation of moment equilibrium becomes equal to Eq. 3.

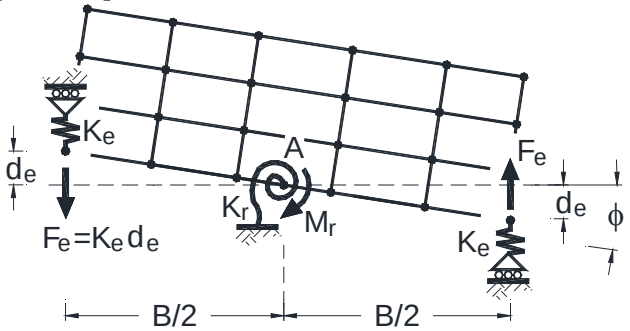

Figure 3. Definition of Variables

$$2[K_e d_e](B/2) - [K_r \phi] = 0 \tag{3}$$

Additionally, from trigonometry the rotation is equal to $\phi = d_e/(B/2)$, which is approximately true in the limit where the angle ϕ approaches to zero. The stiffness of the equivalent spring K_e can be computed by the Eq. 4, as a function of the rotational stiffness K_r.

$$K_e = K_r/(2(B/2)^2) \tag{4}$$

3. NONLINEAR STATIC ANALYSIS

Pushover analyses were carried out using the Drain-2DX computer program [21]. The elements were modeled with an inelastic response and P-delta effects were considered. An inverted triangular lateral load pattern was used, which is consistent with the static method of seismic analysis established in MFDC-04 [1].

Structural displacements of the fixed base model U_S are related exclusively with the deformations of the building. Moreover, models with flexible foundation are also related with two additional components: (*i*) the displacement associated with the foundation rocking U_ϕ and (*ii*) the base translation U_F, as shown in Figure 2b (Eq. 5).

$$U_T = U_S + U_F + U_\phi \quad (5)$$

Pushover curves by interstory of the 12-story building with 2-braced frames (F122, P122 and M122) are shown in Figure 4. According to the results, fixed-base frames are stiffer than the ones with flexible foundation. For this reason, a smaller lateral displacement was developed by the models without SSI. However, the large displacement of models with flexible-base (P122 and M122) should not be interpreted as the structures are subjected to a larger demand than the one computed for the fixed-base models. The lateral excitations are equivalent between them as it is discussed below.

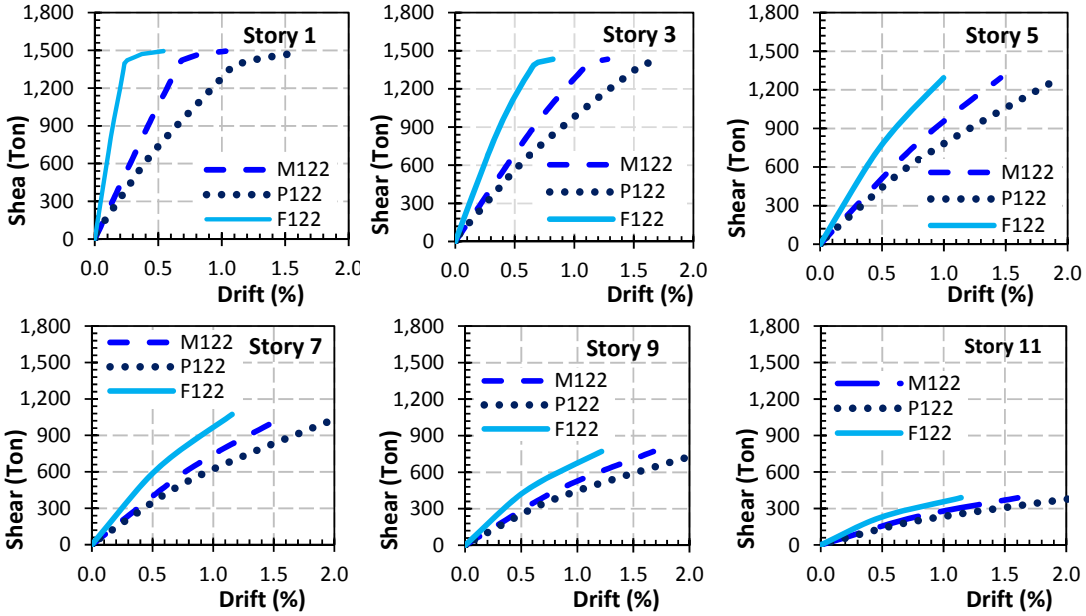

Figure 4. Capacity Curves of 2-bay Braced Frames of the 12-story Building

The global drift (deformation between the roof and base divided by the height) at initial yielding δ_y and the final drift δ_u related to the collapse mechanism were computed from pushover curves (Table 3). According to the results, the total displacements of flexible-foundation models ($U_S + U_F + U_\phi$) are significantly larger than the fixed-base ones. However, the demands are similar when only structure deformations are compared (the foundation rocking U_ϕ and base translation U_F components were removed).

Additionally, in order to identify the contribution of each displacement component (U_S, U_F and U) to the total displacements in the flexible-base models, the displacement normalized with the total displacement U_T was also computed (Table 3). It was found that the base translation component U_F has a small influence in the displacement, it represents between 6% and 10% of the total displacement U_T. In contrast, the foundation rocking component represents between 52% and 56% of the displacement originally obtained from the analysis U_T. This implies that the displacement component associated with the base rotation U_ϕ is the largest contribution in flexible base models. It is worth mentioning that the stiffer frame (2-braced bays) with pile foundation (P122C) does not follow this trend, but the main contribution is related to the structure deformation predominantly U_S.

Tabla 3.Global Drift obtained for the 12-story Buildings

Foundation model	Deformation	Model	Yielding			Collapse		
			δ_y (%)	Step	U/U_T(%)	δ_u (%)	Step	U/U_T(%)
a) Fixed-base model	Structure, U_S	F120	0.51	09	- - -	0.86	11	- - -
		F121	0.41	21	- - -	1.02	37	- - -
		F122	0.31	26	- - -	1.01	61	- - -
b) Flexible foundation model	Total, $U_T = U_S+U_F+U_\phi$ Results of pushover analyses	P120	0.95	09	100.0	1.46	11	100.0
		P121	0.78	21	100.0	1.70	37	100.0
		P122	0.50	22	100.0	1.90	60	100.0
		M120	0.92	09	100.0	1.41	11	100.0
		M121	0.75	21	100.0	1.65	37	100.0
		M122	0.56	26	100.0	1.62	61	100.0
	Structure and foundation rocking, $U_S + U_\phi$ (No base translation U_F)	P120	0.89	09	93.7	1.39	11	95.2
		P121	0.73	21	93.6	1.61	37	94.7
		P122	0.50	22	100.0	1.90	60	100.0
		M120	0.83	09	90.2	1.30	11	92.2
		M121	0.67	21	89.3	1.52	37	92.1
		M122	0.50	26	89.3	1.48	61	91.4
	Structure, U_S (No base translation U_F nor foundation rocking U_ϕ)	P120	0.52	09	54.7	0.93	11	63.7
		P121	0.41	21	52.6	1.05	37	61.8
		P122	0.45	22	90.0	1.77	60	93.2
		M120	0.52	09	56.5	0.92	11	65.2
		M121	0.41	21	54.7	1.05	37	63.6
		M122	0.31	26	55.4	1.02	61	63.0

Pushover global curves (base shear against global drift) of the studied models are shown in Figure 5. The unbraced frames and the 1-braced bay frames of the 12-stories building with flexible foundation (P120C, CC120C, P121C and CC121C) develop a similar response. However, the 2-braced bay frame with pile foundation (P122C) develops a larger displacement. This increase might be related to further damage of structural elements, because of the fact that the main displacement component is associated with the structure deformation (Table 3).

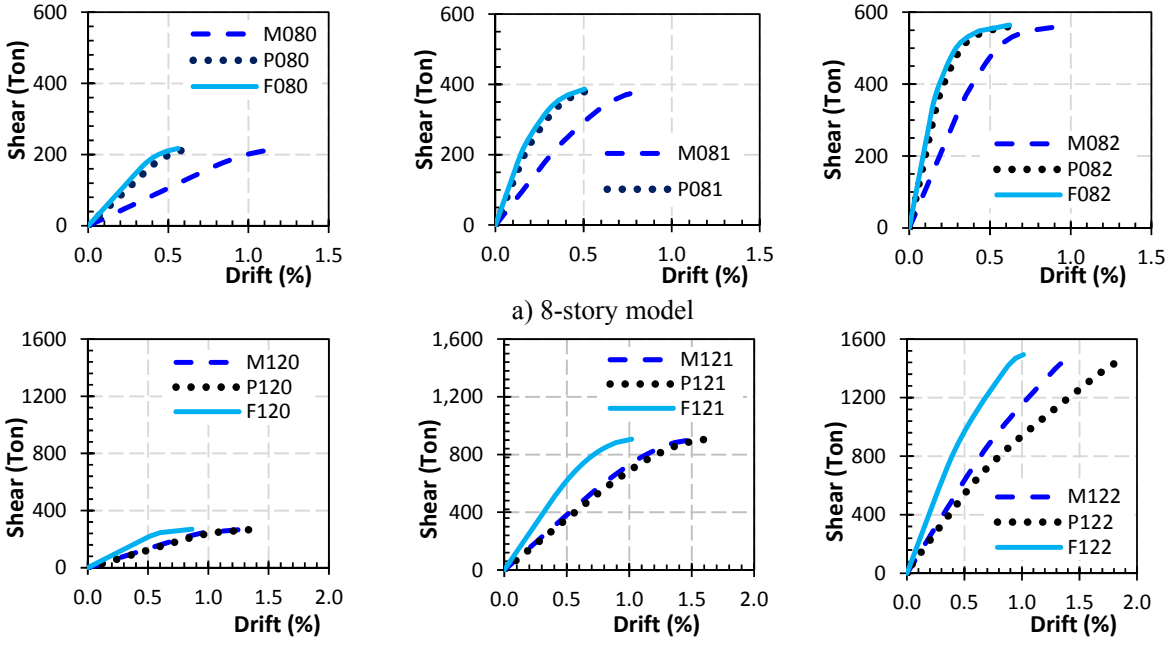

a) 8-story model

b) 12-story model

Figure 5. Pushover Global Curves

In contrast, the response of the 8-story frames with pile foundation (P080, P081 and P082) is similar to those developed by the fixed-base model (F080, F081 and F082). This is due to the group effect of the piles, which increases the stiffness of the soil-foundation system, in spite of the fact that the 8-story model has fewer piles than the 12-story model (Table 2).

In piles foundation, the stiffness of the group of piles is not necessarily equal to the sum of the individual stiffness of each element. In fact, due to the dynamic nature of the demand, the group effect might increase the stiffness of the foundation system (Dobry and Gazetas [22]). Thus, the increment of the stiffness is related primarily to dynamic nature of the impedance functions. If the analyzed frequency n corresponds to an anti-resonant frequency of the piles group; then the displacements would be reduced and, therefore, the group response would be stiffer.

The rocking stiffness of the pile foundation was computed in Dyna5 [20] for the studied buildings (Figure 6). There, the group effect was considered according to the method developed by Dobry and Gazetas [22].

For the quasi-static case ($n \approx 0.0$), the rocking stiffness is approximately $K_r = 6.1(10)^{11}$ kN/m in both cases (Figure 6), regardless the amount of piles. This is due to the quasi-static rocking stiffness depends only on the distance between the external piles. Thus, buildings might develop an equivalent response for frequencies less than $n < 7.0$ rad/sec. For higher frequencies, the dynamic interaction between individual piles becomes different due to the group effect. Rocking stiffness increases as the frequency increases for the 8-story building. And for the 12-story building, the interaction among wave fields produced by the individual piles decrease the stiffness. In Figure 6, the fundamental frequencies of the models ($n_{08} = 15.7$ rad/sec and $n_{12} = 12.6$ rad/sec) are included, in order to point out that the computed rotational stiffness for the 8-story building is almost twice as the one calculated for the 12-story building.

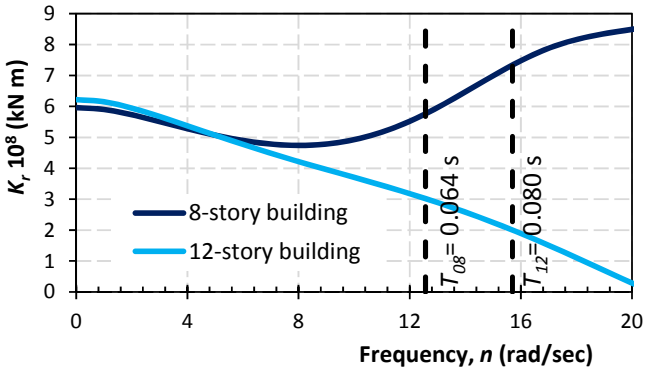

Figure 6. Rotational Stiffness K_r of the Pile Foundation Models

In fact, the group effect was also noticeable in the obtained pushover curves of the 8-story frames (Figure 7). Significant differences between the responses of the flexible base models were obtained. So, group effect might modify the overall stiffness of flexible base models. For some particular design conditions and models with piles foundation, flexible base models might become as stiffer as the fixed-base models. Additionally, it is worth mention that upper stories have near-elastic responses and important overstrength reserves, as it is discussed in the following section.

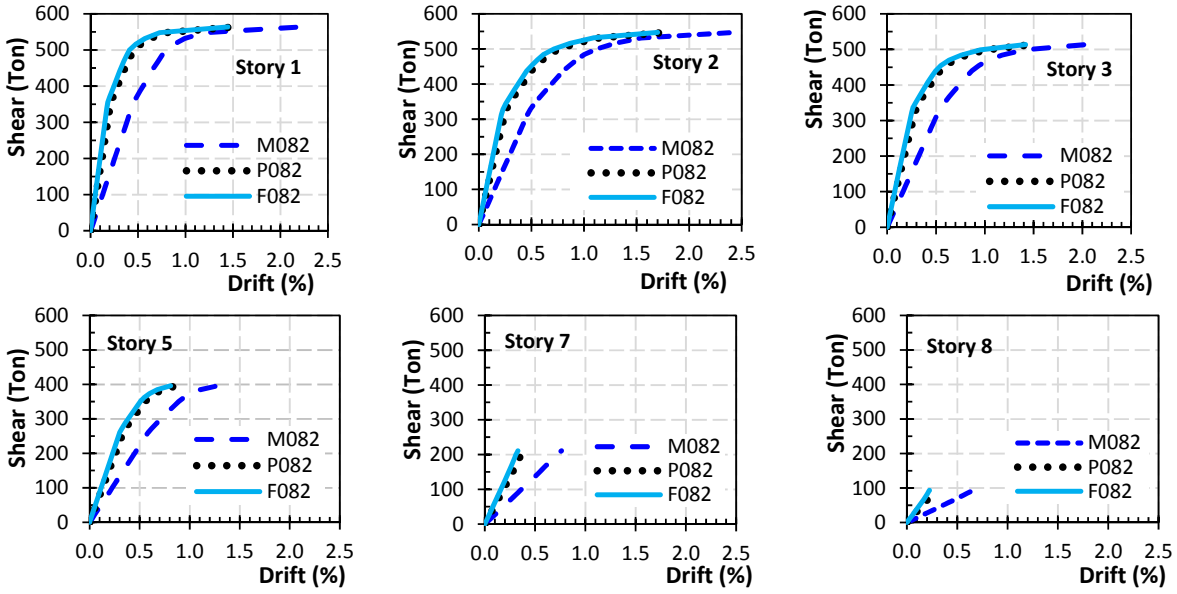

Figure 7. Pushover Curves of the 8-story Frame with 2-braced Bays

4. COLLAPSE MECHANISMS

Collapse mechanisms of the 2-braced bays frames (F122, P122 and M122) are presented in Figure 8. Magnitudes of inelastic deformations are shown with a color scale. They are normalized in relation with the maximum yielding rotation in beams and columns or axial extension and axial shortening in braces. In the braced bays, the brace in the left side is in tension with axial extensions, while the brace in the right side is in compression with axial shortenings. In each case, the step and the global drift were also included.

According to the results, besides the plastic hinges at beams, some plastic hinges have developed at column ends with fewer braces buckle at the collapse mechanism (Figure 8). This suggests a near soft story collapse mechanism with no uniform distribution of yielding within the height. The collapse mechanism is completely different from the one assumed in the design process (strong column - weak beam - weaker brace mechanism). In fact, results of recent research regarding braced frames (Tapia-Hernández and Tena-Colunga [4], Lacerte and Tremblay [23]) conclude that following current building codes, final collapse mechanism do not necessarily agree in many instances with the initial design assumptions in rational analyses of buildings. In addition, no dependency was observed between this trend and the modeled base condition.

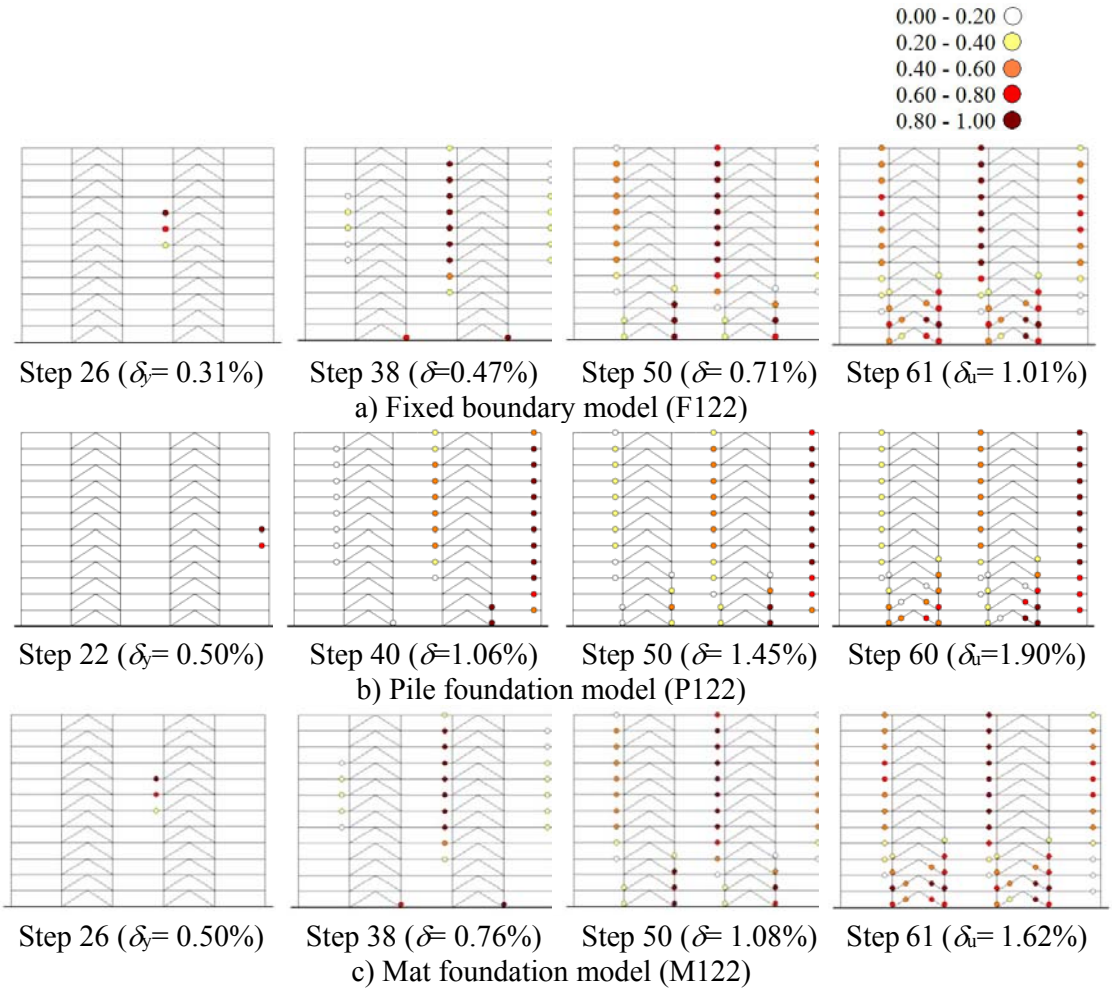

Figure 8. Behavior of 2-braced Bay Model along the Pushover Analysis

The deformation demands at the collapse mechanism were also studied. Average values of ultimate drifts are close to the Code's limit equal to 1.5% [1] for buildings structured with concentrically braced steel frames (Figure 9). Therefore, the normative deformation limit seems adequate for practical purposes as it was shown in similar studies (Tapia-Hernández and Tena-Colunga [24]). Considering this results, the developed ductility and overstrength for each frame are reported in the following section.

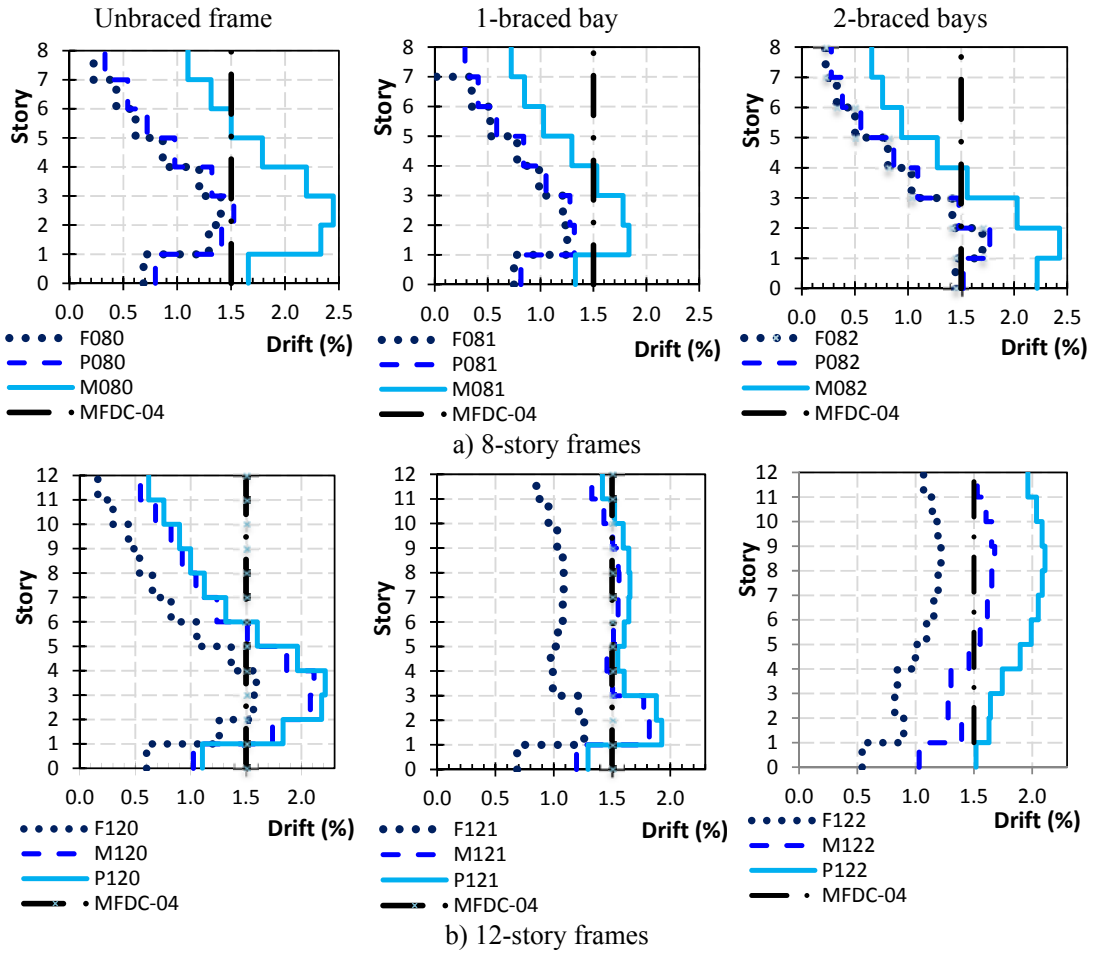

Figure 9. Deformation Demands at the Collapse Mechanism

5. DUCTILITY AND OVERSTRENGTH CAPACITIES

Ductility $\mu = \delta_u/\delta_y$ and overstrength capacities $\Omega = V_u/V_y$ were computed from pushover curves (Figure 4). The results for the 12-story frames are shown in Table 4.

The end of the elastic linear region are related with global drifts equal to 0.31% for the F122 and M122 models and 0.45% for the P122 model (Table 4, Figure 5b). Since the yielding drifts are related to the first non-linear step, the inelastic response appears sooner in fixed base and mat foundation than for the pile foundation system.

According to the results (Table 4), a dependency between the amount of braced bays (frame stiffness) and the ductility and overstrength capacities was noted. Stiffer frames (F122, P122 and M122) are related with the largest inelastic incursion. This trend does not depend on the base condition and might be simply due to the structural redundancy of each frame.

Table 4. Ductility and Overstrength Developed by the Studied Frames

Boundary condition	Model	Yielding drift δ_y (%)	Final drift δ_u (%)	Ductility μ	Shear at yielding V_y (kN)	Final shear V_u (kN)	Overstrength Ω
Fixed	F120	0.51	0.86	1.69	2,163	2,644	1.22
	F121	0.41	1.02	2.49	5,046	8,891	1.76
	F122	0.31	1.01	3.26	6,248	14,658	2.35
Flexible	P120	0.52	0.93	1.79	2,163	2,644	1.22
	P121	0.41	1.05	2.56	5,046	8,891	1.76
	P122	0.45	1.77	3.93	5,287	14,418	2.73
	M120	0.52	0.92	1.77	2,163	2,644	1.22
	M121	0.41	1.05	2.56	5,046	8,890	1.76
	M122	0.31	1.02	3.29	6,248	14,658	2.35

6. INCREMENTAL DYNAMIC ANALYSES

Incremental Dynamic Analysis (IDA) was performed on the 8- and 12-story frames to assess their performance against global collapse by instability. The IDA is a parametric analysis method that involves subjecting a structural model to ground motions that are scaled to multiple levels of intensity to produce curves of response parameters against intensity level (Vamvatsikos and Cornell [25]). The analysis was carried out for the motion recorded in Mexico City during the 1985 earthquake with magnitude 8.1 and peak amplitude of acceleration 0.17g (Figure 10). The selected historical ground motion corresponds to the design spectrum, according to the MFDC-04 for the lake bed zone (soft clay).

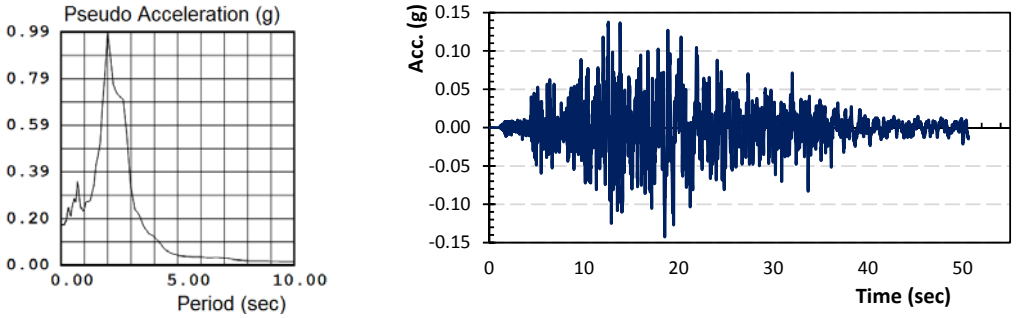

a) Response spectrum b) Acceleration time histories, component East-West

Figure 10. Motion Recorded in Mexico City during the 1985 Earthquake

The seismic behavior of the buildings was evaluated under IDA by examining the following response parameters:

a) Global drift (peak drift computed from the roof displacement U_T over the height of the structure H).
b) Peak interstory drift obtained along the nonlinear analysis (U_i/h).
c) The Drift Concentration Factor D_{CF}.

The peak global drift and the interstory drift angle allow the evaluation of the damage suffered for both the structural and non-structural elements. The drift concentration factor D_{CF} is useful to evaluate the capacity of the structure to mitigate the soft story mechanism and to analyze how the structure mobilizes the energy dissipation capacity (Izvernari *et al*. [26]). It is defined as the ratio between the maximum peak story drift angle along the building height U_i/h and the peak overall roof deformation angle U_T/H (Eq. 6).

$$D_{CF} = \frac{U_i/h}{U_T/H} \quad (6)$$

For steel frames, the value of D_{CF} depends on the continuity of the columns and on the flexural stiffness. If the columns are continuous and infinitely rigid, D_{CF} will be equal to unity. It means that all floors are equally deformed and story deformations are comparable to the average deformation of the building.

In the IDA procedure, a scaling factor was applied in order to increase the ground motion stepwise until collapse of the frame. The IDA curves (ground motion intensity against the maximum peak value) for 12-story frames with 1-braced bays (F121, P121 and M121) are shown in Figure 11. When drift values are compared (Figure 11a and 11b), frames with fixed base condition displayed a robust response; whereas, responses of models with SSI are similar between them. The model with a fixed base has a larger tendency to develop a soft story mechanism than the ones with flexible base (Figure 11c). In general, the response of F121 model (fixed base) envelops the response of flexible base models.

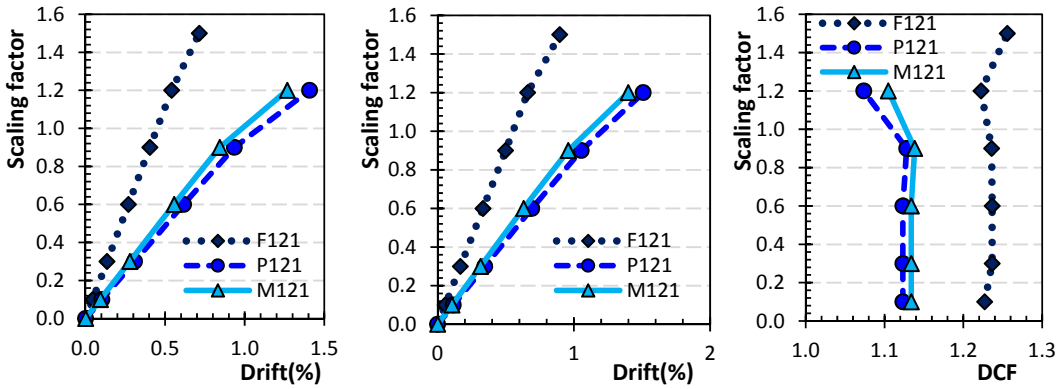

a) Global Drift b) Maximum peak interstory drift c) Drift concentration factor

Figure 11. Incremental Dynamic Analysis Curves for 1-braced Bays Frame

Moreover, IDA curves for 12-story frames with 2-braced bays (F122, P122 and M122) are shown in Figure 12. Here, the responses exhibit variations upon increasing ground motion amplitude up to dynamic instability by stepwise. The M122 curves generally exhibit a more stable response than the other models.

The F122 model (fixed base) does not completely envelop the response of the SSI models. This means that the fixed-base model might not be a conservative representation. In consequence, SSI might not be a beneficial effect on the seismic response of a structure, because of flexible base models develops a dynamic instability sooner than the one developed by the one with fixed-base, especially for the P122 model and a scaling factor equal to 1.5. Since this effect is developed only when the stiffer structures are compared, a relationship between the influence of the base flexibility and the lateral stiffness of the structure might be highlighted.

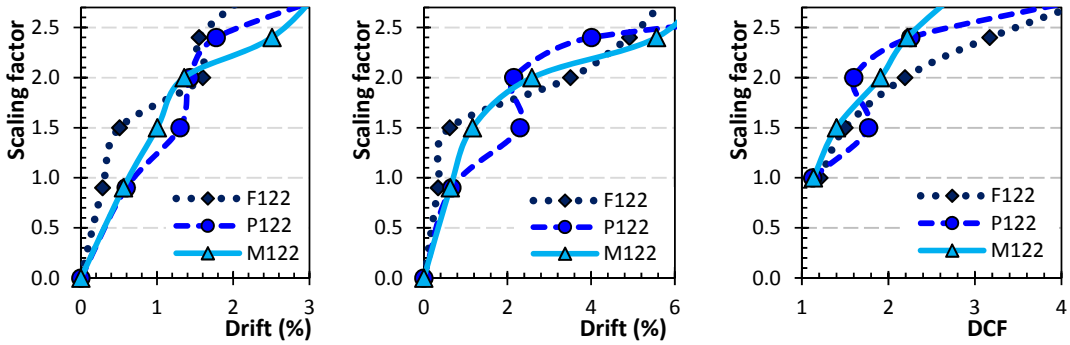

a) Global drift b) Maximum peak interstory drift c) Drift Concentration Factor

Figure 12. Incremental Dynamic Analysis Curves for 2-braced Bays Frame

6.1 Distribution of the Demands on the First Floor

Efforts to assess the influence of SSI effects on the redistribution and maximum demands in columns were developed. The maximum bending moment, shear and axial force in columns A-5 (braced bay) and A-6 (unbraced bay) at the first floor of 12-story frames are shown in Figure 13 and 14, respectively.

In column A-5 (Figure 13), peak demands of the bending moment and shear force of the flexible base models (M122 and P122) are enveloped by the demands of the fixed-base model (F122). This means that the rigid base analysis would be a conservative representation of the demands on the SSI models. However, the maximum axial load of P122 model exceeds the axial demands of the F122 model for a scaling factor equal to 1.5 (Figure 13c).

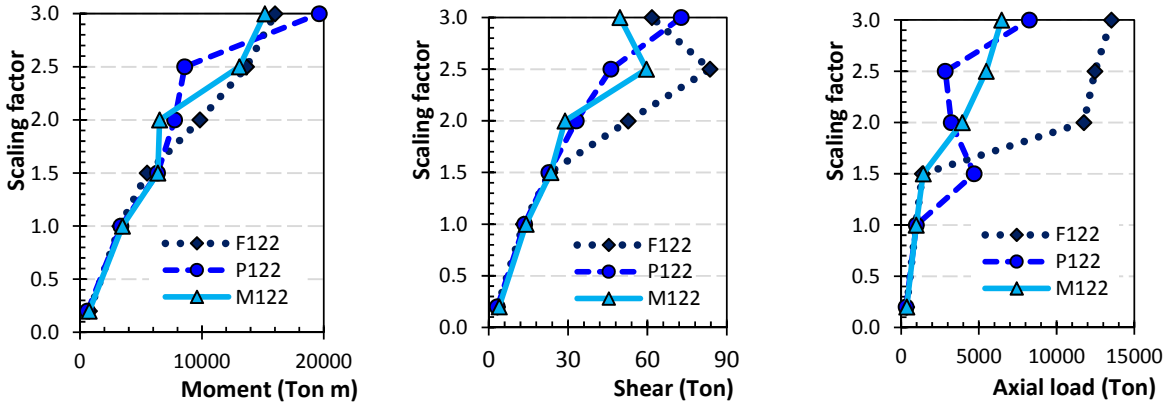

a) Bending moment b) Shear c) Axial force

Figure 13. Peak Demands under Incremental Dynamic Analysis of Column A-5 of 12-story Frames

Moreover, the same tendency was noted on demands of column A-6 (Figure 14). The F122 model (fixed base condition) is able to conservatively predict the magnitude of the peak demand of bending moment and shear force (Figure 13a and 13b). However, it is not a reliable representation of the axial load of the model with a piles foundation (P122, Figure 14c). Thus, the fixed-base model (F122) might estimate incorrectly the obtained axial loads when the SSI effect is accounted.

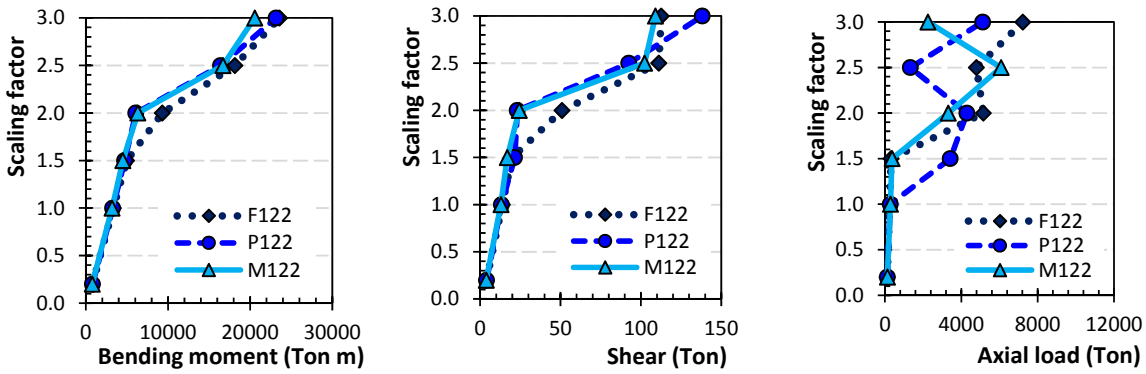

a) Bending moment b) Shear c) Axial load

Figure 14. Peak Demands under Incremental Dynamic Analysis of Column A-6 of 12-story Frames

7. CONCLUSIONS

In this paper, the inelastic responses of ductile steel frames of 8- and -12 regular buildings are evaluated. Models were analyzed under three boundary conditions: (i) fixed-base (no Soil-Structure Interaction), (ii) pile foundation and (iii) mat foundation. Buildings and foundations were designed according to the Mexico's Federal District Code with a ductility factor μ= 3.0 (the maximum allowed for these structures) and for soft-soil site condition (Lake zone).

Pushover analyses were carried out in order to evaluate the influence of the base flexibility on the ductility and overstrength capacities, displacements and collapse mechanisms. In addition, Incremental Dynamic Analyses were performed to assess the response based on the global drift, interstory drift, drift concentration factor and the peak demands in columns (bending moment, shear and axial load).

According to the results, the main contributions of the research are summarized as follow:

- In general, fixed-base models are stiffer than the flexible base models, when the deformation takes into account: a) the body deformations, b) the displacement associated with the foundation rocking and c) the base translation. However, in this study, it is reported that the group effect on piles might modify this trend for some particular conditions. In some cases, models with piles foundation were able to develop larger displacements than the ones with mat foundation. In others cases, models with piles became as stiff as the fixed-base models. So that, the stiffness of buildings with piles foundation is dependent not only of the base flexibility, but also of the specific design conditions, especially of the piles group effect.
- The displacement components of flexible base models (displacement U_F and rocking U_ϕ) represent about the 50 percent of the total displacement developed by the frames. Of them, the main contribution is related with the rocking effect U_ϕ. No dependency was reported between this observation and the foundation system or building's height. Similar body deformations were developed regardless the modeled foundation system.
- The lateral stiffness is strongly dependent of the group effect on piles. For this reason, despite of the fact that the superstructure is regular and it was designed following rational analysis, for the studied buildings, it is not recommended to neglect the soil-structure interaction effect, especially for buildings with pile foundation system.

- According to the results of incremental dynamic analysis, the axial load demands in the columns of the models with pile foundation exceed the ones developed by the fixed-base models for a range of the scaling factor. Fixed-base models might be an unconservative representation of the demands in flexible base models, despite of the fact that the peak demand of bending moment and shear force are acceptably enveloped by the response of the fixed-base model.
- For practical purposes, similar results were obtained in terms of collapse mechanisms and ductility and overstrength capacities, regardless the base foundation.

REFERENCES

[1] MFDC, Mexico's Federal District Code, Gaceta Oficial del Departamento del Distrito Federal. 2004, October (in Spanish).

[2] ASCE/SEI 7-05, Minimum Design Loads for Buildings and Other Structures, American Society of Civil Engineers, 2005.

[3] Ganjavi, B. and Hao, H., "A Parametric Study on the Evaluation of Ductility Demand Distribution in Multi-degree-of-freedom Systems Considering Soil-structure Interaction Effects", Engineering Structures, 2012, Vol. 43, pp. 88-104.

[4] Tapia-Hernández, E. and Tena-Colunga, A., "Code-Oriented Methodology for the Seismic Design for Regular Steel Moment Resisting Braced Frames", Earthquake Spectra Journal, 2014, Vol. 3, No. 4, pp. 1683-1709.

[5] Moghaddam, H. and Hajirasouliha, I., "Fundamentals of Optimum Performance-Based Design for Dynamic Excitations", Scientia Iranica, 2005, Vol. 12, No. 4, pp. 368-378.

[6] Aviles, J. and Perez-Rocha, L.E., "Use of Global Ductility for Design of Structure–foundation Systems", Soil Dynamic Earthquake Engineering, 2011, Vol. 31, No. 7, pp.1018–1026.

[7] Wolf, J.P., "Dynamic Soil-Structure Interaction", Prentice-Hall: New Jersey, 1985.

[8] Rosenblueth, E. and Reséndiz, D., "Disposiciones Reglamentarias de 1987 para tener en cuenta Interacción Dinámica Suelo-estructura", Research Report, 1988, No. 509, Universidad Nacional Autónoma de México (in Spanish).

[9] Avilés, J. and Pérez-Rocha, L.E., "Soil-structure Interaction in Yielding Systems", Earthquake Engineering and Structural Dynamics, 2005, No. 32, pp. 1749-1771.

[10] Tabatabaiefar, H.R., Samali, B. and Fatahi, B., "Effects of Dynamic Soil-Structure Interaction on Inelastic Behaviour of Mid-Rise Moment Resisting Buildings on Soft Soils", Proceedings of the Australian Earthquake Engineering Society Conference. Perth, Western Australia, 2010, pp. 1-11.

[11] Sáez, E., López-Cabellero, F. and Modaressi-Farahamand-Razavi, A., "Inelastic Dyanamic Soil-structure Interaction Effects on Moment-resisting Frame Buildings", Engineering Structures, 2013, Vol. 51, pp. 166-177.

[12] Ganjavi, B. and Hao, H., "Elastic and Inelastic Response of Single- and Multi-degree-of-freedom Systems Considering Soil Structure Interaction Effects", Proceeding of the Australian Earthquake Engineering Society Conference, Barossa Valley, South Australia, 2011, pp. 1-9.

[13] Barcena, A. and Esteva, L., "Influence of Dynamic Soil–structure Interaction on the Nonlinear Response and Seismic Reliability of Multistory Systems", Earthquake Engineering and Structural Dynamic, 2007, Vol. 36, No. 3, pp. 327–346.

[14] Raychowdhury, P., "Seismic Response of Low-rise Steel Moment Frame (SMRF) Buildings Incorporating Nonlinear Soil-structure Interaction (SSI)", Engineering Structures, 2011, Vol. 33, pp. 958-967.

[15] Fernandez-Sola, L.R., Dávalos-Chavez, D. and Tapia-Hernandez, E., "Influence of the Dynamic Soil Structure Interaction on the Inelastic Response of Steel Frames: Proceedings of the 10th National Conference in Earthquake Engineering, Anchorage, AK. 2014, pp. 1-11.

[16] Tapia-Hernández, E., "Comportamiento de Edificios Regulares Estructurados Con Marcos Dúctiles de Acero Con Contraventeo Concéntrico En Suelos Blandos", Ph.D. Thesis, 2011, Universidad Autónoma Metropolitana Azcapotzalco, available at http://posgradoscbi.azc.uam.mx/descargas/Tesis_ies_2011_TapiaHernandezEdgarUAM-A.pdf (in Spanish).

[17] Tapia-Hernández, E. and Tena-Colunga, A., "Lateral Demands of Steel Moment Resisting Concentrically Braced Frames in Soft Soils", Proceedings of the XV World Conference on Earthquake Engineering, Lisbon, Portugal, 2012, ID. 1614. pp. 1-10.

[18] Dávalos D., "Influencia de la interacción dinámica suelo estructura en el comportamiento estático no lineal de marcos de acero con y sin contravientos", Master Thesis, 2013, Universidad Autónoma Metropolitana Azcapotzalco, México (in Spanish).

[19] Jafarzadeh, F. and Asadinik, A., "Dynamic Response and Impedance Functions of Foundation Resting on Sandy Soil using Physical Model Tests", Proceedings of the XIV World Conference on Earthquake Engineering. Beijing, China, 2008, pp. 1-8.

[20] Novak, M., Sheta, M., El-Hifnawy, L., El-Marsafawi, H. and Ramadan, O., "DYNA5: A Computer Program for Calculation of Foundation Response to Dynamic Loads", Geotechnical Research Centre, 2005, The University of Western Ontario.

[21] Prakash, V., Powell, G.H. and Fillipou, F., "DRAIN-2DX: Base Program User Guide", Report No. UCB/SEMM-92/29, 1992, Department of Civil Engineering, University of California at Berkeley.

[22] Dobry, R. and Gazetas, G., "Simple Method for Dynamic Stiffness and Damping of Floating Pile Groups", Geotechnique, 1988, Vol. 38, No. 4, pp. 557-574.

[23] Lacerte, M. and Tremblay, R., "Making Use of Brace Overstrength to Improve the Seismic Response of Multistory Split-X Concentrically Braced Steel Frames", Canadian Journal of Civil Engineering, 2006, 33, pp. 1005-1021.

[24] Tapia-Hernández, E. and Tena-Colunga, A., "Diseño sísmico de marcos de acero contraventeados. Parte 1: Recomendaciones de Diseño", Revista de Ingeniería Sísmica, 2013, 88, pp. 43-68. dx.doi.org/10.18867/2013-RIS-88-3 (in Spanish).

[25] Vamvatsikos, R. and Cornell, A., "Incremental Dynamic Analysis", Earthquake Engineering and Structural Dynamics, 2002, Vol. 31, pp. 492-514.

[26] Izvernari, C., Lacerte, M. and Tremblay, R., "Seismic Performance of Multi-storey Concentrically Braced Steel Frames Designed According to the 2005 Canadian Seismic Provisions", Proceedings of the IX Canadian Conference on Earthquake Engineering, Ottawa, Canada. 2007, pp. 1-10.

STATIONARY AND TRANSIENT RESPONSES OF SUSPENSION BRIDGES TO SPATIALLY VARYING GROUND MOTIONS INCLUDING SITE RESPONSE EFFECT

Süleyman Adanur [1], Ahmet Can Altunışık [2,*], Kurtuluş Soyluk [3] and A. Aydın Dumanoğlu [4]

[1] *Assoc. Prof. Karadeniz Technical University, Department of Civil Engineering, Trabzon, Turkey*
[2] *Karadeniz Technical University, Department of Civil Engineering, Trabzon, Turkey*
3 Gazi University, Department of Civil Engineering, Ankara, Turkey
4 Canik Başarı University, Department of Civil Engineering, Samsun, Turkey

**(Corresponding author: E-mail: ahmetcan8284@hotmail.com)*

Received: 21 April 2016; Revised: 3 May 2016; Accepted: 12 May 2016

ABSTRACT: This paper presents an investigation about the stationary and transient analyses of suspension bridges subjected to spatially varying ground motions including the site response effect. The Bosphorus Suspension Bridge, which connects Europe to Asia in Istanbul, Turkey is selected as a numerical example. The spatial variability of ground motions between the support points is taken into consideration with the coherency function, which arises from three sources: incoherence, wave-passage and site-response effects. The Heaviside Modulating Function has been used throughout the study for computing the transient responses. At the end of the study, the results are compared with each other in two groups as homogeneous-heterogeneous and stationary-transient responses. It is observed that the response values obtained for the heterogeneous soil condition cause larger response values than those of the homogeneous soil condition. Also the greater the differences between the soil conditions, the greater the response values. It is also noticed that the stationary response values are larger than those of the transient responses. Based on the obtained results, the stationary assumption can be accepted as satisfactory for the considered ground motion duration.

Keywords: Bosphorus suspension bridge; Incoherence effect; Site-response effect; Spatially varying ground motions; Stationary response; Transient response; Wave-passage effect.

DOI: 10.18057/IJASC.2017.13.4.4

1. INTRODUCTION

In long span engineering structures such as suspension bridges, earthquake motions will not be the same over distances due to the complex nature of the earth crust. It is evident that, because of the difference in local soil conditions at the supports, loss of coherency due to reflections and refractions, and travelling with finite velocity between support points, earthquake motions will be subjected to significant variations at the support points of the bridge. This variation will cause internal forces due to the pseudo-static displacements which do not arise under uniform ground motions. So, when analysing suspension bridges, the spatial variability of the earthquake motions should be considered. The spatially varying ground motion can be considered as multiple-support excitation for long span multi-support structural systems.

The earthquake response analysis of long span bridges subjected to spatially varying ground motions has aroused particular interest over the last four decades. The effects of multiple-support seismic excitations on suspension bridges were investigated by Abdel-Ghaffar and Rubin [1,2], who concluded that uncorrelated ground motions overestimate the responses compared to those of the uniform ground motion case. The responses of simplified bridge models such as continuous

beams, reinforced concrete bridges, and incompressible circular arches to spatially varying ground motions were investigated by Harichandran and Wang [3], Bilici et al. [4], Zhang et al. [5], Zembaty [6], Gao et al. [7], Li and Chouw [8] and the significance of spatially varying ground motions was observed. Simplified bridge models and a suspension bridge model subjected to the spatially varying earthquake motions were studied, by Der Kiureghian and Neuenhofer [9], Nakamura et al. [10], Der Kiureghian et al. [11] based on a newly developed multiple support response spectrum method. They concluded that the developed response spectrum method offers a simple and viable alternative for seismic analysis of multiple supported structures subjected to spatially varying ground motions. The response of a long span suspension bridge to spatially varying ground motion due to topographic effects was analysed by Rassem et al. [12] who concluded that soil conditions, site topography and bridge support locations in a valley are important-factors which demand a more thorough evaluation of the ground motions exciting the bridge. Stochastic response analyses of cable-stayed bridges subjected to spatially varying ground motions were carried out by Allam and Datta [13,14], Soyluk and Sıcacık [15], Ateş et al. [16], and Zhang et al. [17] which underlined the significance of the spatial variability of ground motions between the support points.

In random vibration analysis, statistical averages are assumed to be independent of time for stationary excitation. In fact, earthquake motions cannot be stationary, because they initially grow from zero, then have a steady phase and eventually decay. Therefore, earthquake motions should be taken as nonstationary excitations. Although earthquake excitation cannot be stationary throughout the motion, it can be taken as stationary for the time period where maximum structural responses occur.

Stationary and transient response analyses of long span bridges subjected to spatially varying ground motions have been carried out frequently in recent years. Stationary and nonstationary stochastic response analyses of suspension, deck arch and cable-stayed bridges subjected to spatially varying ground motions for homogeneous soil conditions were performed by Hawwari [18], Harichandran et al. [19], Adanur et al. [20], Jia et al. [21], and Soyluk and Dumanoglu [22]. In all of these studies the significance of the spatially varying ground motion was underlined. The nonstationary response of a viaduct subjected to spatially varying ground motions was investigated by Perotti [23] and concluded that the incoherence effect is more important than the wave-passage effect. Hyun et al. [24] developed a new method for the nonstationary response analysis of suspension bridges. Numerical results of this study indicated that correlation effects at different support points have significant effects on the dynamic responses of suspension bridges.

The objective of this paper is to determine the stationary and transient responses of suspension bridges, which have not been analysed comprehensively for spatially varying ground motions including the incoherence, wave-passage and site-response effects together. For this purpose the stationary and transient responses of suspension bridges subjected to spatially varying ground motions are investigated, taking into consideration the site-response, incoherence and wave-passage effects at the same time. The relative contributions of the pseudo-static, dynamic and covariance components to the total response are also presented.

2. RANDOM VIBRATION THEORY FOR SPATIALLY VARYING GROUND MOTION

2.1 Stationary Response

One of the effective methods used to carry out random vibration analysis of structural systems is to use the stationary random process theory. This theory has been used widely in the random vibration analysis of structures. The stationary random process theory provides a reasonable basis for the seismic analysis of multiply supported structures where the spatial variability of the ground motion is comprehensively taken into account and hence used consistently by many researchers for the random vibration analysis of structures under the spatially varying ground motions (Der Kiureghian [25]).

In the random vibration theory, the variance of the ith total response component is expressed as [19]

$$\sigma_{z_i}^2 = \sigma^2{}_{z_i}^{qs} + \sigma^2{}_{z_i}^{d} + 2Cov(z_i^{qs}, z_i^{d}) \tag{1}$$

where, $\sigma^2{}_{z_i}^{qs}$ is the variance of the pseudo-static response component, $\sigma^2{}_{z_i}^{d}$ is the variance of the dynamic response component and $Cov(z_i^{qs}, z_i^{d})$ is the covariance between the pseudo-static and dynamic components and can be written as

$$\sigma^2{}_{z_i}^{qs} = \sum_{l=1}^{r}\sum_{m=1}^{r} A_{il}A_{im}\int_{-\infty}^{\infty}\frac{1}{\omega^4}S_{\ddot{v}_{g_l}\ddot{v}_{g_m}}(\omega)d\omega \tag{2}$$

$$\sigma^2{}_{z_i}^{d} = \sum_{j=1}^{n}\sum_{k=1}^{n}\sum_{l=1}^{r}\sum_{m=1}^{r}\psi_{ij}\psi_{ik}\Gamma_{lj}\Gamma_{mk}\int_{-\infty}^{\infty}H_j(-\omega)H_k(\omega)S_{\ddot{v}_{g_l}\ddot{v}_{g_m}}(\omega)d\omega \tag{3}$$

$$Cov(z_i^{qs}, z_i^{d}) = -\sum_{j=1}^{n}\sum_{l=1}^{r}\sum_{m=1}^{r}\psi_{ij}A_{il}\Gamma_{mj}\int_{-\infty}^{\infty}\frac{1}{\omega^2}H_j(\omega)S_{\ddot{v}_{g_l}\ddot{v}_{g_m}}(\omega)d\omega \tag{4}$$

where ω is the circular frequency, r is the number of support degrees of freedom where the ground motion is applied, n is the number of modes used in the analysis, A_{il} and A_{im} are the static displacement components due to unit support motions, $S_{\ddot{v}_{g_l}\ddot{v}_{g_m}}(\omega)$ is the cross spectral density function of accelerations between supports l and m, Γ is the modal participation factor, ψ is the eigenvectors and $H(\omega)$ is the frequency response function. The frequency response function is defined as

$$H_k = \frac{1}{\omega_k^2 - \omega^2 + 2i\xi_k\omega_k\omega} \tag{5}$$

where ω_k is the modal circular frequency and ξ_k is the modal damping ratio.

2.2 Transient Response

It is well known that it is rather complicated and tedious to get closed-from expressions for the modal frequency response function to model the non-stationarity of the ground accelerations. Because the main objective of this study is to determine the stationary and transient responses of suspension bridges qualitatively, the Heaviside Modulating Function is used for the modal

frequency response function to determine the transient structural responses (Harichandran et al. [19]).

For the present study, the Heaviside Modulating Function is used to take into account the effect of transient responses. The Heaviside Modulating Function is defined as [19]

$$H_k(\omega,t) = H_k(\omega)\left\{1-\exp(-\xi_k\omega_k t)\exp(-i\omega t)\left[\cos\omega_{kd}t + \frac{(\xi_k\omega_k + i\omega)}{\omega_{kd}}\sin\omega_{kd}t\right]\right\} \tag{6}$$

where $\omega_{kd} = \omega_k\sqrt{1-\xi_k^2}$. The transient responses at given times are computed by replacing the normal frequency response function with the function $H_k(\omega,t)$ in the expressions written for the stationary response.

2.3 Mean of Maximum Value

Depending on the peak response and standard deviation of the total response, the mean of maximum value (μ), in the stochastic analysis can be written as

$$\mu = p\sigma_z \tag{7}$$

where *p* is a peak factor and σ_z is the standard deviation of the total response [9].

3. SPATIALLY VARYING GROUND MOTION MODEL

The spatial variability of ground motion is characterised by the coherency function in the frequency domain. This function is dimensionless and complex valued. For the coherency function, the following model proposed by Der Kiureghian [25] is used

$$\gamma_{lm}(\omega) = \gamma_{lm}(\omega)^i\gamma_{lm}(\omega)^w\gamma_{lm}(\omega)^s = \gamma_{lm}(\omega)^i\exp\left[i\left(\theta_{lm}(\omega)^w + \theta_{lm}(\omega)^s\right)\right] \tag{8}$$

where $\gamma_{lm}(\omega)^i$ characterises the real valued incoherence effect, $\gamma_{lm}(\omega)^w$ indicates the complex valued wave-passage effect and $\gamma_{lm}(\omega)^s$ defines the complex valued site-response effect.

For the incoherence effect, resulting from reflections and refractions of seismic waves through the soil during their propagation, the widely used model proposed by Harichandran and Vanmarcke [26] is considered. This model is based on the analysis of recordings made by the SMART-1 seismograph array in Lotung, Taiwan and defined as

$$\gamma_{lm}(\omega)^i = A\exp\left[-\frac{2d_{lm}}{\alpha\theta(\omega)}(1-A+\alpha A)\right] + (1-A)\exp\left[-\frac{2d_{lm}}{\theta(\omega)}(1-A+\alpha A)\right] \tag{9}$$

$$\theta(\omega) = k\left[1+\left(\frac{\omega}{2\pi f_0}\right)^b\right]^{-\frac{1}{2}} \tag{10}$$

where d_{lm} is the distance between support points *l* and *m*. A, α, k, f_0 and b are model parameters and

in this study the values obtained by Harichandran et al. [19] are used (A=0.636, α=0.0186, k=31200, f_0=1.51 Hz and b=2.95).

The wave-passage effect resulting from the difference in the arrival times of waves at support points is defined as [25]

$$\theta_{lm}(\omega)^w = -\frac{\omega d_{lm}^L}{v_{app}} \tag{11}$$

where v_{app} is the apparent wave velocity and d_{lm}^L is the projection of d_{lm} on the ground surface along the direction of propagation of the seismic waves. The apparent wave velocities employed in this study are v_{app}=400 m/s for soft soil, v_{app}=700 m/s for medium soil and v_{app}=1000 m/s for firm soil.

The site-response effect resulting from the differences in local soil conditions at the support points is defined as [25]

$$\theta_{lm}(\omega)^s = tan^{-1}\frac{Im\left[H_l(\omega)H_m(-\omega)\right]}{Re\left[H_l(\omega)H_m(-\omega)\right]} \tag{12}$$

where $H_l(w)$ is the local soil frequency response function representing the filtration through soil layers.

The power spectral density function of the ground acceleration $\left(\ddot{v}_{g_l}\right)$ characterising the earthquake process is assumed to be of the following form modified by Clough and Penzien [27].

$$S_{\ddot{v}_{gl}\ddot{v}_{gl}}(\omega) = S_0\left[\frac{\omega_l^4 + 4\xi_l^2\omega_l^2\omega^2}{(\omega_l^2-\omega^2)^2 + 4\xi_l^2\omega_l^2\omega^2}\right]\left[\frac{\omega^4}{(\omega_f^2-\omega^2)^2 + 4\xi_f^2\omega_f^2\omega^2}\right] \tag{13}$$

where S_0 is the amplitude of the white-noise bedrock acceleration, and ω_l, ξ_l and ω_f, ξ_f are the resonant frequency and damping ratio of the first and second filters, respectively.

In this study, firm (F), medium (M) and soft (S) soil types are used. The filter parameters for these soil types proposed by Der Kiureghian and Neuenhofer [9] are utilized as presented in Table 1. The amplitude of the white-noise bedrock acceleration (S0) is obtained for each soil type by equating the variance of the ground acceleration to the variance of the S16E component of the Pacoima Dam acceleration records of the 1971 San Fernando earthquake. The calculated values of the intensity parameter for each soil type are S0(firm)=0.009715 m2/s3, S0(medium)=0.014436 m2/s3, and S0(soft)=0.020267 m2/s3. Acceleration power spectral density function for each soil type is presented in Figure 1.

Table 1. Power Spectral Density Parameters for Model Soil Types

Soil Type	ω_l (rad/s)	ξ_g	ω_f (rad/s)	ξ_f
Firm	15.0	0.6	1.5	0.6
Medium	10.0	0.4	1.0	0.6
Soft	5.0	0.2	0.5	0.6

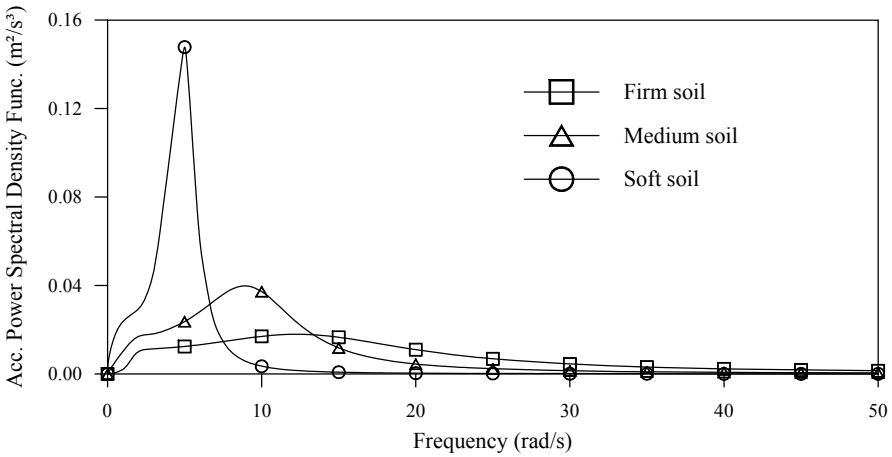

Figure 1. Acceleration Power Spectral Density Functions for the Filtered White Noise Model for Different Soil

4. NUMERICAL EXAMPLE

In this study, the Bosphorus Suspension Bridge in Turkey which connects Europe to Asia in Istanbul is selected as a numerical example (Figure 2). The construction of the bridge started in 1970 and was completed in 1973.

Figure 2. Bosphorus Suspension Bridge

The bridge has steel towers which are flexible, inclined hangers and a steel box-deck of 1074 m main span with side spans of 231 and 255 m on the European and Asian sides, respectively. The horizontal distance between the cables is 28m and the roadway is 21m wide, accommodating three lanes each way. The roadway at the mid-span of the bridge is approximately 64m above the sea level. A schematic representation of the Bosphorus Suspension Bridge including the dimensions is given in Figure 3.

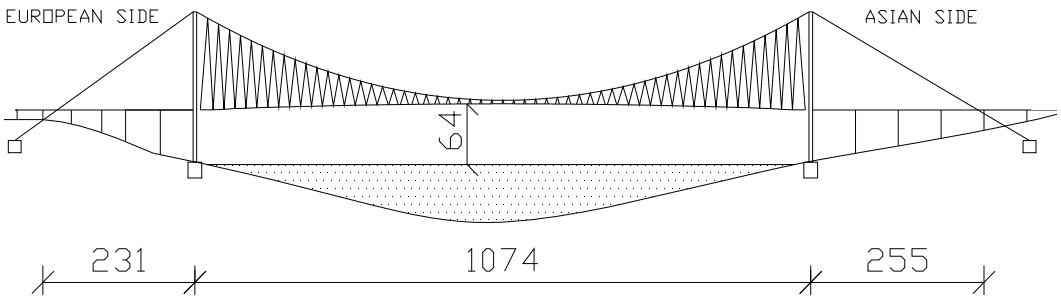

Figure 3. Schematic Representation of the Bosphorus Bridge Including the Dimensions (Dimensions as m)

The deck was constituted with particular concern for aerodynamic form in order to reduce the wind effect along the bridge deck. The aerodynamic steel box-girder deck of the bridge consists of 60 box-girder deck pieces, each comprising 3m deep prefabricated sections of 17.9m long x 33m. The top of each box section consists of an orthotropic plate on which a 35 mm thick mastic asphalt surface is laid.

The bridge has 165m high slender steel towers. The tower legs are 5.20x7.00m at the bottom and they taper to 3.00x7.00m at the top. Vertical tower legs are connected by three horizontal portal beams. Dimensions of the bridge towers are given in Figure 4.

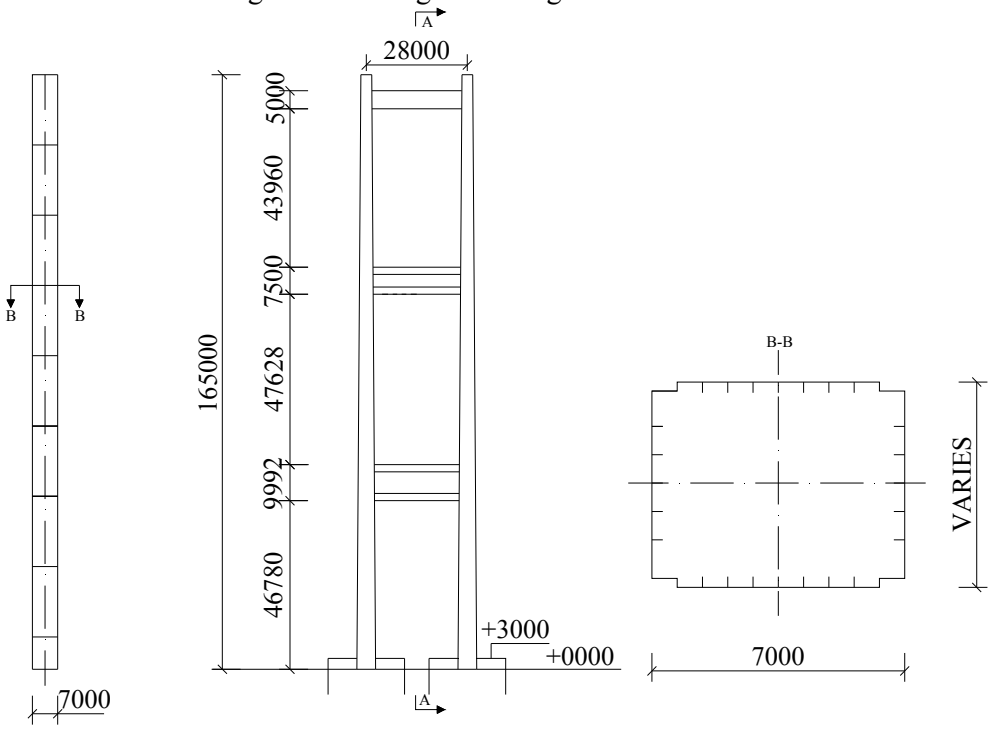

Figure 4. Dimensions of the Bridge Towers (Dimensions as mm)

The main cables of the bridge are built up from parallel wire, 5mm in diameter over the hot dipped galvanizing. Each main cable consists of 19 strands extending between the towers and contains 548 parallel wires, with a further four strands, each containing 192 wires for the backstays.

4.1 Mathematical Model of the Bridge

To investigate the stochastic response of the Bosphorus Suspension Bridge, a two-dimensional

mathematical model of the bridge with 202 nodes, 159 beam elements, 118 truss elements, and 475 degrees of freedom is used in the analyses (Figure 5). The deck, towers, and cables of the selected bridge are modelled using beam elements and the hangers are modelled by truss elements. The analyses are obtained for a 2.5% damping ratio and for the first 15 modes. The stiffening effects of the cables caused by dead load are also accounted for in the analyses.

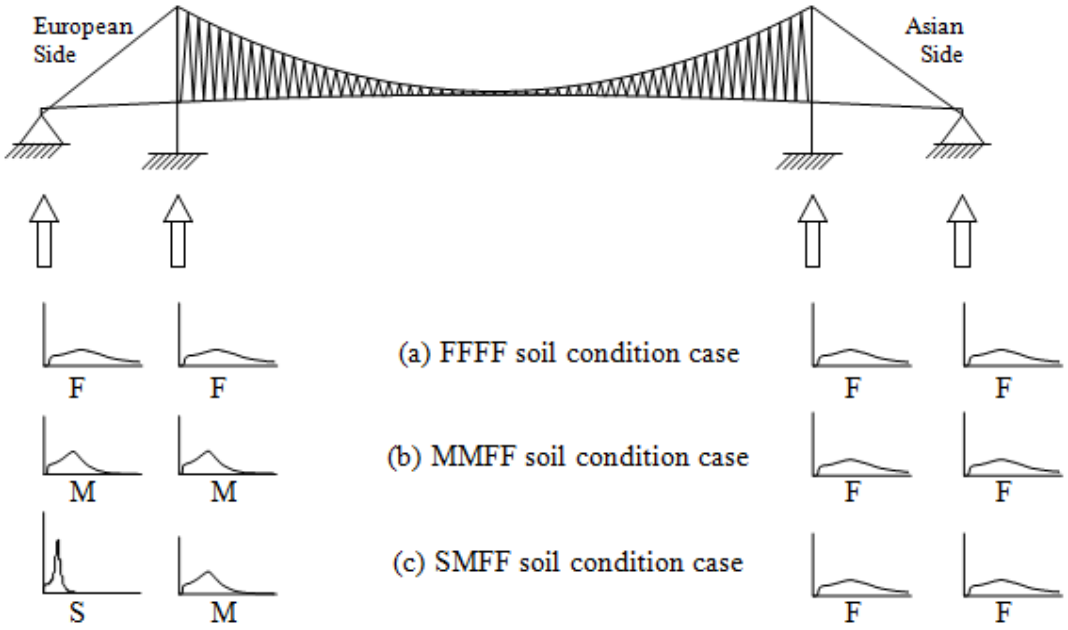

Figure 5. Suspension Bridge Subjected to Spatially Varying Ground Motions in the Vertical Direction for Homogeneous and Heterogeneous Soil Conditions.

4.2. Numerical computations

Stationary and transient analyses of a suspension bridge subjected to spatially varying ground motions are carried out taking into account the incoherence, wave-passage and site-response effects. For this purpose the following three different soil condition cases are considered. Each letter corresponds to a particular support and the soil conditions at that support point.

Case A: All the supports are assumed to be founded on soils with firm soil type (FFFF). This case corresponds to the homogeneous soil type.

Case B: While the supports at the European side are assumed to be founded on medium soil, the supports at the Asian side are assumed to be founded on firm soil type (MMFF).

Case C: The European side anchorage is founded on soft soil, the European side tower pier is founded on medium soil and the supports of the bridge at the Asian side are founded on firm soil (SMFF).

The filtered white noise ground motion model modified by Clough and Penzien [27] is used. It is applied in the vertical direction as a ground motion model in which the spectral density function intensity parameter is determined according to the S16E component of the Pacoima dam record of the San Fernando earthquake in 1971.

The suspension bridge subjected to spatially varying ground motion in the vertical direction for homogeneous and heterogeneous soil cases is shown in Figure 5. The vertical input is assumed to travel across the bridge from the European side to the Asian side with finite velocity of 400 m/s for soft soil, 700 m/s for medium soil and 1000 m/s for firm soil. The spectral density function applied

to each support point as a ground motion is different for each soil type. The general excitation case, which includes the three spatial variability effects, namely the incoherence, wave-passage and site-response effects, is considered in this study.

To determine whether the bridge will reach its stationary response during various durations of the strong shaking; the variances of the transient responses are calculated at 10, 20, 30 and 40 seconds and compared with the stationary responses for the spatially varying ground motions.

5. NUMERICAL RESULTS

5.1 Comparison of Homogeneous and Heterogeneous Responses

The mean of maximum values of total responses is carried out for the considered soil condition sets under the general excitation case which includes the most important effects of spatially varying ground motions. The mean of maximum total vertical deck displacements, bending moments and shear forces calculated for different soil condition sets, defined as FFFF, MMFF and SMFF, are compared in Figure 6. As can be observed from these figures, the stationary response values obtained for the FFFF (homogeneous) soil condition set are the lowest, and the response values for SMFF soil condition set are the highest. The total displacements and bending moments at the middle of the deck obtained from the general excitation case overestimates the responses by 68.39%, 98.41% and by 39.64%, 51.46% for the MMFF, and SMFF soil condition cases, respectively, when compared with the responses due to the FFFF (homogeneous) soil condition case. At the deck point where maximum shear forces take place it is found that the total shear forces obtained from the general excitation case overestimate the response by 52.94%, and 67.48% for the MMFF, and SMFF soil condition cases, respectively, when compared with the response due to the FFFF soil condition case. While the total vertical displacements obtained at the end of deck on the Asian side are close to each other for the three different soil condition sets, the displacements obtained at the end of deck on the European side for the MMFF and SMFF soil condition sets are larger than those of the FFFF soil condition case. This is due to the change in the soil conditions at the European side from firm to soft.

The mean of the maximum total horizontal displacements, bending moments and shear forces at the European and Asian side towers obtained for the three different soil condition sets under the general excitation case are presented in Figure 7. It is evident that the response values obtained at the tower on the Asian side are very much smaller than the response values calculated at the tower on the European side where the soil conditions change from firm to soft. It is also indicated that the response values obtained for the SMFF soil condition case are generally the highest. Moreover, the greater the difference between the soil conditions, generally the greater the response values found at both towers.

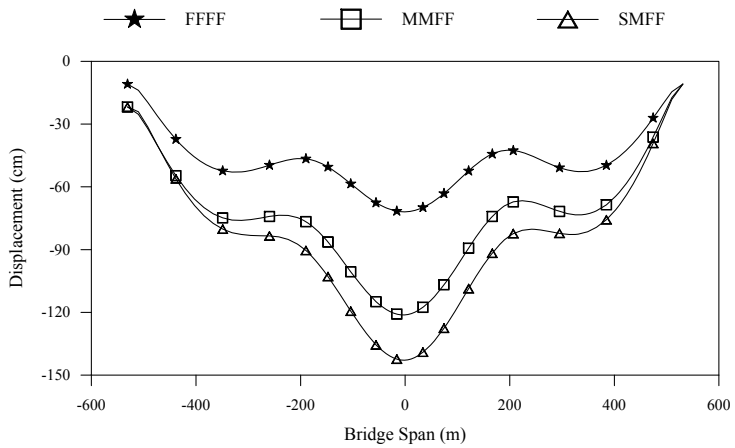

(a) Vertical Displacements

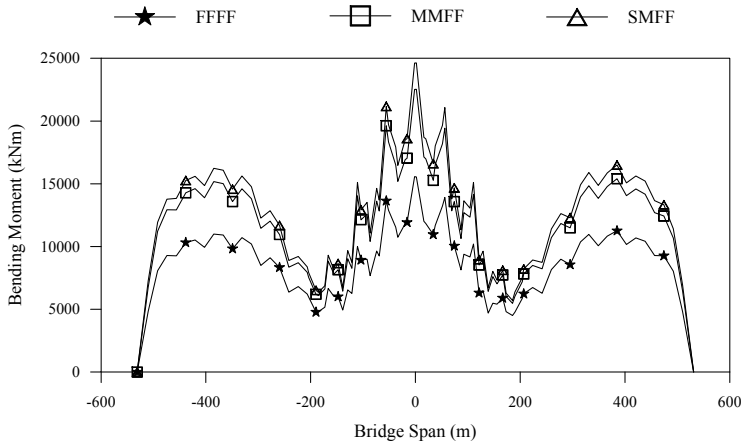

(b) Bending Moments

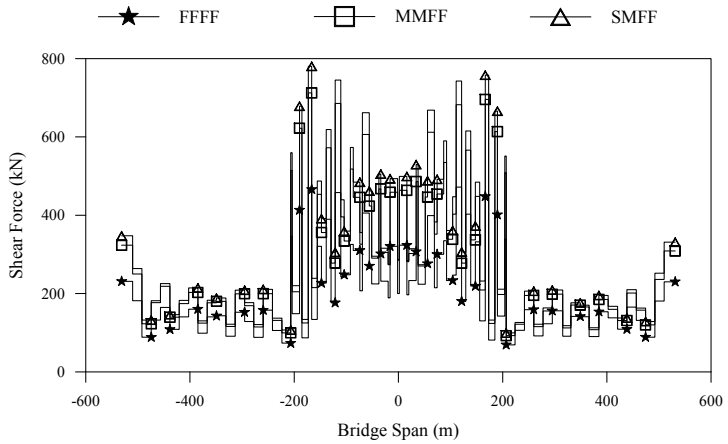

(c) Shear Forces

Figure 6. Mean of Maximum Total Response Values at the Deck for Different Soil Condition Sets under the General Excitation Case

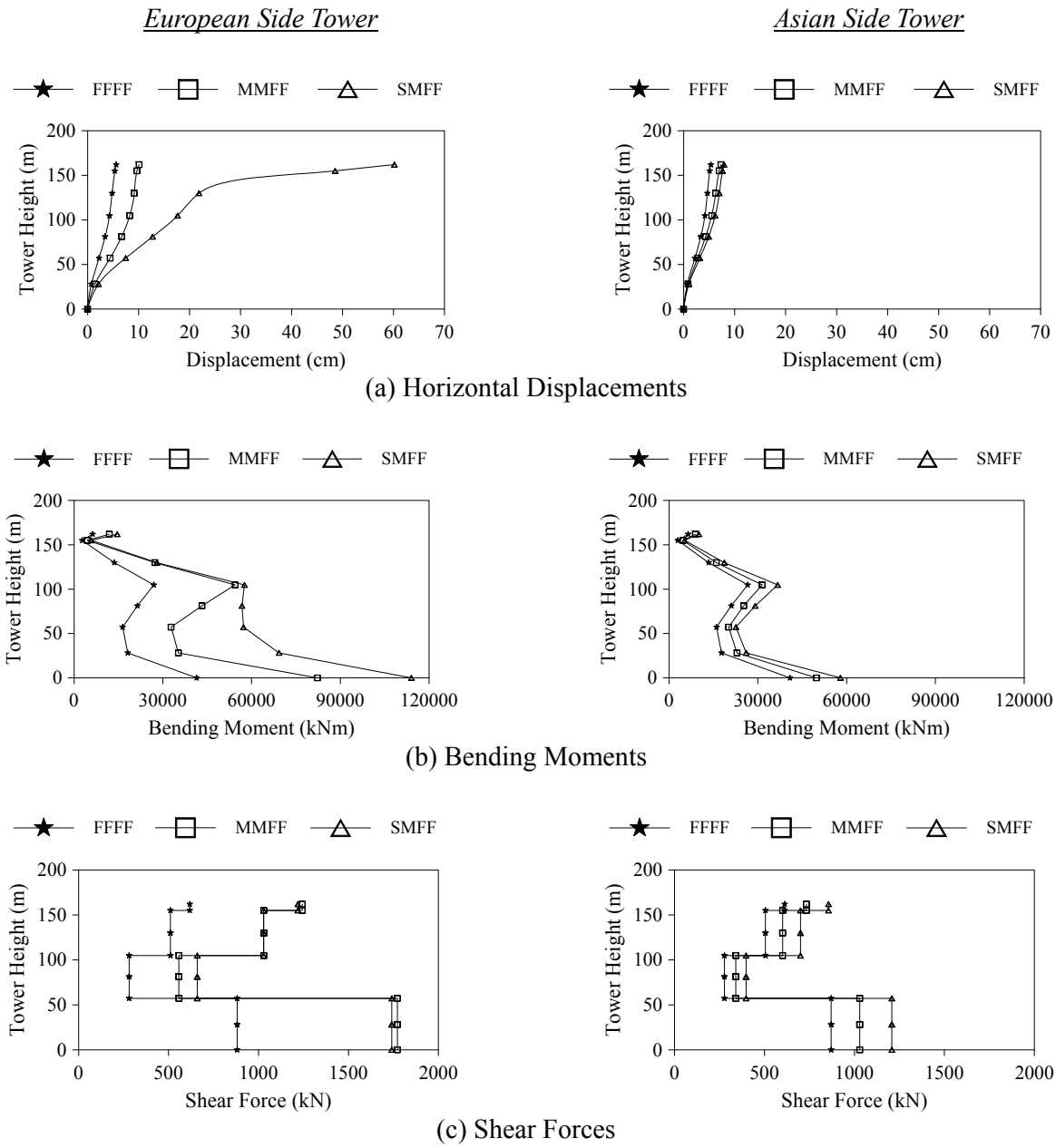

Figure 7. Mean of Maximum Total Response Values at the European and Asian Side Towers for Different Soil Condition Sets under the General Excitation Case

The variance of total response has three components; the pseudo-static component, the dynamic component and the covariance component between the pseudo-static and dynamic components. In this section, the contribution of each component to the total responses of the bridge is investigated. The process of normalisation is performed by dividing the variance values by the maximum total response. The relative contribution of each component to the total vertical displacement along the bridge deck under the general ground motion case is presented in Figure 8 for the FFFF, MMFF and SMFF soil condition sets. It can be observed that the total displacements are dominated by the dynamic component for all the soil condition sets. However, when the soil condition weakens from firm to soft it can be noticed that the contribution of the dynamic component to the total response decreases, and the contribution of the pseudo-static and covariance components increase.

The relative contributions of the response components to the total horizontal tower displacements at the European and Asian side towers are shown in Figure 9 under the general excitation case for the three soil condition sets. While the variations obtained for the displacements at the Asian side tower for each soil condition set are similar to each other, the responses obtained at the European side tower show a different variation. At the top point of the European side tower where the maximum total-horizontal displacement takes place, it can be observed that the dynamic component contributes 65.35%, 41.00%, and 4.66%; the pseudo-static component contributes 40.79%, 55.19%, and 91.86% and the covariance component contributes -6.14%, 3.81%, 3.48% for the FFFF, MMFF, and SMFF soil condition sets, respectively. Similarly, at the top point of the Asian side tower the dynamic component contributes 76.01%, 87.50%, and 92.00%; the pseudo-static component contribute 40.51%, 20.23%, 18.60% and the covariance component contributes -16.52%, -7.73%, and 10.60% for the FFFF, MMFF, and SMFF soil condition sets, respectively. At the European side tower, the total displacements are dominated by the dynamic component for the homogeneous FFFF soil condition case, whereas the total displacements are dominated by the pseudo-static component for the MMFF and SMFF soil condition sets. This can be attributed to the fact that the European side supports are located on weaker soil conditions and hence the pseudo-static components are amplified. The total response is dominated by the dynamic component at the Asian side tower for each soil condition case.

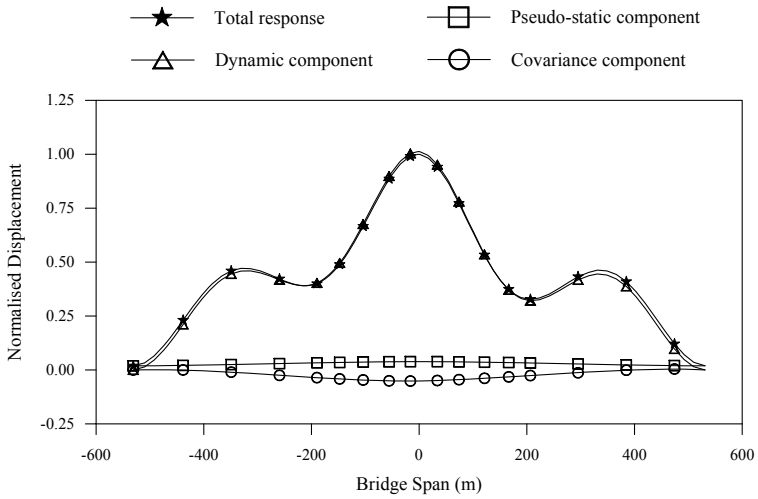

(a) FFFF Soil Condition Case

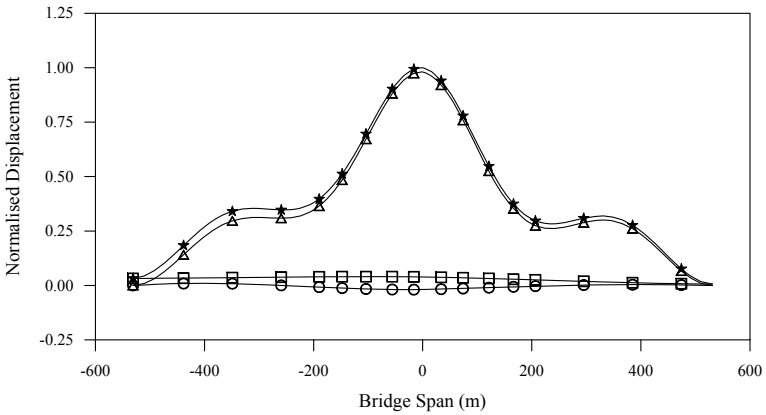

(b) MMFF Soil Condition Case

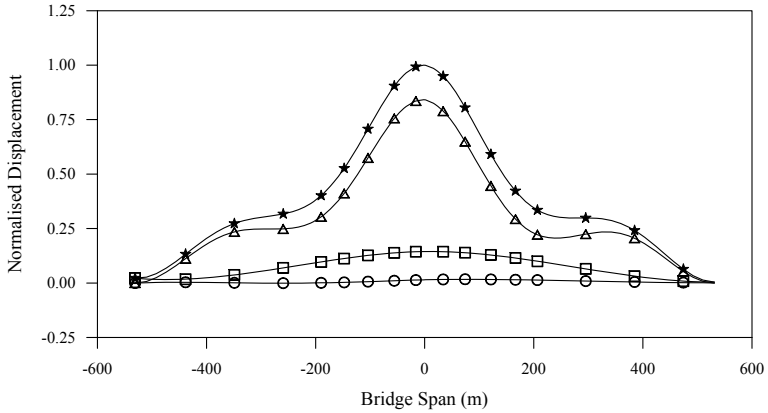

(c) SMFF Soil Condition Case

Figure 8. Normalised Displacement Variances of the Deck for the General Excitation Case

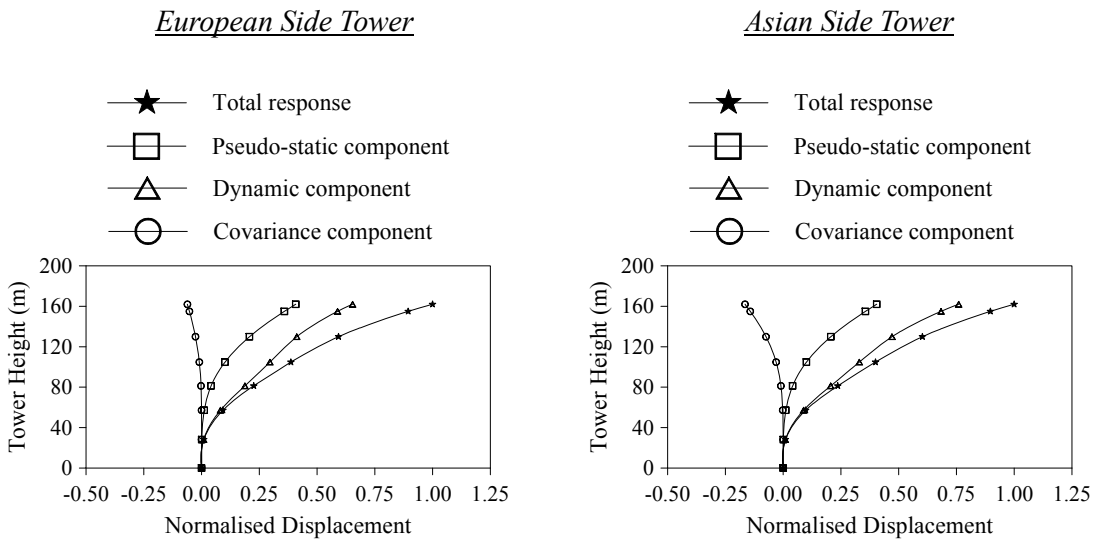

(a) FFFF Soil Condition Case

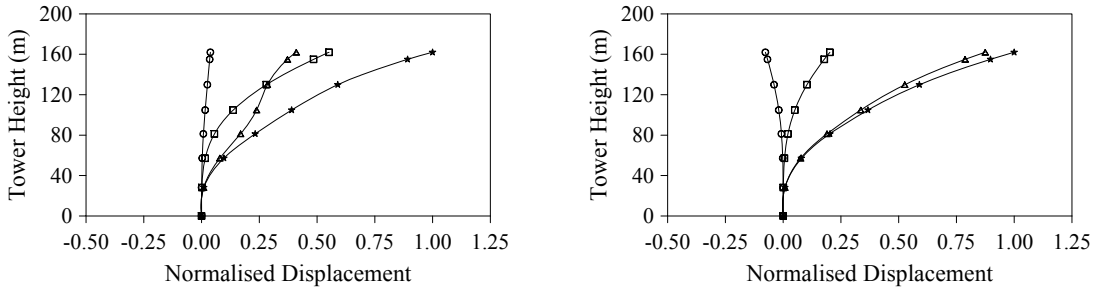

(b) MMFF Soil Condition Case

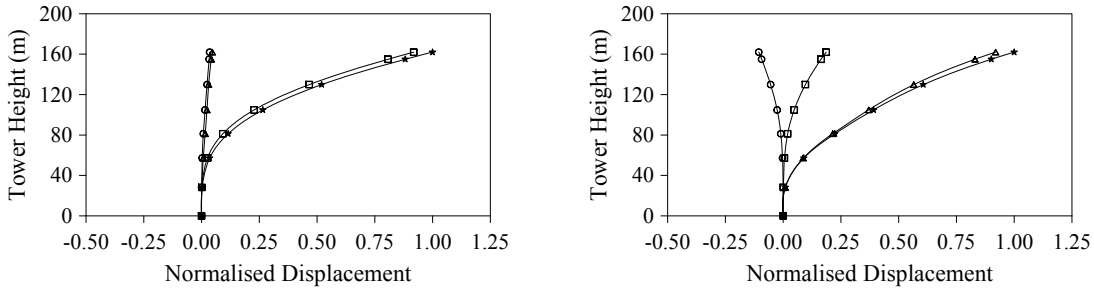

(c) SMFF Soil Condition Case

Figure 9. Normalised Displacement Variances of the European and Asian Side Towers for General Excitation Case

5.2 Comparison of Stationary and Transient Responses

The normalised response values of the vertical deck displacements, bending moments and shear forces are detailed in Figure 10. The transient responses are calculated along the length of the deck at the designated times of 10, 20, 30 and 40 sec and compared with the stationary responses for the SMFF soil condition case (general excitation). Each response has been normalised by dividing it by the corresponding maximum stationary response. As can be observed the stationary response values are larger than those of the transient values. For the total displacements obtained at the middle of the deck; 57.44%, 73.72%, 83.40% and 89.80% of the stationary response is achieved at the times of 10, 20, 30 and 40 seconds of the transient response, respectively. For the total bending moments obtained at the middle of the deck where maximum moments take place; 60.84%, 70.83%, 85.85% and 90.48% of the stationary response is achieved at the times of 10, 20, 30 and 40 seconds of the transient response, respectively. For the total shear forces obtained at the deck where maximum shears occur; 52.70%, 74.57%, 82.56% and 89.74% of the stationary response is achieved at the times of 10, 20, 30 and 40 seconds of the transient response, respectively.

Figure 11 shows the normalised response values of the European and Asian side towers for horizontal displacements, bending moments and shear forces at the times of 10, 20, 30 and 40 sec for the transient response as well as for the stationary response under the general excitation case (SMFF soil condition set). It can be observed that while the response values obtained from the transient analysis are close to those of the stationary analysis at the European side tower at the time of 10 sec, the response values obtained from the transient analysis are close to those of the stationary analysis at the time of 40 sec for the Asian side tower. The reason can be attributed to the fact that while the pseudo-static component dominates the total responses at the European side tower due to the weaker soil condition case (SM), the dynamic component dominates the total responses at the Asian side tower due to the homogeneous stiffer soil conditions (FF). From this point of view the stationary assumption can be accepted as satisfactory for the considered ground motion duration.

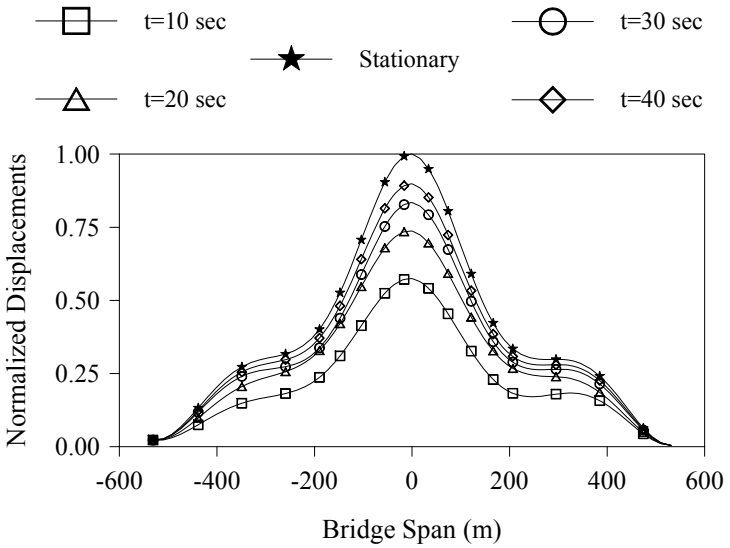

(a) Vertical Displacements

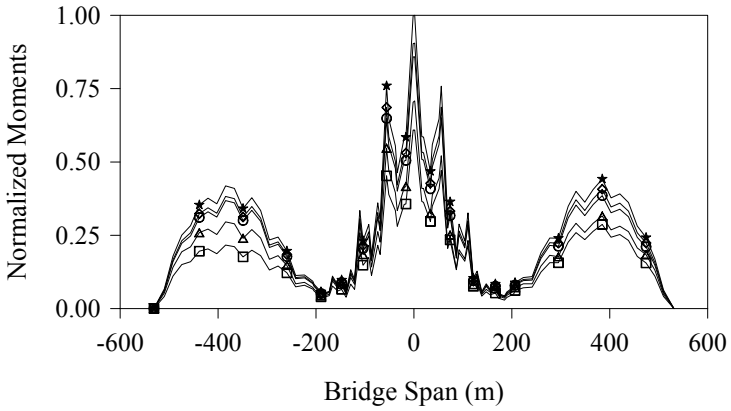

(b) Bending Moments

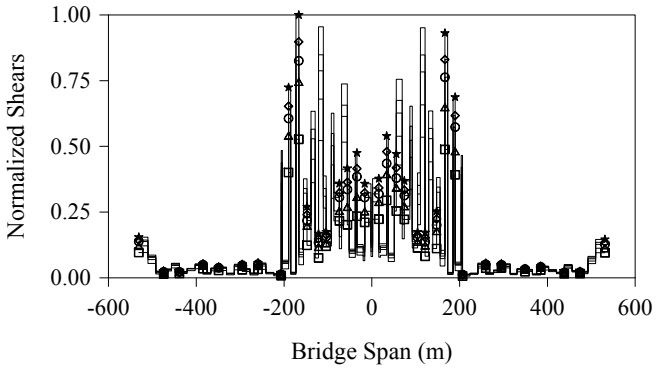

(c) Shear Forces

Figure 10. Normalised Response Values at the Deck Obtained from the Stationary and Transient Analyses under the General Excitation for the SMFF Soil Condition Case

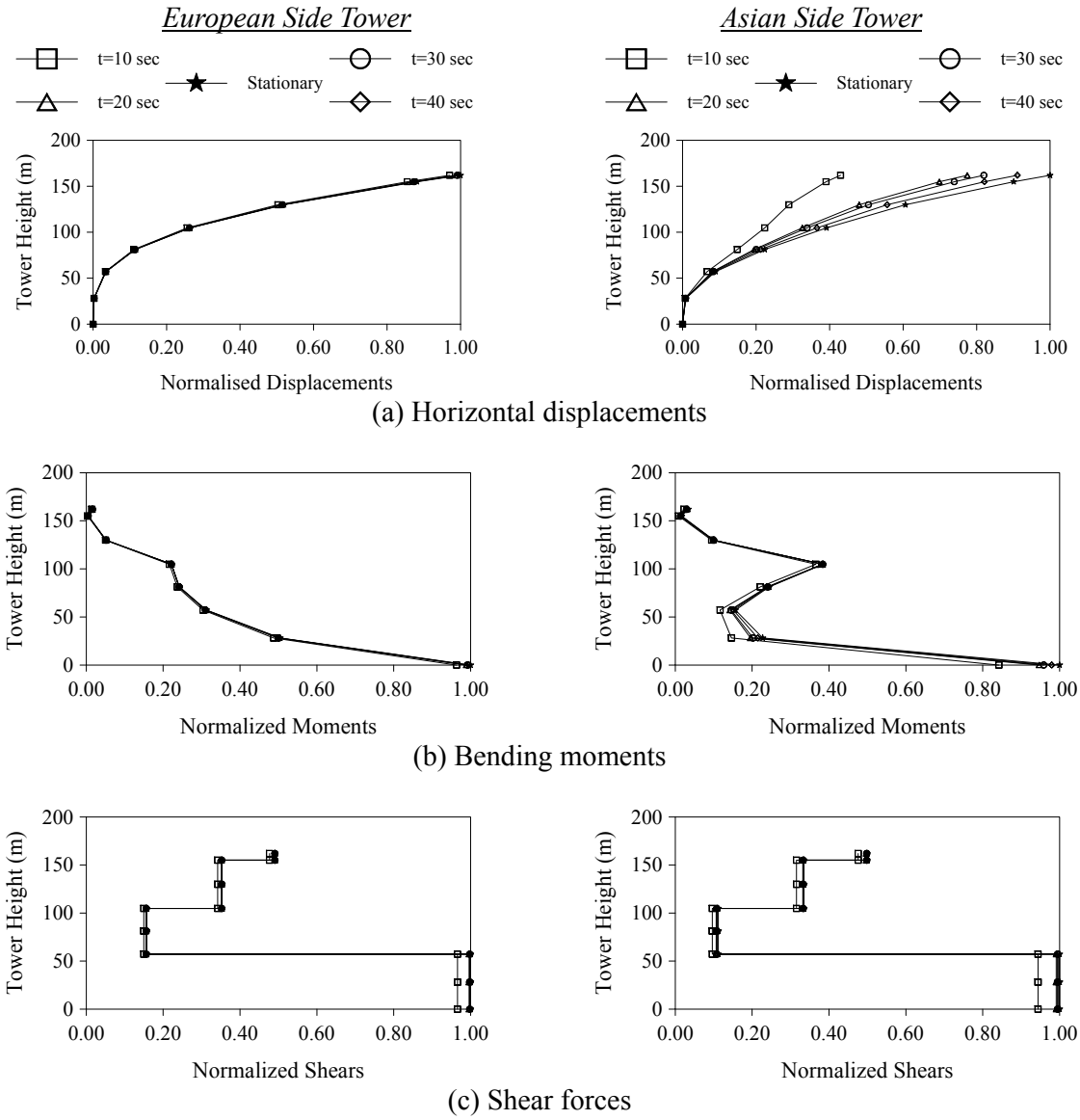

Figure 11. Normalised Response Values at the European and Asian Side Towers Obtained from Stationary and Transient Analyses under the General Excitation for the SMFF Soil Condition Case

The relative contributions of the pseudo-static, dynamic and covariance components to the total displacement responses at the deck, at the European side tower and at the Asian side tower for the stationary analysis and transient analysis at t=10 sec are presented in Figures 12 and 13, respectively. It can be observed that the variation of the transient response is generally consistent with the variation of the stationary response. Because the stationary displacements are generally larger than those of the transient displacements and the pseudo-static displacements are equal for both responses, the contribution of the transient pseudo-static displacements to the total response is increased and the contribution of the transient dynamic components is decreased when compared with those of the stationary contributions. This situation can be observed very clearly on the deck and at the Asian side tower and less noticeably at the European side tower where the total response values are dominated by the pseudo-static component depending on the weaker soil conditions. At the middle of the deck, the contributions of the pseudo-static, dynamic and covariance components to the total response are 14.44%, 84.12% and 1.44% for the stationary analysis and 25.14%,

72.70% and 2.16% for the transient analysis, respectively. At the top of the Asian side tower, the contributions of the pseudo-static, dynamic and covariance components to the total response are 18.60%, 92.00% and -10.60% for the stationary analysis and 43.28%, 81.37% and –24.65% for the transient analysis, respectively. The ratios obtained at the top point of the European side tower are 91.86%, 4.66% and 3.48% for the stationary analysis and 94.66%, 1.81% and 3.53% for the transient analysis, respectively.

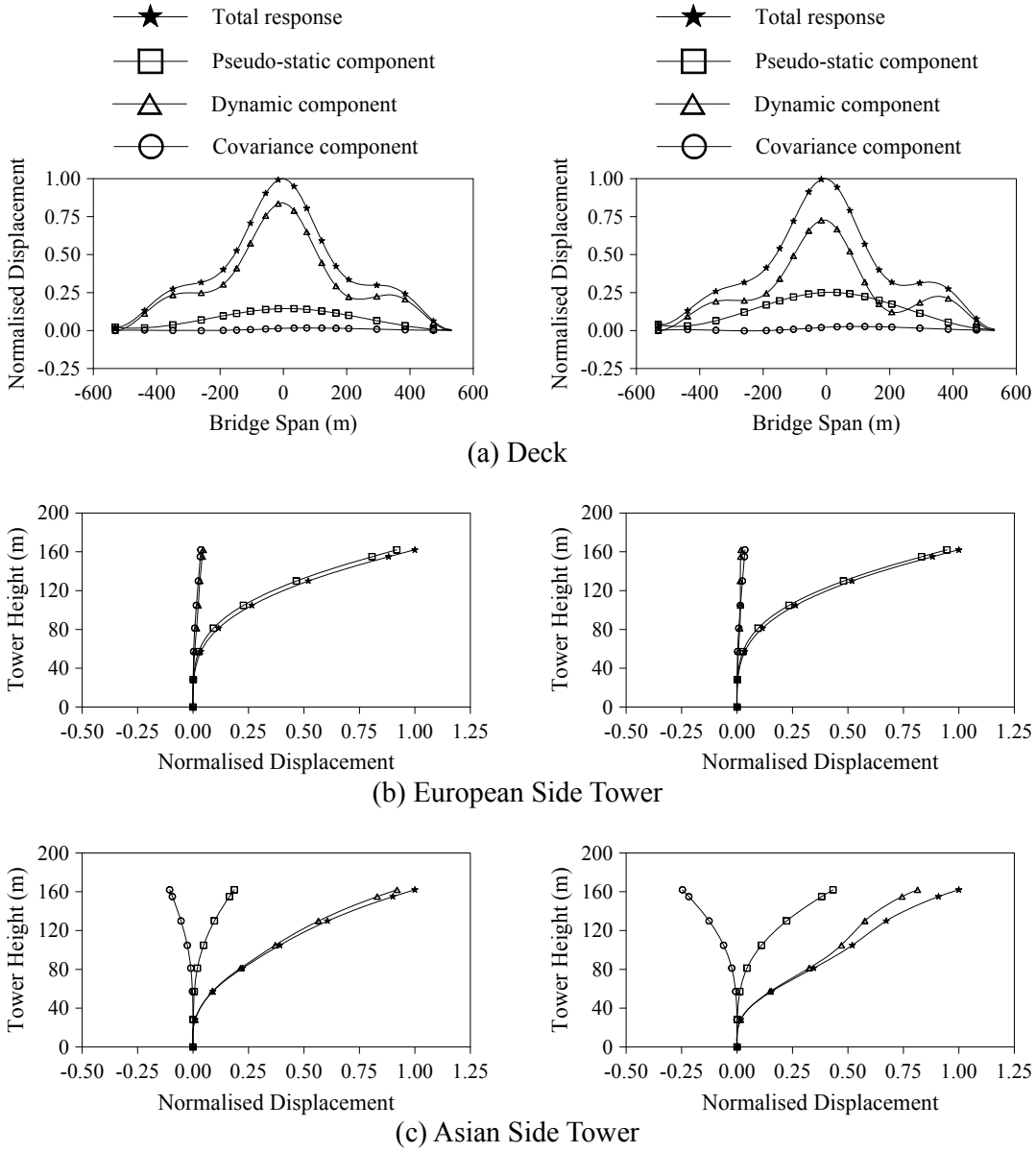

Figure 12. Normalised Stationary Displacement Variances under General Excitation for the SMFF Soil Condition Case

Figure 13. Normalised Transient Displacement Variances at t=10 Seconds under General Excitation for the SMFF Soil Condition Case

6. CONCLUSIONS

The aim of this paper is to determine the stationary and transient responses of the Bosphorus Suspension Bridge, subjected to spatially varying ground motion including the site response effect. The incoherence, wave-passage and site-response effects are examined for the spatially varying ground motion. The site-response effect is investigated in detail by locating the supports of the bridge on distinctly different soil sites. The relative contributions of the pseudo-static, dynamic and covariance components to the total response are presented for both analyses. The main findings from this study can be categorised as follows:

Homogeneous and Heterogeneous Responses

- While the stationary response values obtained for the FFFF (homogeneous) soil condition set are the lowest, the stationary response values obtained for the SMFF soil condition set are the highest. The total displacements and bending moments at the middle of the deck obtained from the general excitation case overestimates the responses by 68.39%, and 98.41% and by 39.64%, and 51.46% for the MMFF, and SMFF soil condition cases, respectively, when compared with the responses due to the FFFF (homogeneous) soil condition case. At the deck point where maximum shear forces take place the total shear forces obtained from the general excitation case overestimate the response by 52.94%, and 67.48% for the MMFF, and SMFF soil condition cases, respectively, when compared with the response due to the FFFF soil condition case.
- While the total vertical displacements at the Asian side for the three different soil condition sets are close to each other, the displacements at the European side for the MMFF and SMFF soil condition sets are larger than those for the FFFF soil condition case.
- The response values obtained for the heterogeneous soil condition cases are larger than those of the homogeneous soil condition case. Also the greater the difference between the soil conditions, the greater the response values.
- The displacement variance values are dominated by the dynamic component at the deck and at the Asian side tower. On the other hand, while the total displacements are dominated by the dynamic component at the European side tower for the homogeneous soil condition case, the pseudo-static component dominates the total displacements for the heterogeneous soil condition cases. Furthermore, the relative contribution of the pseudo-static component to the total response generally increases as the support soil conditions weaken from firm to soft.
- While the variations obtained for the displacements at the Asian side tower for each soil condition set are similar to each other, the responses obtained at the European side tower show a different variation.
- At the top point of the European side tower where maximum total horizontal displacements take place, it can be observed that the dynamic components contributes 65.35%, 41.00%, and 4.66%; the pseudo-static component contributes 40.79%, 55.19% and, 91.86% and the covariance component contributes -6.14%, 3.81%, and 3.48% for the FFFF, MMFF, and SMFF soil condition sets, respectively. At the top point of the Asian side tower the dynamic component contributes 76.01%, 87.50%, and 92.00%; the pseudo-static component contributes 40.51%, 20.23%, and 18.60% and the covariance component contributes -16.52%, -7.73%, -and 10.60% for the FFFF, MMFF, and SMFF soil condition sets, respectively.
- At the European side tower the total displacements are dominated by the dynamic component for the homogeneous FFFF soil condition case, whereas the total displacements are dominated by the pseudo-static component for the MMFF and SMFF soil condition sets. This can be attributed to the fact that the European side supports are located on weaker soil

conditions and hence the pseudo-static components are amplified.
- The total response is dominated by the dynamic component at the Asian side tower for each soil condition case.

Stationary and Transient Responses

- The stationary response values are larger than those of the transient responses.
- For the total displacements obtained at the middle of the deck; 57.44%, 73.72%, 83.40% and 89.80% of the stationary response is achieved at the designated times of 10, 20, 30 and 40 seconds of the transient response, respectively. For the total bending moments obtained at the middle of the deck where maximum moments take place; 60.84%, 70.83%, 85.85% and 90.48% of the stationary response is achieved at the specified times of 10, 20, 30 and 40 seconds of the transient response, respectively. For the total shear forces obtained at the deck where maximum shears occur; 52.70%, 74.57%, 82.56% and 89.74% of the stationary response is achieved at the times of 10, 20, 30 and 40 seconds of the transient response, respectively.
- While the response values obtained from the transient analysis are close to those of the stationary analysis at the European side tower at the designated time of 10 sec, the response values obtained from the transient analysis are close to those of the stationary analysis at the time of 40 sec for the Asian side tower.
- While the pseudo-static component dominates the total responses at the European side tower due to the weaker soil condition case (SM), the dynamic component dominates the total responses at the Asian side tower due to the homogeneous stiffer soil conditions (FF).
- The variation of the pseudo-static, dynamic and covariance components obtained from the transient response analyses are generally consistent with those of the stationary components. Because stationary responses are larger than those of the transient values and the pseudo-static components are equal for both responses, the contribution of the transient pseudo-static components to the total response is increased and the contribution of the transient dynamic components is decreased when compared with those of the stationary contributions.

Due to the complex nature of the problem it is difficult to make general conclusions based on a single suspension bridge model. By comparing the stationary responses with those of the transient responses obtained at various durations of the strong ground shaking used in the stationary analysis, the stationary assumption can be accepted as satisfactory for the considered ground motion duration. However, transient effects could be significant and should be taken into account in earthquakes characterized by shorter durations of strong ground shaking.

REFERENCES

[1] Abdel-Ghaffar, A.M. and Rubin, L.I., ,‘‘Suspension Bridge Response to Multiple-Support Excitations’’, Journal of Engineering Mechanics, 1982, Vol. 108, pp. 419-435.

[2] Abdel-Ghaffar, A.M. and Rubin, L.I., ,‘‘Vertical Seismic Behaviour of Suspension Bridges’’, Earthquake Engineering and Structural Dynamics, 1983, Vol. 11, pp. 1-19.

[3] Harichandran, R.S. and Wang, W., ‘‘Response of One- and Two-Span Beams to Spatially Varying Seismic Excitation’’, Report to the National Science Foundation, MSU-ENGR-88-002, Michigan State University, Michigan, 1988.

[4] Bilici, Y., Bayraktar, A., Soyluk, K., Hacıefendioglu, K., Ateş, S. and Adanur, S., ‘‘Stochastic Dynamic Response of Dam-Reservoir-Foundation Systems to Spatially Varying Earthquake Ground Motions’’, Soil Dynamics and Earthquake Engineering, 2009, Vol. 29, pp. 444-458.

[5] Zhang, D.Y., Liu, W., Xie, W.C. and Pandey, M.D., ‘‘Modeling of Spatially Correlated, Site-Reflected, and Nonstationary Ground Motions Compatible with Response Spectrum’’, Soil Dynamics and Earthquake Engineering, 2013, Vol. 55, pp. 21-32.

[6] Zembaty, Z., ‘‘Vibrations of Bridge Structure Under Kinematic Wave Excitations’’, Journal of Structural Engineering, 1997, Vol. 123, No. 4, pp. 479-487.

[7] Gao, Y., Wu, Y., Li, D., Liu, H. and Zhang, N., ‘‘An Improved Approximation for the Spectral Representation Method in the Simulation of Spatially Varying Ground Motions”, Probabilistic Engineering Mechanics, 2012, Vol. 29, pp. 7-15.

[8] Li, B. and Chouw, N., “Experimental Investigation ff Inelastic Bridge Response Under Spatially Varying Excitations with Pounding”, Engineering Structures, 2014, Vol. 79, pp. 106-116.

[9] Der, Kiureghian, A. and Neuenhofer, A., “A Response Spectrum Method for Multiple-Support Seismic Excitations”, Report No. UCB/EERC-91/08, Berkeley (CA), Earthquake Engineering Research Center, College of Engineering, University of California, 1991.

[10] Nakamura, Y., Der, Kiureghian, A. and Liu, D., “Multiple-Support Response Spectrum Analysis of the Golden Gate Bridge”, Report No. UCB/EERC-93/05, Berkeley (CA), Earthquake Engineering Research Center, College of Engineering, University of California, 1993.

[11] Der, Kiureghian, A., Keshishian, P. and Hakobian, A., “Multiple Support Response Spectrum Analysis of Bridges Including the Site-Response Effect and MSRS Code”, Report No. UCB/EERC-97/02, Berkeley (CA), Earthquake Engineering Research Center, College of Engineering, University of California, 1997.

[12] Rassem, M., Ghobarah, A. and Heidebrecht, A.C., ,‘‘Site Effects on the Seismic Response of a Suspension Bridge”, Engineering Structures, 1996, Vol. 18, pp. 363-370.

[13] Allam, S.M., and Datta, T.K., “Seismic Behaviour of Cable-Stayed Bridges Under Multi-Component Random Ground Motion”, Engineering Structures, 1999, Vol. 22, pp. 62-74.

[14] Allam, S.M. and Datta, T.K., “Analysis of Cable-Stayed Bridges Under Multi-Component Random Ground Motion By Response Spectrum Method”, Engineering Structures, 2000, Vol. 22, pp. 1367-1377.

[15] Soyluk, K. and Sıcacık, E.A., “Soil-Structure Interaction Analysis of Cable-Stayed Bridges for Spatially Varying Ground Motion Components”, Soil Dynamics and Earthquake Engineering, 2012, Vol. 35, pp. 80-90.

[16] Ateş, Ş., Soyluk, K., Dumanoglu, A.A. and Bayraktar, A., “Earthquake Response of Isolated Cable-Stayed Bridges Under Spatially Varying Ground Motions”, Structural Engineering and Mechanics, 2009, Vol. 31, No. 6, pp. 639-662.

[17] Zhang, Y.H., Li, Q.S., Lin, J.H. and Williams, F.W., “Random Vibration Analysis of Long-Span Structures Subjected to Spatially Varying Ground Motions”, Soil Dynamics and Earthquake Engineering, 2009, Vol. 29, No. 4, pp.620-629.

[18] Hawwari, A.R., “Suspension Bridge Response to Spatially Varying Ground Motion”, Ph.D. Thesis, Michigan State University, Michigan, 1992.

[19] Harichandran, R.S., Hawwari, A. and Sweiden, B.N., “Response of Long-Span Bridges to Spatially Varying Ground Motion”, Journal of Structural Engineering, 1996, Vol. 122, No. 5, pp. 476-484.

[20] Adanur, S., Dumanoglu, A.A. and Soyluk, K., “Stochastic Analyses of Suspension Bridges: Stationary and Transient”, In: Grundmann, Schueller, editors. Proceedings of the Fifth European Conference on Structural Dynamics, EURODYN 2002. Rotterdam: A.A. Balkema; 2002.

[21] Jia, H.Y., Zhang, D.Y., Zheng, S.X., Xie, W.C. and Pandey, M.D., "Local Site Effects on a High-Pier Railway Bridge Under Tridirectional Spatial Excitations: Nonstationary Stochastic Analysis", Soil Dynamics and Earthquake Engineering, 2013, Vol. 52, pp. 55-69.

[22] Soyluk, K. and Dumanoglu, A.A., ,''Spatial Variability Effects of Ground Motions on Cable-Stayed Bridges", Soil Dynamics and Earthquake Engineering, 2004, Vol. 24, pp. 241-250.

[23] Perotti, F., "Structural Response to Nonstationary Multiple-Support Random Excitation", Earthquake Engineering and Structural Dynamics, 1990, Vol. 19, pp. 513-527.

[24] Hyun, C.H., Yun, C.B. and Lee, D.G., "Nonstationary Response Analysis of Suspension Bridges for Multiple Support Excitations", Probabilistic Engineering Mechanics, 1992, Vol. 7, pp. 27-35.

[25] Der, Kiureghian, A., "A Coherency Model for Spatially Varying Ground Motions", Earthquake Engineering and Structural Dynamics, 1996, Vol. 25, pp. 99-111.

[26] Harichandran, R.S. and Vanmarcke, .EH., ''Stochastic Variation of Earthquake Ground Motion in Space and Time", Journal of Engineering Mechanics, 1986, Vol. 112, No. 2, pp. 154-174.

[27] Clough, R.W. and Penzien, J., "Dynamics of Structures", Second Edition, Singapore: McGraw Hill, Inc., 1993.

[28] Brown, W.C. and Parsons, M.F., "Bosphorus Bridge, Part I: History of Design", Proc. Instn Civ. Engrs, 1975, Vol. 58, pp. 505-532.

EXPERIMENTAL STUDY ON STABILITY OF HIGH STRENGTH STEEL LONG COLUMNS WITH BOX-SECTIONS

Lei Gao, Kebin Jiang, Linyue Bai* and Qiang Wang

Army Engineering University of PLA, Nanjing 210007, China

**(Corresponding author: E-mail: baily016@sina.com)*

Received: 13 June 2016; Revised: 12 January 2017; Accepted: 25 February 2017

ABSTRACT: Ten long columns made of high strength steel 18Mn2CrMoBA (nominal yield stress is 745 MPa) were employed in axial compression experiments to investigate their overall stability. The columns with thin-walled box-shaped cross-sections were first fabricated into channel shapes followed by welding. The initial geometrical imperfections of the specimens were measured, and the ratio of instability plane initial deflection to the member length was around 1/1000. The finite element model (FEM) which can introduce the influence of geometrical imperfection and residual stress was established. The results of numerical simulation were compared with the experimental results, and the results were in good agreement with the experimental results. Comparisons with Chinese GB50017-2003 specification indicated that the experimental values for the load bearing capacity were greater than that obtained from b-type column curves, but less than a-type column curves. The results were also close to b-type column curves, as defined in the European Eurocode3 steel structure design specification. However, the American ANSI/AISC 360-10 steel structure design specification overestimated the load capacity of this type of long column considered. Therefore, this paper recommends that the design of this type of long column employ the b-type curves specified by the GB50017-2003 or Eurocode3 specifications.

Keywords: High strength steel, thin-walled box-shaped cross-sections, axial compression experiment, load bearing capacity, column curve

DOI: 10.18057/IJASC.2017.13.4.5

1. INTRODUCTION

With the development of steel production processes, high strength steel has been increasingly used to actual projects. Currently, Japan, the United States, and other countries have engaged in an increasing number of engineering projects employing high strength steel [1-3]. The yield strength of high-strength steel mainly ranges between 460 MPa and 690 MPa [3-6], and some super high strength steel having a yield strength of up to 1100 MPa has been applied to rapid bridge construction applications for the military [7]. In recent years, high-strength steel has been increasingly employed in constructions such as the National Stadium of China [8], the new headquarters of China Central Television [9], Phoenix International Media Center [10], and Electrical Transmission Tower [11]. These buildings primarily employed Q460 high-strength structural steel as the construction material. Utilization of high-strength steel can effectively reduce structural self-weight, increase the usage space of a building, and save cost. In addition, high-strength steels with yield strengths exceeding 700 Mpa have been used as building materials for some movable bridge projects in China [12].

While high-strength steel has been widely applied in engineering projects, no specific design specifications for high-strength steel members have yet been developed in China and abroad. The maximum yield strength of steel considered in the Chinese GB50017-2003 specification is 420 MPa [13]; thus, research related to high-strength steel stability must be conducted. Currently, investigators in China and abroad have conducted some degree of research in this field. Usami et al.

[14] conducted stability experimental studies using six columns with box shaped cross-sections made of HT80 high-strength steel with a nominal yield strength of 690 MPa, and an empirical formula was proposed based on their experimental results. Rasumussen et al. [15] implemented compression stability experimental studies using eleven columns with welded H-type or box-shaped cross-sections made of BISALLOY80 high-strength steel with a nominal yield strength of 690 MPa, and their research results demonstrated that the stability coefficient was apparently improved compared to common steel columns with identical normalized slenderness ratios. Yang et al. [16-18] conducted numerous experiments using short and long columns made of G550 high-strength steel with a yield strength of 550 MPa to study their local and overall buckling properties, and numerical simulations were implemented using ABAQUS finite element software. In China, Shi et al. [19-21] performed experimental studies on the stability performance of domestic Q460 high-strength steel welded columns with box-shaped cross-sections as well as the stability performance related to the strong axis of S690 and S960 welded H-shaped compression columns. The results of their investigation demonstrated that the stability coefficient of high-strength steel columns was apparently greater than those of common steel columns. Li et al. [22] implemented axial compression experiments on seven welded columns with box-shaped cross-sections made of domestic Q460 high-strength middle-thick steel plate, and conducted related finite element analysis. They proposed that the stability coefficient could utilize the b-type curve specified in the GB50017-2003 specification [13].

Numerous research results have demonstrated that the use of high-strength steel in axial compression members decreases the sensitivity of the overall stability to initial imperfections [20], and the decreased ratio of the residual stress to the steel yield strength improved the overall stability coefficient of axial compression members [15]. Therefore, it is essential to ascertain whether or not present steel structural design specifications are applicable to high-strength steels through experimental and theoretical investigations. To this end, the present study experimentally evaluated the stability of ten long columns with thin-walled box-shaped cross-sections made of 18Mn2CrMoBA high-strength steel with a nominal yield strength of 745 MPa, and established a finite element model using finite element software to numerically simulate the experimental process. In addition, the experimental results were utilized to study the applicability of the stability design methods for axial compression members fabricated from 18Mn2CrMoBA steel respectively given in the GB50017-2003, American ANSI/AISC 360-10 [23], and European Eurocode3 [24] steel structure design specifications.

2. EXPERIMENTAL OVERVIEW

2.1 Specimen Design

Ten high-strength welded columns made of domestic 18Mn2CrMoBA steel were designed with box-shaped cross-sections. To prepare the specimens, thin steel plate was firstly cold-formed into channel-shaped members, and then thin-walled box-shaped cross-section columns were formed by butt welding. Compared with the commonly employed fabrication method involving the welding of four plates, this preparation method employed only two welds. To prevent end damage during loading, steel plates of 6 mm thickness were welded at the two ends of each specimen. Meter and Vernier calipers were employed to measure the geometrical sizes of specimens, and the actual measured sizes are listed in Table 1. Here, t represents the sectional thickness, L represents the specimen length, H and B represent the sectional height and width of specimens, respectively, and L_0 represents the space between the rotation centers of the unidirectional cylindrical hinge bearings installed at each end of the specimen, where $L_0 = L + 180$ mm, which is discussed in detail in Subsection 2.3.

Table 1. Measured Dimensions of the Actual Specimens

Member number	t /mm	L /mm	H /mm	B /mm	L_0 /mm
LC1a	3.34	416.1	63.06	51.20	596.1
LC1b	3.34	417.3	63.08	51.04	597.3
LC2a	3.34	617.2	62.50	50.12	797.2
LC2b	3.42	616.0	62.34	50.26	796.0
LC3a	3.40	816.4	62.20	50.58	996.4
LC3b	3.40	815.2	62.56	50.34	995.2
LC4a	3.28	1016.6	63.42	49.54	1196.6
LC4b	3.30	1017.1	63.24	50.18	1197.1
LC5a	3.36	1416.2	63.54	50.28	1596.2
LC5b	3.22	1415.3	62.68	50.90	1595.3

The material properties of the specimens utilized, as previously reported [25], are listed in Table 2, where t represents the plate thickness, E represents the elastic modulus, f_y represents the nominal yield strength, f_u represents the limited tensile strength, and f_y/f_u represents the yield ratio.

Table 2. Experimental Results of the Material Properties

Specimen number	t /mm	E /GPa	f_y /MPa	f_u /MPa	f_y/f_u
ts1	3.44	194.9	795	935	0.8502
ts2	3.30	196.2	791	921	0.8588
ts3	3.34	198.6	794	929	0.8546
Average	3.36	196.6	793.3	928.3	0.8545

2.2 Measurement of the Initial Geometrical Imperfections of Specimens

Meter and feeler gauges were employed to measure the initial geometrical imperfections of the specimens. The measurements primarily included the initial deformation along the weak axis, i.e., in the instability plane. The front and back planes were respectively measured. Three lines in each plane comprised of two edge lines and one middle line were measured. Four testing points along each line comprised of two end points and two quartile points were tested, and the maximum values of the measured results was treated as the initial geometrical imperfections, which are listed in Table 3, where δ represents the measured average initial imperfection value. It is observed from Table 3 that the ratio of δ/L was about 1/1000, which verifies the applicability of using 1/1000th of the member length specified in the GB50017-2003 specification [13] as the standard value of the initial imperfection.

Table 3. Initial Geometrical Imperfections along the Weak Axis

Specimen number	L /mm	δ /mm	δ /L
LC1a	416.1	0.37	1124
LC1b	417.3	0.39	1070
LC2a	617.2	0.58	1064
LC2b	616.0	0.61	1009
LC3a	816.4	0.79	1033
LC3b	815.2	0.82	994
LC4a	1016.6	0.93	1093
LC4b	1017.1	1.12	908
LC5a	1416.2	2.93	483
LC5b	1415.3	1.48	956

2.3 Experimental Equipment

The experiment utilized a 5000 kN hydraulic testing apparatus for vertical loading. A universal ball hinge was installed at the upper end of the loading equipment, allowing for free rotation. To ensure that the specimen could show buckling features along the weak axis, a unidirectional cylindrical hinge was installed at each end of the specimen, as shown in Figure 1. Meanwhile, to ensure member connection with the cylindrical hinge, a 15 mm thick loading plate was welded to the end of the specimen. Into the plate was cut a 5 mm slot wherein the specimen was inserted. The distance between the center of the cylinder and the loading plate was 80 mm; thus, $L_0 = L + 180$ mm, as discussed above. Loading proceeded in discrete steps followed by a pause of 30 s for measurement reading. For loading levels sufficiently far from the ultimate load capacity, specimens were loaded in increments of 10 to 20 kN; however, as the loading approached the ultimate load capacity, specimens were loaded in increments of 1 to 5 kN.

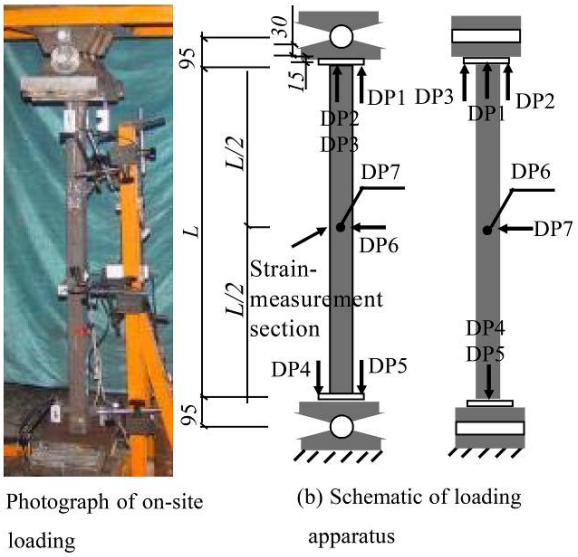

(a) Photograph of on-site loading

(b) Schematic of loading apparatus

Figure 1. Schematic of the Experimental Loading Apparatus

3. EXPERIMENTAL RESULTS AND ANALYSIS

3.1 Instability Modes and Deformation Analysis

The status of the failed specimens, as shown in Figure 2, demonstrated a overall instability failure mode. This failure is a type of limit point instability affected by initial imperfections, eccentric loading, and other factors. The specimens exhibited a smaller horizontal deformation during the early stage of loading, and, with a gradually increasing load, the horizontal deformation gradually increased, and presented apparent bending deformation around the weak axis. The tensile strain occurreded on the sectional convex side of the middle span; meanwhile, the compressive strain on the concave side gradually increased until it yielded to a plastic state, although the load could continue increasing. With the development of sectional plasticity and increased bending deformation, specimens could withstand no greater load. Thus, an overall buckling phenomenon became true when the load was reduced. It is observed from Figure 2 that bending deformation became increasingly evident with an increasing specimen slenderness ratio, and instability failure occurred more readily.

Figure 2. Photographs of Specimen Failure

Figures 3(a) and (b) present the relationships between the testing load and the axial displacement at bearings for specimens LC3b and LC4a, respectively. For simplicity, the bearing downside displacement was treated as positive when the displacement meter was compressed; and treated as negative under a tensioned displacement meter. An apparent deformation is observed from the figures at testing point DP1, employed for monitoring rotation at the upper bearing. When the specimens reached their load limit, the upper bearing exhibited a larger rotation, and the displacement meter extended; accordingly, the load and displacement decreased. The experimental results indicate that the upper bearing can represent the end constraint of a simply supported hinge. For the two testing points DP4 and DP5, employed for monitoring rotation at the lower bearing, it is observed from Figure 3(b) that nearly no displacement occurred during the process of loading up to the load limit. This indicates an absence of rotation, and only slight rotation occurred after attaining the load limit of specimens. Therefore, the lower bearing cannot be treated as a hinge bearing, but, rather, as a fixed end constraint over the entire loading process. Accordingly, the specimen constraints were treated as simply supported on one end and a fixed support on the other end. The member length calculation coefficient for the specimen slenderness ratio was 0.7. Specimen LC5a exhibited a maximum initial imperfection. In this case, the reinforcing plate at its lower end fell off during loading, which introduced a large gap between the end and the loading plate, and rotation at the lower hinge during loading; therefore, LC5a could be treated according to a simply supported constraint with a member length coefficient of 1. The corresponding calculation lengths L_j for the specimens are presented in Table 4.

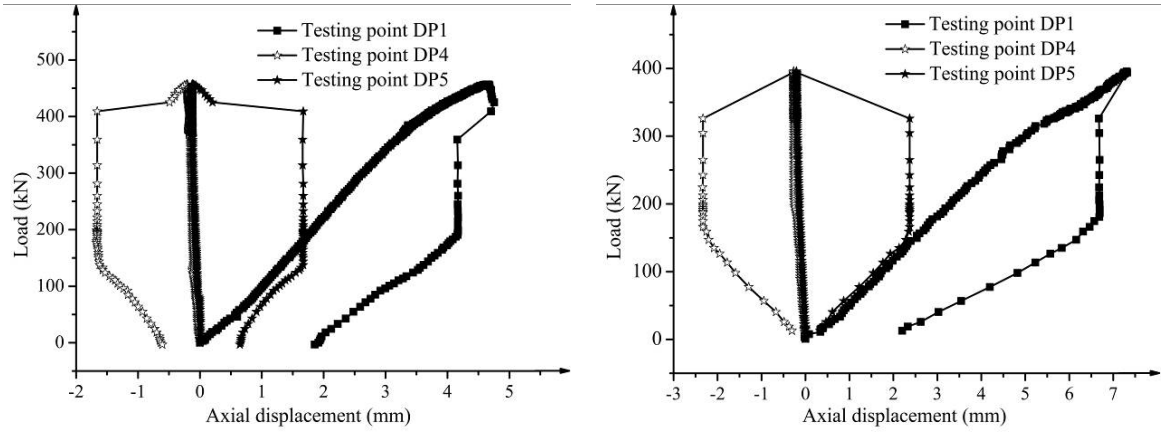

(a) Specimen LC3b (b) Specimen LC4a

Figure 3. Axial Displacement Curve of the Specimen Bearing

3.2 Stability Capacity

The experimentally determined limit capacities of the specimens are provided in Table 4, where P_y represents the capacity, and $P_y = Af_y$ when the section was fully yielded. A represents the section area of the specimens, P_{ut} represents the stability capacity, λ_y represents the slenderness ratio along the weak axis of the specimen, and λ_n represents the normalized slenderness ratio, which, according to the GB50017-2003 specification [13], can be calculated as

$$\lambda_n = \frac{\lambda_y}{\pi}\sqrt{f_y / E}. \quad (1)$$

The overall stability coefficient φ_t was determined by

$$\varphi_t = P_{ut} / P_y. \quad (2)$$

Table 4. Stability Capacities and Normalized Slenderness Ratios

Specimen number	L_j/mm	λ_y	λ_n	P_y/kN	P_{ut}/kN	φ_t
LC1a	417.3	20.74	0.419	570.1	559.6	0.9816
LC1b	418.1	20.84	0.421	569.4	558.4	0.9807
LC2a	558.0	28.33	0.573	561.4	513.5	0.9147
LC2b	557.2	28.27	0.572	573.9	515.7	0.8986
LC3a	697.5	35.16	0.711	571.7	463.5	0.8107
LC3b	696.6	35.26	0.713	572.4	456.8	0.7980
LC4a	837.6	42.86	0.867	553.7	395.7	0.7146
LC4b	838.0	42.41	0.857	559.3	435.3	0.7783
LC5a	1596.2	80.67	1.631	570.9	182.9	0.3204
LC5b	1116.7	55.73	1.127	547.4	366.6	0.6697

4. FINITE ELEMENT NUMERICAL SIMULATION

4.1 Finite Element Model

The present research utilized ANSYS [26] software to establish a finite element analysis model, and to conduct numerical simulations. To consider the local buckling and overall relative buckling of the box-shaped cross-section fabricated by welding trough-shaped steel plate, shell elements (shell181), rather than beam elements, were employed. A finite element model based on the elastoplastic large deflection theory of a thin plate was established. Based on the stress-strain curve of the material [25], a multi-linear isotropic strengthening model was selected for the material model. To incorporate the rigid boundary assumption into the model, and to facilitate the application of constraints and loading, two rigid steel plates having a very high elastic modulus were added to the two ends of the member model, and the nodes at the middle of the two end plates were constrained. The established finite element model and constraint modes are presented in Figure 4.

The actual members exhibit a variety of imperfections, which mainly include mechanical imperfections, such as residual stress, and geometrical imperfections such as initial bending, initial member eccentricity, and the initial bending of the plate element. Of these, the numerical simulation should consider the residual stress, the overall initial deflection of a member, and the local imperfections of the plate element.

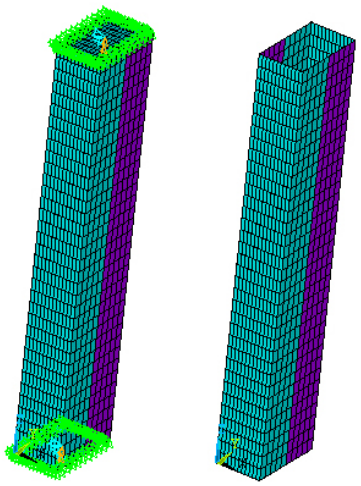

Figure 4. Finite Element Model

4.1.1 Introduction of geometrical imperfections

Beginning with the basic model, the locations of nodes were altered according to a semi-sine wave, and the maximum initial deflections listed in Table 3 were applied to the nodes of the model. After alteration of node locations, new elements were generated to establish the overall model.

The consistent imperfection mode method was applied to local defects. An eigenvalue buckling analysis of the structure was conducted to determine the first local buckling mode, which was treated as the reference mode. The obtained reference mode was multiplied by the factor that made the maximum deformation of local buckling equal to the maximum local imperfection amplitude Δ_0, and was then applied to the finite element model. The maximum local imperfection amplitude Δ_0 was determined by Eq. 3, as proposed by Mateus [27].

$$\Delta_0 = 0.1\beta^2 \tag{3}$$

Here, $\beta = b/t\sqrt{\sigma_y / E}$, where b is the width to thickness ratio, and σ_y is the yield strength. Substituting this expression for β into Equation (3) yields

$$\Delta_0 / b = 0.1 \times b / t \times \sigma_y / E. \tag{4}$$

4.1.2 Introduction of mechanical imperfection

Shen et al. [28] tested the residual stresses for numerous box-shaped cross-sections made of lower high-strength channel steel, and proposed the residual stress model shown in Figure 5. The researchers proposed that the residual tensile stress σ_{rt} be given as $0.832f_y$, and the residual compressive stress σ_{rc} be given as $0.0839f_y$. The actual residual stress for box-shaped cross-section members formed by welding cold-rolled trough-shaped steel employed in the present research was a compound stress comprised of cold-bending and welding residual stresses, which are very complicated. To simplify the calculation, the present study employed $0.8f_y$ for σ_{rt} and $0.1f_y$ for σ_{rc}, and the residual stress model employed is shown in Figure 5.

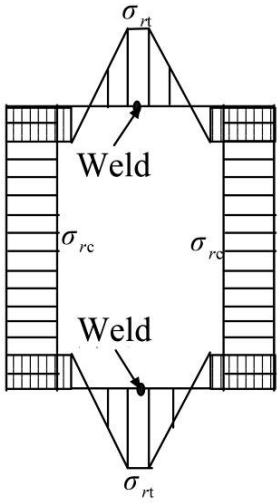

Figure 5. Diagram of the Residual Stress Model

The application of residual stress utilized the method of recording residual stress data [29]. A residual stress data file was prepared for every element in the finite element model, and then the data files were introduced into the model by reading them in the ANSYS software. Every shell181 element has five integration points, so residual stress was applied at the location of integration point of every element.

After constructing the model, the arc-length method was employed for the solution. During the solving process, the applied load, the adopted loading step, and the arc radius were adjusted to ensure tracking of the section where the load-displacement was decreasing. This process was at times repeated to achieve satisfactory results. After completion of the solving process, the universal time processer was used to capture the load-displacement curves of those nodes for which the load limit capacity was attained. A program was prepared for the present study to compute the stability of the modeled steel members using the ANSYS parametric design language [26]. Figure 6 presents the programming flow chart.

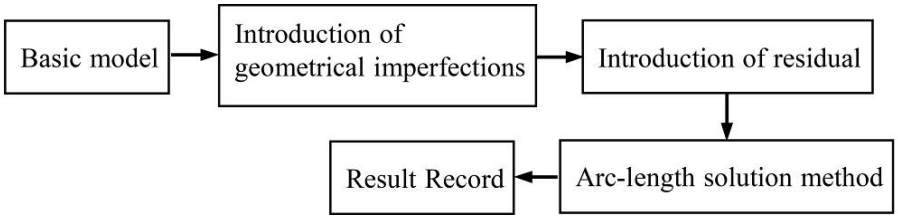

Figure 6. Program Flow Diagram for Computing the Stability of the Modeled Steel Members

4.2 Numerical Simulation Results

Table 5 lists the results of all finite element numerical simulation results and their experimental counterparts for comparison. Figure 7 presents a comparison of the load-displacement curves.

Table 5. Comparison of the Experimental Results and the Results of Finite Element Numerical simulation

Number	P_{us} /Kn	P_{ut} /kN	$(P_{ut} - P_{us})/P_{ut}$ /%
LC1a	559.6	565.7	1.07
LC1b	556.2	558.4	0.39
LC2a	488.1	513.5	4.94
LC2b	489.5	515.7	5.08
LC3a	441.5	463.5	4.74
LC3b	442.6	456.8	3.11
LC4a	409.8	395.7	−3.56
LC4b	413.2	435.3	5.07
LC5a	193.7	182.9	−5.90
LC5b	559.6	565.7	1.07

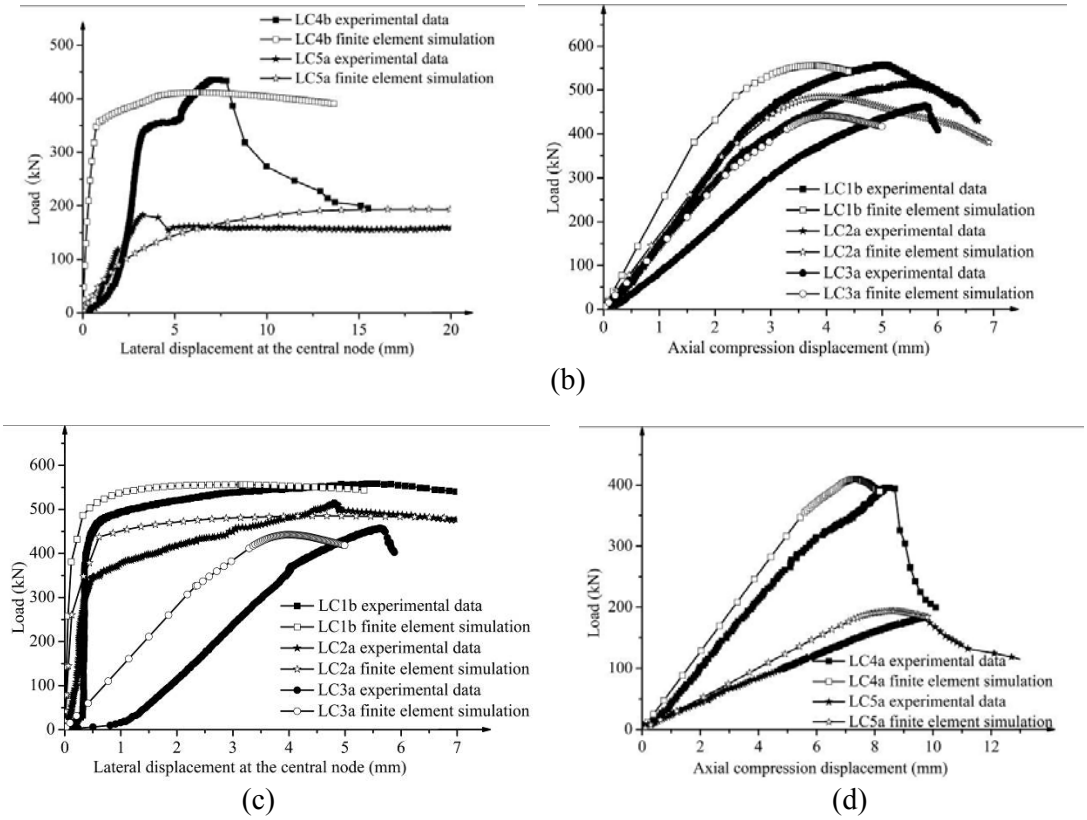

Figure 7. Comparison of Experimental Load Displacements with those obtained from Finite Element Numerical Simulation

Table 5 shows that, except for specimen LC5, the difference between the finite element numerical simulation results and the experimental results are within 5%. Figure 7 indicates that the individual load-displacement curves obtained from finite element numerical simulation and experiment exhibit an identical trend, representing good agreement between simulation and experiment. Therefore, the finite element model proposed here accurately simulates the compression process of thin-walled box-shaped cross-section members made of 18Mn2CrMoBA high-strength steel.

5. COMPARISON WITH SPECIFICATIONS

Figure 8 presents a comparison between the obtained experimental results and those obtained based on the GB 50017-2003 specification [13].

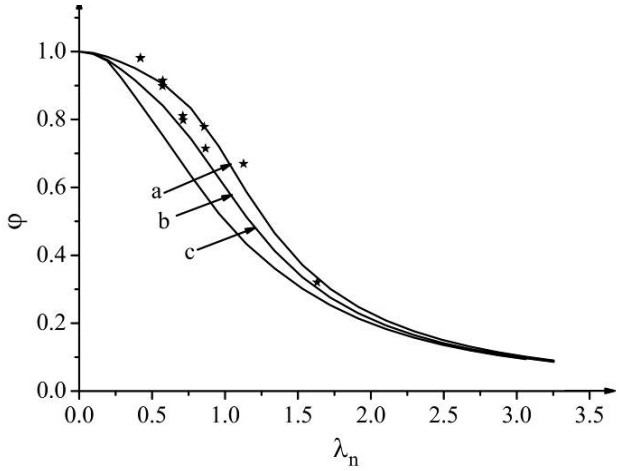

Figure 8. Comparison of Experimental Results and the Results obtained from the Chinese GB 50017-2003 Specification

The bending buckling capacity calculation formula for axial compression members provided by the ANSI/AISC 360-5/360-10 specification [23] is given as follows. The stability capacity P_n is given as

$$P_n = F_{cr} A_g \tag{5}$$

where A_g is the gross sectional area and F_{cr} is the buckling stress. F_{cr} can be calculated by the following formula.

$$F_{cr} = [0.658^{\frac{f_y}{F_e}}] f_y, \quad \frac{KL}{r} \leq 4.71\sqrt{\frac{E}{f_y}} \tag{6}$$

$$F_{cr} = 0.877 F_e, \quad \frac{KL}{r} > 4.71\sqrt{\frac{E}{f_y}} \tag{7}$$

Here, the following definitions are applied:

K is the calculation length coefficient of the column;
R is the sectional radius of gyration;
KL/r is the column slenderness ratio λ;
F_e is the elastic buckling critical stress, given as $F_e = \pi^2 E / (KL / r)^2$.

When the local buckling of the plate member is not taken into consideration, the normalized slenderness ratio $\lambda_n = \frac{\lambda}{\pi}\sqrt{\frac{f_y}{E}}$ and the overall stability coefficient $\varphi = P_n/(f_y A_g)$ are introduced to obtain a column curve calculation formula similar to the GB 50017-2003 specification:

$$\varphi = 0.658^{\lambda_n^2}, \lambda_n \leq 1.499, \tag{8}$$

$$\varphi = 0.877 / \lambda_n^2, \lambda_n > 1.499. \tag{9}$$

The Eurocode3 specification [24] classifies member sections into four types according to the degree to which capacity and rotation capability are influenced by local buckling. When the overall buckling is considered as the primary buckling mode, the corresponding capacity calculation formula is given as follows. The stability capacity $N_{b.Rd}$ is given as

$$N_{b,Rd} = \frac{\chi A f_y}{\gamma_{M1}}, \tag{10}$$

where A is the gross sectional area of a member and χ is the overall stability factor. χ is calculated as

$$\chi = \frac{1}{\phi + \sqrt{\phi^2 - \bar{\lambda}^2}}, \text{ for } \chi \le 1. \tag{11}$$

Here, the following definitions are applied:

$$\phi = 0.5[1 + \alpha(\bar{\lambda} - 0.2) + \bar{\lambda}^2] \tag{12}$$

$\bar{\lambda}$ is the normalized slenderness ratio;
α is the imperfection influence factor;
γ_{M1} is the resistance factor for stability design, which is 1 for a building structure.

Every column curve corresponds to a specific value of imperfection influence, and five column curves are specified. A welded box-shaped cross-section member belongs to category III or II of the column curve. When the width-thickness ratio is less than 30, the member belongs to category III and $\alpha = 0.34$, and it belongs to category II and $\alpha = 0.49$ when the width-thickness ratio is equal to or greater than 30.

Figure 9 provides a comparison between the experimental results and calculation results based on Eqs. 8, 9, and 11 for the load bearing capacity of the members considered. Figure 9 indicates that some of the experimental load bearing capacity results were greater, but a few individual data were 3.5% lower than those obtained by the ANSI/AISC 360-5/360-10 specification. However, the experimental load bearing capacity results were 8.9% greater than that of the category-b column specified in the Eurocode3 specification, and were similar to that of the category-b curve of the GB 50017-2003 specification, while exhibiting a 13.2% difference from that of the category-c curve.

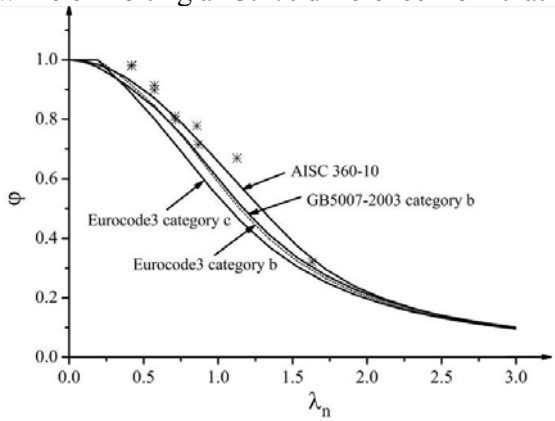

Figure 9. Comparison between the experimental results for the load bearing capacity of the members and those obtained from the European Eurocode3 and American ANSI/AISC 360-10 specifications

6. CONCLUSION

Ten long columns made of high strength steel were employed in axial compression experiments to investigate their overall stability and load bearing capacity under axial compression. The columns had thin-walled box-shaped cross-sections, and were made of 18Mn2CrMoBA cold-formed steel that was first made into channel shapes followed by butt welding. The results of the study can be summarized as follows.

(1) Measurements of the overall initial imperfections of specimens indicated that the initial deflection of the instability plane can be based on 1/1000th of the member length, as given by the GB 50017-2003 specification for the design process.

(2) Axial compression tests exhibited an overall bending instability mode.

(3) Comparison between the results of experiment and finite element numerical simulation indicated that the proposed finite element model comprehensively captured the influence of initial geometrical imperfection and residual stress on the stability and load bearing capacity of the long columns considered, and could therefore accurately predict these characteristics.

(4) The load bearing capacity attained from specimens was greater than that of the category-b curve of the GB 50017-2003 specification, but lower than that of the category-a curve. The load bearing capacity of specimens was close to that of the category-b curve of the Eurocode3 specification. Meanwhile, the ANSI/AISC 360-10 specification overestimated the load capacity of the type of steel columns considered.

(5) This research recommends using the category-b curve of the GB 50017-2003 specification and the category-b curve of the Eurocode3 specification for design of long columns with thin-walled box-shaped cross-sections made of 18Mn2CrMoBA high-strength steel.

ACKNOWLEDGEMENTS

This research work was financial supported by the Major State Basic Research Development of China (973 Program, Grant No.2014CB046801).

REFERENCE

[1] Pocock, G., “High Strength Steel Use in Australia, Japan and the US”, J. Structural Engineer, 2006, Vol. 84, No. 21, pp. 27-30.

[2] Fukumoto, Y., “New Constructional Steels and Structural Stability”, J. Engineering Structures, 1996, Vol. 18, No. 10, pp. 786-791.

[3] Rosier, G.A. and Groll, J.E., “High Strength Quenched and Tempered Steels in Structures”, J. Steel Construction, 1987, Vol. 21, No. 3, pp. 2-13.

[4] Cui, W., “Recent Research Advances and Application of High Strength Steel Structures”, J. Building Structure, 2011, Vol. 41 (supplement), pp. 958-963.

[5] Shi, G., Ban, H.Y., Shi, Y.J. and Wang, Y.Q., “Overview of Research Progress for High Strength Steel Structures”, J. Engineering Mechanics, 2013, Vol. 30, No. 1, pp. 1-13.

[6] Günther, H.P., “Use and Application of High-performance Steels for Steel Structures”, M. Zurich, Switzerland: ETH Honggerberg, 2006.

[7] Li, G.Q., Wang, Y.B., Chen, S.W. and Sun, F.F., “State of the Art on Research of High Strength Structural Steels and Key Issues of Using High Strength Steels in Seismic Structures”, J. Journal of Building Structures, 2013, Vol. 34, No. 1, pp. 1-13.

[8] Fan, Z., Liu, X.M., Fan, X.W., Hu, C.Y., et al., ”Design and Research of Large-span Steel Structure for the National Stadium”, Journal of Building Structures, 2007, Vol. 28, No. 2, pp. 1-16.

[9] Chen, Z.M., Zhang, Y.L., Peng, M.X. and Zhang, K., "Application of High-strength Steel and Thick Steel Plates to CCTV New Site Building", J. Steel Construction, 2009, Vol. 24, No. 2, pp. 34-38.
[10] Zhou, S.H., Zhu, Z.Y., Qi, W.H., et al., "Structural Design on the Project of Phoenix International Media Center", J. Building Structure, 2011, Vol. 41, No. 9, pp. 56-62.
[11] Li, Z.L., Liu, H.J., Zhang, D.Y. and Li, M.H., "Application of High-strength Steel Q460 in 1000kv Transmission Towers", J. Power System Technology, 2008, Vol. 32, No. 24, pp. 1-5.
[12] Gou, M.K. and Tao, L., The Application of High Strength Steel ($\sigma_s \geq 700$MPa) To Movable Bridge", J. Steel Structure, 2002, Vol. 17, No. 61, pp. 6-9.
[13] GB50017-2003 Code for design of steel structures[S].Beijing: China Planning Press, 2003.
[14] Tsutomu, Usami, Yuhshi, Fukumoto, "Local and Overall Buckling of Welded Box Columns", Journal of Structural Division (ASCE), 1982, Vol. 108, No. ST3, pp. 525-542.
[15] Rasmussen, K.J.R. and Hancock, G.J., "Tests of High Strength Columns", Journal of Constructional Steel Research, 1995, Vol. 34, No. 1, pp. 27-52.
[16] Yang, D. and Hancock, G.J., "Compression Tests of Cold-reduced High Strength Steel Sections, I: stub columns", Journal of Structural Engineering, 2004, Vol. 130, No. 11, pp. 1772-1781.
[17] Yang, D., Hancock, G.J., Ramussen, K.J.R., "Compression Tests of Cold-reduced High Strength Steel Sections, II: Long Columns", Journal of Structural Engineering, 2004, Vol. 130, No. 11, pp. 1782-1789.
[18] Yang, D. and Hancock, G.J., "Numerical Simulation of High-strength Steel Box-shaped Columns Failing in Local and Overall Buckling Modes", Journal of Structural Engineering, 2006, Vol. 132, No. 4, pp. 541-549.
[19] Shi, G., Lin, C.C., Wang, Y.Q. and Shi, Y.J., "Experimental Study on Local Buckling of High Strength Steel I-section Stub Columns under Axial Compression", Journal of Building Structures, 2012, Vol. 33, No. 12, pp. 20-30.
[20] Ban, H.Y., Shi, G., Shi, Y.J. and Wang, Y.Q., "Overall Buckling Behavior of Q460 High Strength Steel Welded Box Section Columns under Axial Compression", Journal of Building Structures, 2013, Vol. 34, No. 1, pp. 22-29.
[21] Shi, G., Ban, H.Y., Bijlaard, F.S.K., et al., "Experimental Study and Finite Element Analysis on the Overall Buckling Behavior for Ultra-high Strength Steel Compression Members with End Restraints", China Civil Engineering Journal, 2011, Vol. 44, No. 10, pp. 17-25.
[22] Li, G.Q., Wang, Y.B. and Chen, S.W., "Experimental Study on Ultimate Bearing Capacity of Axially Compression High Strength Steel Columns", Journal of Building Structures, 2012, Vol. 33, No. 3, pp. 8-14.
[23] ANSI/AISC 360-10.Specification for Structural Steel Buildings, Chicago : American Institute of Steel, Construction, 2010.
[24] BS EN 1993-1-1 Eurocode 3 : Design of Steel Structures,Part 1-1:General Rules and Rules for Buildings, Brussels: European Committee for Standardization, 2005.
[25] Gao, L., Sun, H.C., Jin, F.N., et al., "Load-carrying Capacity of High-strength Steel Box-sections I: Stub columns", Journal of Constructional Steel Research, 2009, Vol. 65, No. 4, pp. 918-924.
[26] Wang, J.L., ANSYS12.0 Finite Element Analysis and Example, Beijing:China Machine Press, 2010. (in Chinese).
[27] Antonio, F., Matens, Joel A. Witz, "A Parameter Study of the Post-buckling Behaviour of Steel Plate, Engineering Structure, 2001, Vol. 23, pp. 172-185.
[28] Shen, Z.Y. and Zhang, Q.L., "Post-Buckling Ultimate Load-Carrying of Compressed Square-Tube Steel Column", Journal of Civil Engineering, 1991, Vol. 24, No. 3, pp. 15-26.
[29] Deena, K. Dinno，"Strength and Ductility of Steel Members based on Post-yield Stability and Collapse Behaviour"，Doctor of Philosophy，Canada：Department of Civil Engineering University of Toronto, 2002.

EFFECTIVE LENGTH FACTOR OF COLUMNS IN NON-SWAY MODULAR STEEL BUILDINGS

Guo-Qiang Li[1,2], Ke Cao[1], Ye Lu[1,2,*] and Jian Jiang[1]

[1]*College of Civil Engineering, Tongji University, Shanghai 200092, PR China*
[2]*State Key Laboratory for Disaster Reduction in Civil Engineering, Tongji University, Shanghai 200092, PR China*

**(Corresponding author: E-mail: luyet@tongji.edu.cn)*

Received: 8 February 2016; Revised: 27 January 2017; Accepted: 25 February 2017

ABSTRACT: Prefabrication by off-site manufacturing (OSM) leads to faster construction, improved quality, and reduced resources and waste. As a specific type of off-site structure, modular steel buildings consisting of volumetric modular units is a relatively new structural form in comparison with traditional steel frames with fixed or flexible beam-to-column connections. For multi-strorey modular steel buildings, additional lateral force-resisting systems are commonly used to prevent the structural side sway. In order to rationally evaluate the stability of columns in the non-sway modular steel buildings, the governing equations for determining the effective length factor (*K*-factor) of columns are derived using the three-column sub-assemblage model. A simplified method based on the French rule is proposed to determine *K*-factors. Its accuracy and effectiveness are verified against governing equations (maximum error within 6%) and finite element simulation of a six-storey modular steel frame (maximum error within 9%). The influencing factors on the *K*-factor are studied. The results show that the available methods such as the alignment chart and French rule cannot be directly applied to determine *K*-factors for the modular steel buildings. It is found that the boundary restraint parameters and their relative values affect the *K*-factor. The assumption of pinned connections between modular units is found to be non-conservative. It is recommended to check and strengthen the flexible connections for the design of modular steel buildings with too small or too large relative stiffness of the connections between modules.

Keywords: Effective length factor, column buckling, semi-rigid connection, non-sway modular steel building, simplified method

DOI: 10.18057/IJASC.2017.13.4.6

1. INTRODUCTION

Modules, as prefabricated room-sized volumetric units are normally fully fitted at the manufacturing stage and are installed on site as load-bearing ‘building blocks’ [1]. Although the modular concept is similar to temporary and mobile buildings, it differs in terms of structural design and quality requirements. A multi-storey modular steel building consisting of volumetric modular units (hereinafter, modular steel building) is a collection of modular units joined together to form a self-supported and load-bearing structure. It has to conform to building codes for its intended use [2]. There are two generic forms of modular units as shown in Figure1, respectively. One is continuously supported modules where vertical loads are transferred through walls (Figure1a). The other is corner-supported modules where vertical loads are transferred through columns (Figure1b) [3]. This study focuses on corner-supported modules.

In most current building codes for steel members and frames, the design of columns is based on the evaluation of elastic restraints at both ends of columns, from which the effective length factor (hereinafter, the *K*-factor) is derived for estimating the buckling load. The alignment chart method was used in codes of the United States [4] and Canada [5] to obtain *K*-factors. It is the graphic solution of mathematically exact equations. The accuracy of alignment charts essentially depends on the chart size of and users' sharpness of vision. In Europe [6] and China [7], the *K*-factor can be determined by simplified equations called “French rules” [8]. These equations are accurate, yet

simple enough to be used. However, both of these two methods are proposed based on traditional steel frames with fixed beam-to-column connections.

Many efforts have been taken to determine the *K*-factor for flexibly connected non-sway frames. Three data bases have been made for connection models by Goverdhan[9]; Nethercot[10]; and Kishi-Chen[11]. For non-sway frames with flexible connections, Chen[12], Lui [13], and Bjorhovde [14] proposed calculation methods of *K*-factors. Lui [13] proposed a simple procedure in which the initial and zero connection stiffness were taken for unloading and loading conditions, respectively. It was the simplest method but failed to consider the non-linearity of beam-to-column connections for both braced and unbraced frames [12]. Barakat and Chen[12] recommended the modification of the relative stiffness factor in the alignment chart method using the secant connection stiffness. For non-sway frames, it led to a constant *K*-factor at all loading levels which was similar to Lui's method.

For modular steel buildings, the modular units are produced in a factory with welded beam-to-column connections, and are then assembled on site using bolt connections. Thus, the connection can be considered as semi-rigid consisting of rigid individual modular unit.. For multi-strorey or high-rise modular steel buildings, additional lateral force-resisting systems such as braces[15] or steel panels[16] are commonly used to effectively prevent their lateral sway. The models for traditional braced frames with flexible connections and non-sway modular steel building frames with bracings, are shown in Figure 2. This study focuses on the latter.

The structural behavior of modular steel buildings is totally different from that of traditional rigid or flexible frames. This indicates that the methods mentioned above are not applicable for modular steel buildings. As a new structural system, few research has been done on modular steel buildings. Annan[15,17,18] and Hong[16] studied the behavior of low-rise modular steel buildings under a series of ground motions. The concentrical bracing and double skinned steel plate were used to prevent lateral drift. It was found that the energy dissipation capacity of modular steel buildings was slightly better than that of regular frames. The former had various internal force distribution and force-transfer mechanisms compared with traditional frames. Lawson and Richards[1,3,19] carried out case studies on mid to relatively high-rise modular steel buildings in UK without considering the dynamic response under seismic loads. They presented some engineering projects in detail and experimentally investigated the robustness of a pair of modular units under unusual actions.

However, there is rare research and building codes on the effective length factors (*K*-factors) of columns in modular steel buildings. In engineering practices, the flexible connection between modular units is always considered as pinned, and thus the French rules is used to determined *K*-factors[20]. This method is proven to be non-conservative as illustrated in this paper. Therefore, it is necessary to propose a new method to determine the *K*-factor of columns for modular steel buildings.

In this paper, the governing equations for determining the *K*-factor for non-sway modular steel buildings with bracings are derived. A simplified method, similar to the French rules, is proposed based on these governing equations and verified against analytical and numerical results. Finally, the influencing factors on *K*-factors are studied.

a. Continuously supported module (by Terrapin)

b. Corner-supported module (by Kingspan)

Figure 1. Typical Cases of Continuously supported Module and Corner-supported Module

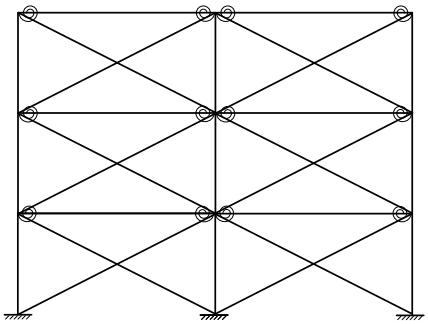

a. Braced Frame with Flexible Connections

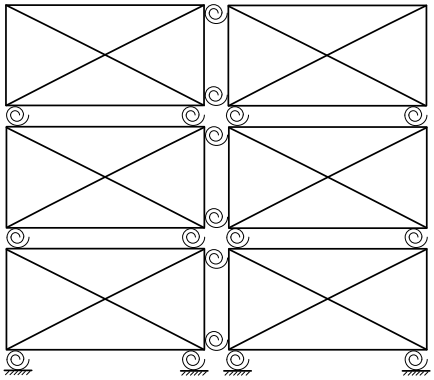

b. Non-sway Modular Steel Building Frame with Bracings

Figure 2. Models of Traditional and Modular Frames

2. MODELING ASSUMPTIONS

Figure 3 shows the sub-assemblage model used for determining the *K*-factor of columns in a non-sway modular steel building. The model is composed of the column c_2 (member CD in Figure 3), five restraining columns (c_1, c_3, c_4, c_5, and c_6), and eight restraining beams (b_1, b_2, b_3, b_4, b_5, b_6, b_7, and b_8). The semi-rigid connections between modular units are represented by a series of rotational springs.

For simplification, the following eight assumptions are adopted:

1. All members of the modular units behave elastically;
2. Axial forces in the beams are negligible;
3. All columns within a given storey buckle simultaneously;
4. Stability functions for all columns in the sub-assemblage model are identical;
5. At buckling of the sub-assemblage, the rotations at two ends of a beam are assumed to be of equal magnitude but opposite direction (i.e. beams are bent in a single curvature);
6. The beam-to-column connections within the modular unit are assumed to be rigid;
7. The connections between modular units are assumed to be semi-rigid;
8. At buckling of the sub-assemblage, the end rotations of columns in adjacent storey are proportional.

According to the assumptions 3 and 4, the deformations of columns c_2 and c_5 at buckling of the sub-assemblage are identical, and thus the sub-assemblage model shown in Figure 3 is bilaterally symmetrical which can be simplified. The simplified sub-assemblage model is shown in Figure 4, being composed of the column c_2 (member CD in Figure 4), two restraining columns (c_1 and c_3), and four restraining beams (b_1, b_2, b_3, and b_4).

In Chen's model of flexibly jointed and non-sway frames [12], the effect of non-linear connection stiffness was taken into account since the rotation between beams and columns was not negligible under a vertical load. For non-sway modular steel buildings, connections between beams and columns are assumed to be rigid, and the rotation between modular units in adjacent storey is negligible as the designed vertical load of each storey is identical. Therefore, the initial rotational stiffness of the semi-rigid connections can be used for modular steel buildings in unloading and loading conditions.

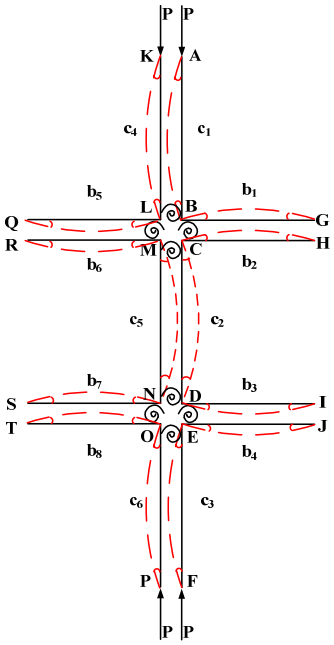

Figure 3. Sub-assemblage Model without Lateral Sway

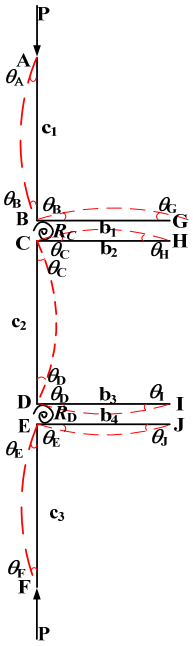

Figure 4. Simplified Sub-assemblage Model without Lateral Sway

3. SLOPE DEFLECTION EQUATIONS OF MEMBERS

Since the beam-to-column connections in a single modular unit are assumed rigid, the slope deflection equations of beam and column members in a non-sway modular unit are identical to those of traditional non-sway frames.

The beam element AB with end moments M_{AB} and M_{BA} is shown in Figure 5. For the sub-assemblage model with the assumed deflected shape $\theta_A = -\theta_B$, as shown in Figure 5, the slope-deflection equations are generally expressed in terms of θ_A as:

$$M_{AB} = 2\frac{EI_b}{L_b}\theta_A \tag{1}$$

where L_b is beam length; EI_b is flexural rigidity of beam; θ_A and θ_B are corresponding nodal rotations.

Figure 6 shows the model of the column element CD subjected to an axial force P and end moments M_{CD} and M_{DC}. The slope-deflection equations of the column CD are represented by stability functions as [12]:

$$M_{CD} = \frac{EI_c}{L_c}[s_{ii}\theta_C + s_{ij}\theta_D] \tag{2}$$

$$M_{DC} = \frac{EI_c}{L_c}[s_{ji}\theta_C + s_{jj}\theta_D] \tag{3}$$

where L_c and EI_c are the length and flexural rigidity of the column, respectively; s_{kl} (k, l =i or j) are the stability functions defined as:

$$s_{ii} = s_{jj} = \frac{kL_c \sin kL_c - (kL_c)^2 \cos kL_c}{2 - 2\cos kL_c - kL_c \sin kL_c} \tag{4}$$

$$s_{ij} = s_{ji} = \frac{(kL_c)^2 - kL_c \sin kL_c}{2 - 2\cos kL_c - kL_c \sin kL_c} \tag{5}$$

where

$$k = \sqrt{\frac{P}{EI}} \tag{6}$$

The K-factor of a column can therefore be obtained by Equation (6) as:

$$K = \frac{\pi}{kL_c} \tag{7}$$

Substituting Eq. (7) into Eqs. (4) and (5), the stability functions s_{kl} (k, l =i or j) can be expressed by K as:

$$s_{ii} = s_{jj} = \frac{\frac{\pi}{K}\sin\frac{\pi}{K} - (\frac{\pi}{K})^2 \cos\frac{\pi}{K}}{2 - 2\cos\frac{\pi}{K} - \frac{\pi}{K}\sin\frac{\pi}{K}} \tag{8}$$

$$s_{ij} = s_{ji} = \frac{(\frac{\pi}{K})^2 - \frac{\pi}{K}\sin\frac{\pi}{K}}{2 - 2\cos\frac{\pi}{K} - \frac{\pi}{K}\sin\frac{\pi}{K}} \tag{9}$$

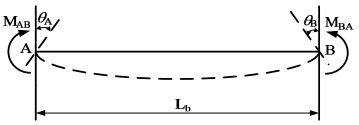

Figure 5. Model of Non-sway Beam Element subjected to End Moments

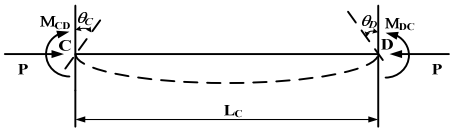

Figure 6. Model of Non-sway Column Element subjected to End Moments

4. Governing Equations for *K*-factor

According to the assumption 4, the rotations of beams in the simplified sub-assemblage (Figure 4) can be simplified as: $\theta_C = -\theta_H$, $\theta_D = -\theta_I$, $\theta_B = -\theta_G$ and $\theta_E = -\theta_D$. The nodal rotations of joint B and E can be expressed as:

$$\theta_B = \theta_C - \frac{M_C}{R_C} \tag{10}$$

$$\theta_E = \theta_D - \frac{M_D}{R_D} \tag{11}$$

where R_C and R_D are the stiffness of the semi-rigid connections, respectively; M_C and M_D are the moments of the semi-rigid connections, respectively.

According to the assumption 8, the nodal rotations of joint A and F can be expressed as:

$$\theta_A = (\theta_C - \frac{M_C}{R_C}) \times \frac{\theta_D}{\theta_C} \tag{12}$$

$$\theta_F = (\theta_D - \frac{M_D}{R_D}) \times \frac{\theta_C}{\theta_D} \tag{13}$$

The end moments of beam and column elements shown in Figure4 can thus be expressed as:

$$M_{BG} = 2i_{b1}(\theta_C - \frac{M_B}{R_C}) \tag{14}$$

$$M_{CH} = 2i_{b2}\theta_C \tag{15}$$

$$M_{DI} = 2i_{b3}\theta_D \tag{16}$$

$$M_{EJ} = 2i_{b4}(\theta_D - \frac{M_E}{R_D}) \tag{17}$$

$$M_{BA} = i_{c1}[s_{ii}(\theta_C - \frac{M_B}{R_C}) + s_{ij}(\theta_D - \frac{M_B}{R_C}\frac{\theta_D}{\theta_C})] \tag{18}$$

$$M_{CD} = i_{c2}(s_{ii}\theta_C + s_{ij}\theta_D) \tag{19}$$

$$M_{DC} = i_{c2}(s_{ii}\theta_D + s_{ij}\theta_C) \tag{20}$$

$$M_{EF} = i_{c3}[s_{ii}(\theta_D - \frac{M_E}{R_D}) + s_{ij}(\theta_C - \frac{M_E}{R_D}\frac{\theta_C}{\theta_D})] \tag{21}$$

where M_{BG} is the end moment of beam BG at joint B; M_{CH} is the end moment of beam CH at joint C; M_{DI} is the end moment of beam DI at joint D; M_{EJ} is the end moment of beam EJ at joint E; M_{BA} is the end moment of column BA at joint B; M_{CD} and M_{DC} are the end moments of column CD at joints C and D, respectively; M_{EF} is the end moment of column EF at joint E; i_{bm} (m =1, 2, 3, or 4) are the linear stiffness of the beams, and i_{cn} (n =1, 2 or 3) are the linear stiffness of the columns:

$$i_{bm} = \frac{EI_{bm}}{L_b} \tag{22}$$

$$i_{cm} = \frac{EI_{cm}}{L_c} \tag{23}$$

The moment equilibriums at points *B*, *C*, *D*, and *E* can be expressed as:

$$-M_C + M_{BA} + M_{BG} = 0 \tag{24}$$

$$M_C + M_{CH} + M_{CD} = 0 \tag{25}$$

$$-M_D + M_{EF} + M_{EJ} = 0 \tag{26}$$

$$M_D + M_{DI} + M_{DC} = 0 \tag{27}$$

By solving Equations (14) ~ (27), the equations for θ_C, θ_D, and *K* can be obtained as:

$$\begin{aligned}&(s_{ii}R_Ci_{c1} + 2R_Ci_{b1} + 2R_Ci_{b2} + 2s_{ii}i_{c1}i_{b2} + 4i_{b1}i_{b2} + s_{ii}R_Ci_{c2} + s_{ii}^2i_{c1}i_{c2} + 2s_{ii}i_{b1}i_{c2})\theta_C^2 \\ &+(s_{ij}R_Ci_{c1} + 2s_{ij}i_{b2}i_{c1} + 2s_{ii}s_{ij}i_{c1}i_{c2} + s_{ij}R_Ci_{c2} + 2s_{ij}i_{b1}i_{c2})\theta_C\theta_D + s_{ij}^2i_{c1}i_{c2}\theta_D^2 = 0\end{aligned} \tag{28}$$

$$\begin{aligned}&(s_{ii}R_Di_{c3} + 2R_Di_{b4} + 2R_Di_{b3} + 2s_{ii}i_{b3}i_{c3} + 4i_{b3}i_{b4} + s_{ii}R_Di_{c2} + s_{ii}^2i_{c2}i_{c3} + 2s_{ii}i_{b4}i_{c2})\theta_D^2 \\ &+(s_{ij}R_Di_{c3} + 2s_{ij}i_{c3}i_{b3} + 2s_{ii}s_{ij}i_{c2}i_{c3} + s_{ij}R_Di_{c2} + 2s_{ij}i_{b4}i_{c2})\theta_C\theta_D + s_{ij}^2i_{c2}i_{c3}\theta_C^2 = 0\end{aligned} \tag{29}$$

The relative beam-to-column stiffness factor G and relative unit connection to column stiffness factor J can be defined as:

$$G_B = \frac{i_{b1}}{i_{c1}} \qquad G_C = \frac{i_{b2}}{i_{c2}} \qquad G_D = \frac{i_{b3}}{i_{c2}} \qquad G_E = \frac{i_{b4}}{i_{c3}} \tag{30}$$

$$J_B = \frac{R_C}{i_{c1}} \qquad J_C = \frac{R_C}{i_{c2}} \qquad J_D = \frac{R_D}{i_{c2}} \qquad J_E = \frac{R_D}{i_{c3}} \tag{31}$$

By using Eqs. (30) and (31), Eqs. (28) and (29) can be simplified as:

$$\begin{aligned}&(s_{ii}J_C + 2J_CG_B + 2J_CG_C + 2s_{ii}G_C + 4G_BG_C + s_{ii}J_B + s_{ii}^2 + 2s_{ii}G_B)\theta_C^2 \\ &+(s_{ij}J_C + 2s_{ij}G_C + 2s_{ii}s_{ij} + s_{ij}J_B + 2s_{ij}G_B)\theta_C\theta_D + s_{ij}^2\theta_D^2 = 0\end{aligned} \tag{32}$$

$$\begin{aligned}&(s_{ii}J_D + 2J_DG_E + 2J_EG_D + 2s_{ii}G_D + 4G_DG_E + s_{ii}J_E + s_{ii}^2 + 2s_{ii}G_E)\theta_D^2 \\ &+(s_{ij}J_D + 2s_{ij}G_D + 2s_{ii}s_{ij} + s_{ij}J_E + 2s_{ij}G_E)\theta_C\theta_D + s_{ij}^2\theta_C^2 = 0\end{aligned} \tag{33}$$

The Eqs. 32 and 33 are in a binary quadric form about θ_C and θ_D, which can be also expressed as:

$$(\theta_C + \alpha_1\theta_D)(\alpha_2\theta_C + \alpha_3\theta_D) = 0 \tag{34}$$

$$(\alpha_4\theta_C + \theta_D)(\alpha_5\theta_C + \alpha_6\theta_D) = 0 \tag{35}$$

where the coefficients α_1, α_2, α_3, α_4, α_5, and α_6 can be determined by:

$$\alpha_2 = s_{ii}J_C + 2J_CG_B + 2J_BG_C + 2s_{ii}G_C + 4G_BG_C + s_{ii}J_B + s_{ii}^2 + 2s_{ii}G_B \tag{36}$$

$$\alpha_1\alpha_3 = s_{ij}^2 \tag{37}$$

$$\alpha_1\alpha_2 + \alpha_3 = s_{ij}J_C + 2s_{ij}G_C + 2s_{ii}s_{ij} + s_{ij}J_B + 2s_{ij}G_B \quad (38)$$

$$\alpha_6 = s_{ii}J_D + 2J_DG_E + 2J_EG_D + 2s_{ii}G_D + 4G_DG_E + s_{ii}J_E + s_{ii}^2 + 2s_{ii}G_E \quad (39)$$

$$\alpha_4\alpha_5 = s_{ij}^2 \quad (40)$$

$$\alpha_4\alpha_6 + \alpha_5 = s_{ij}J_D + 2s_{ij}G_D + 2s_{ii}s_{ij} + s_{ij}J_E + 2s_{ij}G_E \quad (41)$$

The general governing equations for the *K*-factor of column c_2 can therefore be derived from Eqs. 34 and 35 as:

$$\det\begin{vmatrix}\alpha_2 & \alpha_3\\ \alpha_5 & \alpha_6\end{vmatrix} = 0 \quad (42)$$

By solving (36) ~ (42), the solution of *K*-factor of column c_2 is derived as:

$$\begin{aligned}&(s_{ii}^2 + 2(J_CG_B + (J_B + 2G_B)G_C) + s_{ii}(J_B + J_C + 2(G_B + G_C)))(s_{ii}^2 + 2(J_EG_D\\ &+(J_D + 2G_D)G_E) + s_{ii}(J_D + J_E + 2(G_D + G_E))) - \frac{1}{4}s_{ij}^2(2s_{ii} + J_B + J_C +\\ &2(G_B + G_C) + \sqrt{J_B^2 + 2J_B(J_C + 2G_B - 2G_C) + (J_C - 2G_B + 2G_C)^2})(2s_{ii} +\\ &J_D + J_E + 2(G_D + G_E) + \sqrt{J_D^2 + 2J_D(J_E + 2G_D - 2G_E) + (J_E - 2G_D + 2G_E)^2}) = 0\end{aligned} \quad (43)$$

5. SIMPLIFIED SOLUTION FOR *K*-FACTOR

The Eq. 43 can be solved by numerical methods to obtain the *K*-factor. However the numerical solution is too complicated to be used in practice. Therefore, a simple fitting formula for *K*-factor based on the numerical solutions of Eq. 43 was obtained in this section.

For non-sway steel frames, the French design rules for steel structures [21], also called "French rules", have been widely used in Europe and China since 1966 with the following approximate solution:

$$K = \frac{0.64G_A'G_B' + 1.4(G_A' + G_B') + 3}{1.28G_A'G_B' + 2(G_A' + G_B') + 3} \quad (44)$$

where the restraint factors G_i' ($i = A, B$) is the relative stiffness of all the columns connected at the joint *i* of a steel frame to that of all the beams connected at joint *i*, i.e.,

$$G_i' = \frac{\sum(I_c / L_c)}{\sum(I_b / L_b)} \quad (45)$$

Qualitative analyses showed that when the rotation stiffness R_C and R_D of the connections between the modular units are large enough, a non-sway modular steel building can be treated as a traditional non-sway frame, and thus the simple formula of the French rule is applicable. This means the format of Eq. (44) can be used for modular steel buildings. Therefore, the simple formula for *K*-factor of modular steel buildings can be assumed as:

$$K = \frac{0.64G_C''G_D'' + 1.4(G_C'' + G_D'') + 3}{1.28G_C''G_D'' + 2(G_C'' + G_D'') + 3} \quad (46)$$

where

$$G_C'' = \frac{J_C G_B + (J_B + \alpha) G_C}{J_C + J_B + \alpha} \quad (47)$$

$$G_D'' = \frac{J_D G_E + (J_E + \alpha) G_D}{J_D + J_E + \alpha} \quad (48)$$

where G_C'' and G_D'' are the modified relative stiffness factors of column CD at node C and D, and α is a constant to be determined. When R_C and R_D are large enough, Eqs. (46) ~ (48) can be reduced to Eqs. 44 and 45.

To determine α, the *K*-factors corresponding to various restraint factors, G_B, G_C, G_D, G_E, J_B, J_C, J_D, J_E, obtained from numerical solutions of Eq. (43) were employed. Using the least-squared method to fit the simple formula, the value of α was determined as 0.2. To evaluate the effectiveness of the simple formula Eq. (46), *K*-factors were obtained from Eq. (43) and Eq. (46) for practical values of restraint factors (G_B, G_C, G_D, G_E, J_B, J_C, J_D, J_E,) and the results are listed in Table 1 . The K_e and K_a denote the *K*-factors obtained from Eq. (43) and Eq. (46), respectively. The error between them ($Error_1$) is defined as:

$$Error_1 = \frac{K_a - K_e}{K_e} \times 100\% \quad (49)$$

The positive and negative $Error_1$ indicate the underestimation and overestimation of *K*-factors from the simple formula Eq. (46). From Table 1, it can be seen that, in most cases, the simple formula overestimated the *K*-factors with the maximum error within 6%. The average $Error_1$ was −1.11% and the average absolute $Error_1$ was 1.35%, which showed that the simple formula can reasonably predict the *K*-factor of columns of modular steel buildings.

6. DEMONSTRATION OF A TYPICAL MODULAR STEEL BUILDING

A six-storey modular steel building consisting of 10 modules was used to further demonstrate the effectiveness of the simple formula for *K*-factor of modular steel buildings as shown in Figure 7. The dimension of each module was 3.0 m (height) × 6.0 m (length) × 2.4 m (width). Considering the accuracy and efficiency, the finite element software SAP2000 was used to model the buckling behavior of this modular steel building. The beam and column elements of each module were meshed automatically with a maximum length of 0.1 m. The flexible connections were modeled using linear springs of which three translational degrees of freedoms (DoFs) were constrained. The rotation stiffness of the connections with respect to the *x*- and *y*-axis was set as 4,930 kN•m/rad, which was the initial connection stiffness of the joint obtained by previous experimentation [20]. In order to restrict the buckling in the second to fifth storey, three translational DoFs and two rotational DoFs in the O–*xy* plane of the nodes in the first storey, and both the translational DoFs and rotational DoFs in the O–*xy* plane of the nodes in the sixth storey, were constrained. The two translational DoFs in the O–*xy* plane of the end nodes for other columns were constrained to simulate the non-sway situation. The critical load of first buckling mode, P, was obtained through eigenvalue buckling analyses and the *K*-factor was determined by using Eqs. 6 and 7.

Figure 8 shows the first buckling mode shape of this modular steel building which fits the assumptions well. It can be concluded that the assumptions are reasonable for accurately predicting the buckling behavior of modular steel buildings. The *K*-factors K_n obtained from the numerical simulation in SAP2000 are listed in Table 1. The error between K_n and K_a ($Error_2$) is defined as:

$$\text{Error}_2 = \frac{K_n - K_a}{K_a} \times 100\% \qquad (50)$$

The average Error_2 was −2.66% and the average of the absolute value of Error_1 was 4.82%, which indicates accepted accuracy of the simple formula. Most of the *K*-factors obtained by the numerical model were smaller than those determined by the simple formula. This was because, in the sub-assemblage model, similar deformation curves of columns in adjacent storey were assumed, while in the numerical model the deformation of columns was restrained by boundary conditions. The restraints in the numerical model were stronger than those in the sub-assemblage model.

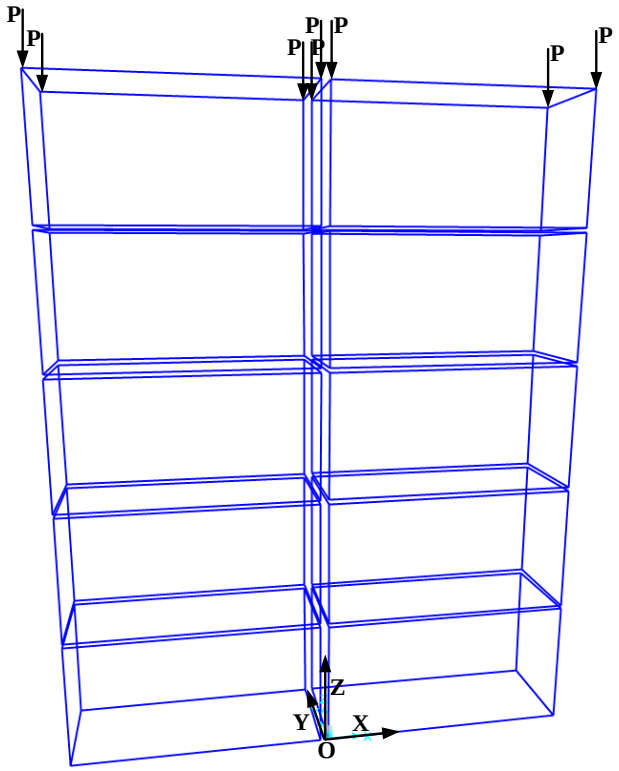

Figure 7. Numerical Model of a Typical Modular Steel Building

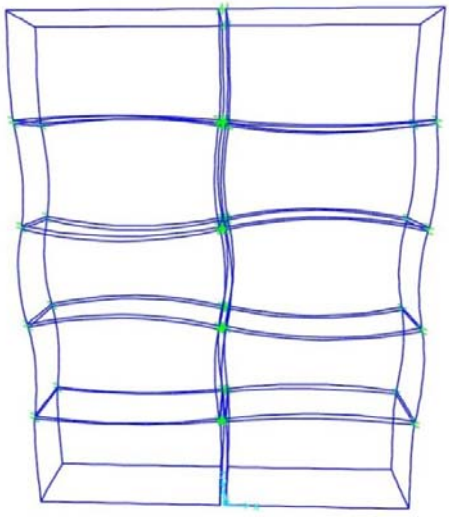

Figure 8. First Buckling Shape of the Modular Steel Building in the Numerical Model

Table 1. Comparison of *K*-factors obtained by Governing Equation, Simple Formula, and Numerical Model

Restraint factors												
G_B	G_C	G_D	G_E	J_B	J_C	J_D	J_E	K_e	K_a	$Error_1$ (%)	K_n	$Error_2$ (%)
0.2	0.6	0.6	0.6	0.75	0.75	0.75	0.75	0.8618	0.8554	−0.74	0.8198	-4.13
0.2	1.5	1.5	1.5	3.00	3.00	3.00	3.00	0.7670	0.7601	−0.90	0.7159	-5.75
0.4	0.6	0.8	0.2	0.50	4.00	5.00	2.00	0.8806	0.8773	−0.37	0.8421	-4.00
0.4	1.5	1.0	2.5	4.00	0.50	0.25	1.00	0.7519	0.7432	−1.15	0.7187	-3.27
0.6	0.4	0.8	1.0	4.00	0.25	0.75	3.00	0.8342	0.8367	0.30	0.7997	-4.44
0.6	1.5	2.5	0.2	0.75	2.00	4.00	0.50	0.8495	0.8198	−3.50	0.8583	4.54
0.8	0.2	0.8	2.5	2.00	3.00	4.00	0.75	0.7636	0.7599	−0.49	0.7192	-5.33
0.8	1.0	2.5	0.8	0.25	0.50	0.75	4.00	0.7392	0.7326	−0.89	0.6932	-5.33
1.0	0.4	1.5	0.2	2.00	5.00	1.00	4.00	0.7816	0.7757	−0.76	0.7339	-5.34
1.0	1.5	0.4	1.0	0.25	1.00	5.00	0.75	0.7768	0.7748	−0.26	0.7348	-5.15
1.5	0.8	2.0	0.2	3.00	0.50	2.00	0.75	0.8294	0.7996	−3.59	0.8317	3.87
1.5	2.0	0.8	1.5	0.25	2.00	0.50	5.00	0.7555	0.7568	0.17	0.7378	-2.52
2.0	0.8	1.5	2.5	0.50	2.00	0.75	0.25	0.7111	0.6988	−1.73	0.6766	-3.11
2.0	2.5	0.4	0.8	3.00	0.25	4.00	2.00	0.7386	0.7428	0.57	0.6812	-8.35
2.5	0.4	2.0	2.5	0.25	0.75	3.00	2.00	0.7364	0.6936	−5.82	0.7357	5.73
2.5	1.5	0.6	0.8	2.00	4.00	0.5	0.25	0.7452	0.7482	0.40	0.7015	-6.26

7. INFLUENCING FACTORS OF *K*-FACTORS

All the restraint factors (G_B, G_C, G_D, G_E, J_B, J_C, J_D, J_E,) may affect the *K*-factors. Furthermore, from qualitative analyses, it was found that the ratios of the relative beam-to-column stiffness G_B/G_C and G_D/G_E also had significant effects on the *K*-factors. Considering the symmetry of the sub-assemblage model, the effects of G_B/G_C and G_D/G_E on the *K*-factor should be the same. To study the effects of G_B/G_C on the *K*-factor of columns, set $J_B = J_C = J_D = J_E$ and $G_B = G_D = G_E = 1$. Using the governing equation, eighty *K*-factors with respect to different values of G_C and J_C were obtained and presented in Figure 9. According to these results, several conclusions can be drawn as follows:

(1) When $G_B/G_C = 1$, the *K*-factor was independent of J_C.
(2) The trend of *K*-factors with respect to J_C changed with G_B/G_C. When $G_B/G_C > 1$, the *K*-factor decreased with the increasing J_C, and tended to converge. This was because the relative beam-to-column stiffness of column c_1 at node C was larger than that of column c_2. Therefore, at buckling, the moment in the flexible joint was opposite to the rotation of column c_2 at node C, which enhanced the restraint of column c_2 and reduced its *K*-factor. The moment increased with the increment of J_C and tended to converge. On the contrary, when $G_B/G_C < 1$, the *K*-factor increased as J_C increased, and attempted to converge.
(3) The *K*-factor may increase with the increasing J_C. This indicates that the assumption of pinned connections between modular units in Mao's research [20] and some engineering practices may overestimate the stability of columns for modular steel buildings, up to 15%. Hence, the method of pinned connections should not be adopted for the design of modular steel buildings.
(4) The influence of J_C on the *K*-factor depended on G_B/G_C. The more the G_B differed from G_C, the greater influence J_C will have on the *K*-factor. It indicates that the moment in the flexible joint to

connect modular units will be significantly influenced by G_B/G_C. The more the G_B differed from G_C, the larger the moment. The rotation of the flexible joint can be obtained by Eqs. (28) and (29). It was found that when G_B/G_C was 0.35 or 2.64, the rotation of the flexible joint could reach 0.5°, which was half of the elastic limit angle [20]. Thus, it is suggested that, in the design of modular steel buildings for G_B/G_C or G_D/G_E beyond the range of 0.38~2.64, the joint must be double-checked and strengthened. The range given above was established on several preliminary conditions and its applicability needs to be further studied.

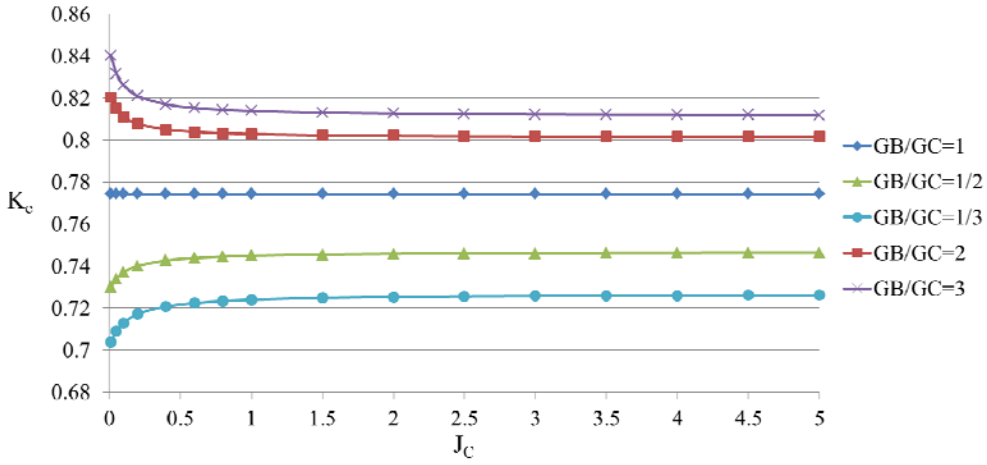

Figure 9. Variation of K_e-J_C Curves against Different G_B/G_C

8. CONCLUSIONS

This paper proposed analytical solutions of *K*-factors of columns in non-sway modular steel buildings with bracings. The accuracy of the proposed method was verified against numerical results. The following conclusions can be drawn:

(1) The governing equations for determining the *K*-factor of columns for non-sway modular steel buildings were derived based on a sub-assemblage model. Several assumptions applicable to non-sway frames with flexible connections were proposed. It was found that it was not suitable to directly apply the available methods such as the alignment chart and French rule to determine *K*-factors for modular steel buildings.
(2) The simple formula for determining the *K*-factor for non-sway modular steel buildings was obtained using least-squared method to fit the proposed governing equations. The accuracy of the proposed simple formula was verified against governing equations given the maximum errors within 6% and the average absolute error of 1.35%.
(3) The effectiveness of the simple formula was also verified against numerical simulation of a six-storey frame with 10 modules. The maximum error between the analytical and numerical results of *K*-factors was within 8.35%. It indicated the good applicability of the proposed simplified method to practical cases.
(4) The variation of *K*-factors with J_C depended on G_B/G_C. The assumption of pinned connections between modular units was found to be non-conservative. Furthermore, it is recommended to check and strengthen the flexible connections in the modular steel buildings with too small or too large G_B/G_C.

NOTATION

EIb	Flexural rigidity of beam
EIc	Flexural rigidity of column
Lb	Length of beam
Lc	Length of column
MAB, MBA	End moment at joints A and B
M_{BG}, M_{CH}, M_{DI}, M_{EJ}	End moment of beam at joints B, C, D, and E
M_{CD}, M_{DC}, M_{EF},	End moment of column at joints C, D, and E
M_C, M_D	Moments of the semi-rigid connections at joints C and D
θ_A, θ_B, θ_C, θ_D, θ_E, θ_F	Nodal rotations at joints A, B, C, D, E, and F
s_{kl}	Stability functions ((θ_A, θ_B, θ_C, θ_D, θ_E, θ_F)
k	$\sqrt{P/EI_c}$
K	Effective length factor of column
P	Axial force subjected to column
R_C, R_D	Connection stiffness of the semi-rigid connections at joints C and D
i_{bm}	Linear stiffness of the beams (m =1, 2, 3, or 4)
i_{cn}	linear stiffness of the columns (n =1, 2, or 3)
G_B, G_C, G_D, G_E	Relative beam-to-column stiffness factors at joints B, C, D, and E
J_B, J_C, J_D, J_E	Relative joint to column stiffness factors at joints B, C, D, and E
G_A', G_B'	Relative stiffness of all the columns connected at joints A and B to that of all the beams (i = A, B)
G_C'', G_D''	Modified relative stiffness factors of column CD at joints C and D

REFERENCES:

[1] Lawson, R.M., Richards, J., "Modular Design for High-rise Buildings", Proceedings of the ICE - Structures and Buildings, 2010, Vol. 163, pp. 151-64.

[2] Fathieh, A., "Nonlinear Dynamic Analysis of Modular Steel Buildings in Two and Three Dimensions", [Master of Applied Science], Toronto: University of Toronto, 2013.

[3] Lawson, R.M., Ogden, R.G., "Hybrid' Light Steel Panel and Modular Systems", Thin-Walled Structures, 2008, Vol. 46, pp. 720-30.

[4] Construction AIOS.AISC 325-05 Steel Construction Manual, Thirteenth Edition, 2006.

[5] National Standard of Canada CAN/CSA-S16, 1-M89, Limit States Design of Steel Structures, 1989.

[6] European Convention for Constructional Steel Work ERFS, 1978.

[7] JGJ 99-98, Chinese Technical Specification for Steel Strucure of Tall Buildings.

[8] Dumonteil, P., "Simple Equations for Effective Length Factors", Engineering Journal, American Institute of Steel Construction, 1992, Third quarter: 111-5.

[9] AV, G., "A Collection of Experimental Moment–rotation Curves and Evaluation of Prediction Equations for Semi-rigid Connections", [Master], Nashville: Vanderbilt University, 1983.

[10] DA, N., "Steel Beam-to-column Connections: a Review of Test Data and Its Applicability to the Evaluation of Joint Behavior in Performance of Steel Frames", CIRIA Project Record 1985.

[11] Kishi, N.C.W., "Data Base of Steel Beam-to-column Connections", Structural Engineering Report. Structural Engineering Report, West Lafayette: Purdue University, 1986.

[12] Kishi, N., Chen, W.F., Goto, Y. and Komuro, M., "Effective Length Factor of Columns in Flexibly Jointed and Braced Frames", Journal of Constructional Steel Research, 1998, Vol. 47, pp. 93-118.

[13] EM, L., "Effects of Connection Flexibility and Panel Zone Deformation on the Behavior of Plane Steel Frames", Ph.D., West Lafayette, Purdue University, 1985.
[14] RB. "Effect of End Restraint on Column Strength: Practical Applications", Engineering Journal, AISC, 1984, Vol. 1, pp. 1-13.
[15] Annan, C.D., Youssef, M.A. and Naggar, M.H.E., "Seismic Overstrength in Braced Frames of Modular Steel Buildings", Journal of Earthquake Engineering, 2009.
[16] Hong, S., Cho, B., Chung, K. and Moon, J., "Behavior of Framed Modular Building System with Double Skin Steel Panels", Journal of Constructional Steel Research, 2011, Vol. 67, pp. 936-46.
[17] Annan, C.D., Youssef, M.A. and Naggar, M.H.E, "Experimental Evaluation of the Seismic Performance of Modular Steel-braced Frames", Engineering Structures, 2009.
[18] Annan, C.D., Youssef, M.A. and Naggar, M.H.E., Seismic Vulnerability Assessment of Modular Steel Buildings", Journal of Earthquake Engineering, 2009.
[19] Lawson, P.M., Grubb, P.J., Byfield, M.P. and Popo-Ola, S.O., "Robustness of Light Steel Frames and Modular Construction", Proceedings of the ICE - Structures and Buildings, 2008, Vol. 161, pp. 3-16.
[20] Lei, M., "Research on Joint Mechanical Behavior of Container Architecture [Master]. Shang Hai: Tongji University, 2015.
[21] Eyrolles, P., Regles de calcul des Constructions en acier CM66.1975.

THE HONG KONG POLYTECHNIC UNIVERSITY
香港理工大學

DEPARTMENT OF CIVIL AND ENVIRONMENTAL ENGINEERING
土木及環境工程學系

First Announcement and Call for Papers

ICASS '18

9th International Conference on

Advances in Steel Structures

Hong Kong, 5-7 December 2018

Conference web: www.ascjournal.com/icass2018

Organised by

Department of Civil and Environmental Engineering
The Hong Kong Polytechnic University

Sponsored by (to be confirmed)

HKIE THE HONG KONG INSTITUTION OF ENGINEERS 香港工程師學會
Civil, Structural and Fire Divisions

香港鋼結構學會 Hong Kong Institute of Steel Construction

RCATISE
Research Centre for Advanced Technology in Structural Engineering
The Hong Kong Polytechnic University

Scope and Objectives

This will be the ninth in the international conference series on Advances in Steel Structures, with the first, second, third and sixth of the conferences series held in Hong Kong, fourth in Shanghai, fifth in Singapore, seventh in Nanjing and eighth in Portugal. As with the eight previous successful conferences, this conference is intended to provide a forum for researchers and professionals to discuss and disseminate recent advances in analysis, behaviour, design and construction of steel, aluminium and composite steel-concrete structures.

Papers related to all aspects of analysis, behaviour, design, fabrication and construction of steel and composite steel-concrete structures are invited. The following topics are not exhaustive and papers that fall within the general theme of the conference will be considered for presentations and for publications in the conference proceedings and uploaded to web www.hkisc.org./icass2018. Selected papers will also be published in the International Journal of Advances in Steel Construction which carries a mission of technology transfer and is widely circulated among the engineering and building professionals.

Steel Structures, Composite Construction, Mixed Construction, Aluminium and Glass Structures, Cold-Formed Steel, Columns, Beams, Beam-Columns, Frames, Connections, Space Structures, Tall Buildings, Bridges, Cable Structures, Pre-tensioned Structural Systems, Curtain Walling, Scaffolding, Roof Cladding, Silos, Tanks, Pipelines, Offshore Platforms, Chimneys, Transmission Line Towers and Masts, Design Codes, Expert Systems, Structural Stability, Stability Design, Computational Methods, Advanced Analysis, Second-order Direct and Indirect Analysis, Non-linear Analysis, Performance-based Structural Design, Dynamics, Seismic-resistant Structures, Vibration Control, System Identification, Fatigue and Fracture, Corrosion, Fire Engineering, Structural Optimisation, Life-cycle Performance, Code and Standard Development.

Official Language

English will be the official language of the Conference for both oral and written presentations.

Key Dates

Submission of Abstracts: 1 March 2018
Provisional Acceptance: 1 May 2018
Submission of Final Papers: 1 July 2018
Final Notice of Acceptance: 31 August 2018
Conference: 5-7 December 2018

Proceedings

The proceedings of the conference will be published by the Hong Kong Institute of Steel Construction.

Registration Fee

The conference registration fee is US$750 (Early bird registration before 1st September 2018)/US$850, which covers conference proceedings, conference banquet, lunches and refreshments.

Call for Papers

Authors are invited to submit 200-300 words abstracts of papers to ICASS'18. All enquiries relating to the conference should be addressed to:

Ms Carol Deng
Conference Secretary
The Hong Kong Institute of Steel Construction

Email: carol.deng@hkisc.org
Conference web: www.ascjournal.com/icass2018

Conference chairman Siu-Lai Chan **Co-chairmen** Tak-Ming Chan and Songye Zhu

ORDER FORM

ISSN 1816-112X

Advanced Steel Construction, an international journal

Indexed by the Science Citation Index Expanded, Materials Science Citation Index and ISI Alerting Services

From: _____

To: ***Secretariat, Advanced Steel Construction, an international journal***
Fax: (852) 2334-6389

I/ We would like to enter a subscription to the ***International Journal of Advanced Steel Construction (IJASC)*** *published by The Hong Kong Institute of Steel Construction.*

Please complete the form and send to:

International Journal of Advanced Steel Construction
c/o Department of Civil and Environmental Engineering
The Hong Kong Polytechnic University
Hunghom, Kowloon, Hong Kong

Fax: (852) 2334-6389 Email: ceslchan@polyu.edu.hk

Published by : The Hong Kong Institute of Steel Construction
Website: http://www.hkisc.org/

Please tick the appropriate box

- ❑ Please enter my hard-copy subscription **(4 issues per year)**.
- ❑ Please send me a complimentary copy of the *Advanced Steel Construction, an International Journal (IJASC).*

Please tick the appropriate box(es)

	Print	**On-line is free**
Personal	❑ US$ 125	
Institutional	❑ US$ 280	

Total Amount **US$** _____

Methods of payment *(please tick the appropriate box(es))*

- ❑ Please invoice me
- ❑ Cheque enclosed for US$ _____ payable to Hong Kong Institute of Steel Construction Limited (No personal cheque accepted)

Ship to

Name (Prof./ Dr./ Mr./ Ms.) _____
Address _____
_____
_____
City/ State/ Postal Code _____
Country _____
Email _____ Fax _____